

# Commissioning and early physics analysis with the ATLAS and CMS experiments

A. Hoecker

CERN, Geneva, Switzerland

## Abstract

These lecture notes for graduate students and young postdocs introduce the commissioning and early physics programme of the high-transverse-momentum experiments ATLAS and CMS, operating at the Large Hadron Collider (LHC) at CERN.

***Preface** — This writeup of lectures given in March 2009 at the 5<sup>th</sup> Latin American School of High-Energy Physics, Recinto Quirama, Colombia, provides an overview of the various commissioning phases pursued by the ATLAS and CMS experiments to thoroughly prepare the detectors and data acquisition systems for physics. As an ATLAS member, the access to the relevant information from my own experiment was so invitingly easy that the document features an intolerable emphasis on ATLAS. I can only sincerely apologize to my CMS colleagues, and state that changing all figures shown into the corresponding ones from CMS would not alter the message the lectures seek to convey. In spite of their very different design, ATLAS and CMS have similar physics potential. Wherever significant performance differences exist, they are pointed out throughout these notes. Most of the analyses discussed here are taken from the vast ATLAS and CMS detector, performance, and physics reports [1–4]. No explicit reference is given when using results from these papers. While finalising these notes, the LHC restarted the commissioning programme in November 2009, after a year of repair and consolidation, achieving for the first time proton–proton collisions at 900 GeV centre-of-mass injection energy, and — for short periods — even the new world record energy of 2.36 TeV. Results from the analyses of collision data, which were not available at the time of the lectures, are not included in these notes.*

## 1 Motivation for a huge machine

The Large Hadron Collider (LHC) at the European Laboratory for Particle Physics Research (CERN) is the most powerful proton accelerator ever built. It collides two beams of protons accelerated to 7 TeV each and bent by dipole magnets with 8.3 T magnetic field strength within the 26.7 km circular collider, immersed in a ca. 100 m deep tunnel between Lake Geneva and the French Jura mountains. If the proton were an elementary particle, that is, if it were point-like, the 14 TeV centre-of-mass energy released by the collision could be fully transformed into mass. Dependent on quantum numbers and conservation laws (symmetries), for example one heavy particle of 14 TeV or a particle–antiparticle pair of 7 TeV each (masses of particles and antiparticles are identical) could be produced. Since the heaviest known particle is the top quark with mass of 173 GeV, any heavier particle found would be a discovery. These new heavy particles might decay to other new particles, still heavier than the top quark, and henceforth a full cascade of new particles could be discovered. The proton is, however, not an elementary particle, but is made out of a cloud of quarks and gluons (partons). The collision of two protons can thus be regarded as collisions between partons with momentum fractions that follow a density distribution with long tails towards one. Unlike for instance at  $e^+e^-$  colliders, increasing the number of recorded collisions increases the probability for the occurrence of very hard parton scattering involving large fractions of the proton–proton centre-of-mass energy. A high-luminosity 14 TeV proton–proton collider therefore allows the experiments to deeply explore the TeV scale.

What does TeV scale signify? Let us recall the relevant atomic, nuclear, and particle physics scales. The only known massless elementary particles are photons and gluons (bosons), which propagate the electromagnetic and strong forces, respectively. The lightest fermions are the neutrinos with masses probably lower than a few eV. This is below the atomic binding energy, which reaches tens of eV.

The next orders of magnitudes are represented by the electron mass (1 MeV), nuclear binding energy (up to 10 MeV), pion and muon masses (100 MeV), the heaviest known lepton as well as proton, neutron, and vector-meson masses (1 GeV), the  $c\bar{c}$  and  $b\bar{b}$  resonances and heavy-quark mesons (10 GeV), and finally the electroweak unification scale, represented by the masses of the Z and W weak-interaction bosons, the top quark, and (presumably) the Higgs boson (100 GeV) and the Higgs vacuum expectation value (246 GeV). No particles beyond that scale are known to date.

However, as we shall see later, the requirement of a stable Higgs sector suggests the existence of new phenomena at the TeV scale, which is precisely the area of sensitivity of the LHC. Little is known beyond that scale. Will new symmetries arise, the breaking of which generates new particles? The seesaw mechanism accommodating massive neutrinos predicts heavy right-handed Majorana neutrinos of mass up to  $10^{14}$  GeV. Unification of the electroweak and strong interactions may occur at  $10^{16}$  GeV. Finally, gravitation becomes strong at the particle level at the Planck scale of order  $10^{18}$  GeV, requiring a quantum field theory that includes gravitation. The minimal Standard Model (assuming massless neutrinos) of unified electroweak and strong interactions includes 19 free parameters, among which are 3 coupling constants, 1 spin-1 and 1 spin-0 boson mass, 9 fermion masses, 3 weak quark mixing angles, 1  $CP$ -violating weak phase, and 1  $CP$ -violating strong phase, which is either tiny or zero. Including a massive neutrino sector increases the number of free parameters by at least 9, depending on the nature of the neutrinos.

The dynamical predictions of the Standard Model have been verified to extreme precision in the past thirty-five years at a large number of very different experiments. Let us recall a few eminent examples. The cross section of lepton pair production has been measured to order 1 TeV and found in agreement with the Z resonance being the highest particle decaying into two leptons, and Drell–Yan production being the dominant process beyond the Z (*cf.* topmost plot in Fig. 1 [5]). Electroweak unification has been tested by globally fitting the Standard Model prediction to precision measurements obtained at the high-energy  $e^+e^-$  colliders LEP (CERN) and SLC (SLAC), and at the  $p\bar{p}$  collider Tevatron (FNAL). The second plot from the top in Fig. 1 shows the relation between measured and predicted W-boson mass versus the top-quark mass [6]. The universality of weak interactions has been verified at the 0.3% level by comparing the tau branching fractions to electron and muon plus neutrinos and to the tau-lepton lifetime (*cf.* bottom left plot in Fig. 1 [7]). The asymptotic freedom property of QCD has been verified at the 1% level by measuring the evolution (‘running’) of the strong coupling at

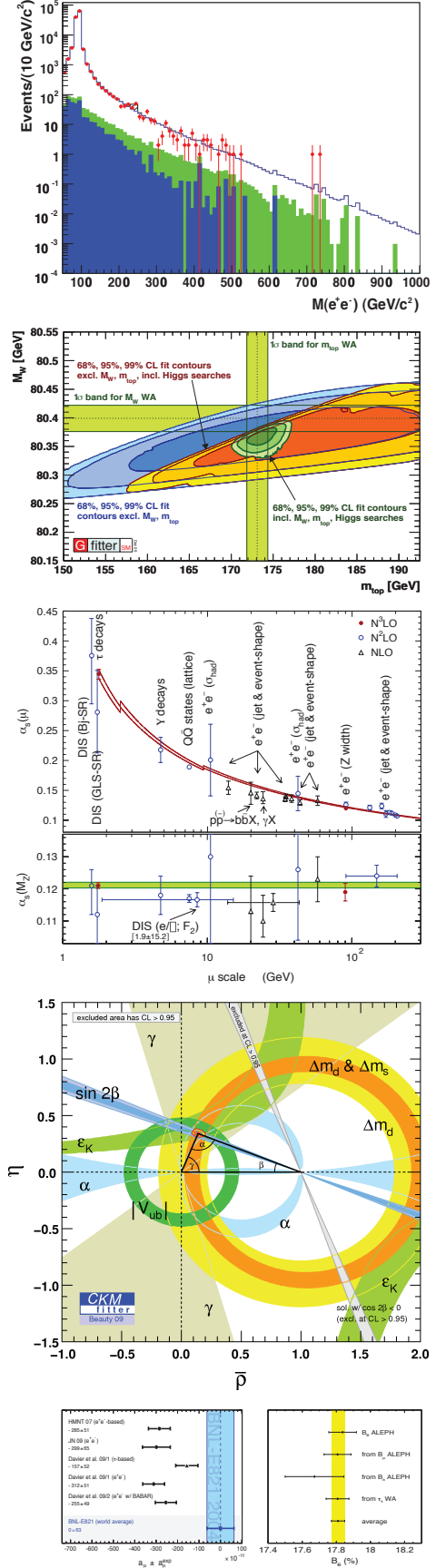


**Fig. 1:** Tests of the Standard Model.

various energy scales, the most precise of which being the ones at the  $\tau$  and the  $Z$  mass scales (third plot in Fig. 1 [8]). The Standard Model predicts that all  $CP$ -violating phenomena involving weak charged currents originate from a single phase in the quark mixing matrix. This has been verified by relating different measurements of  $CP$  violation in the  $B$ -meson and kaon sectors to each other, all showing compatibility (fourth plot in Fig. 1 [9]). The  $CP$ -violating electric dipole moment of the electron has been found to be smaller than  $10^{-27}$  ecm as predicted by the Standard Model. The anomalous magnetic moment of the muon has been measured to the parts-per-million level, verifying the predicted contributions from electromagnetic, weak, and hadronic loop corrections. A small deviation from the expectation is currently not at a sufficiently significant level to draw conclusions (*cf.* bottom right plot in Fig. 1 [10]). Many more examples all confirm the Standard Model. So, what's the problem?

As explained in much detail by John Ellis [11] and others at this school, the Standard Model — though describing so gloriously the experimental data — is, at best, incomplete. Firstly, the Higgs boson, the last elusive Standard Model ingredient, has not yet been discovered. Even if it were discovered, it would be the only elementary scalar particle in the Standard Model, which — for many physicists — is conceptually unsatisfactory. A popular question is the origin of the large mass hierarchy between fermions of different generations, amounting to more than 4 orders of magnitude between top and up quarks. Many astrophysical observations have established the presence of cold dark matter in the galaxies and galactic halos. Moreover, spurious repulsive ‘dark energy’ appears to accelerate the expansion of the universe. In particle physics, we can use the standard quantum field theory renormalisation groups to predict the energy-scale dependence of the electroweak and strong coupling constants. Evolving the three couplings to  $10^{16}$  GeV, they *almost* converge towards a single unified coupling — almost, but not quite. While unification might be considered an aesthetic requirement, stability of the Higgs sector is not. Indeed, the virtual loop corrections, in particular from top-pair vacuum polarisation, diverge quadratically with their high-energy cut-off. Also, perturbativity of the Higgs quartic coupling and stability of the Higgs potential require the Higgs mass to lie within a small allowed window, if the Standard Model is to survive up to the (reduced) Planck scale  $M_P \sim 2 \cdot 10^{18}$  GeV. Moreover, how would the unification of the Standard Model and gravitation be established at that scale? A subtle, but no less intriguing problem is the apparent smallness of the strong- $CP$  parameter, tightly bound from measurements of the neutron electric dipole moment, although no mechanism such as a symmetry in the Standard Model suggests such a small or even vanishing value. While the Standard Model features  $CP$  violation in the charged weak current, theoretical calculations show that the amount of  $CP$  violation is insufficient by many orders of magnitude to be at the origin of the matter–antimatter asymmetry currently observed in the visible part of the universe.<sup>1</sup>

The instability of the mass of the scalar Higgs boson against radiative corrections is denoted by the term ‘gauge hierarchy problem’, which also sets the scale at which new physics can be expected. It is — beyond the Higgs discovery and the strong Standard Model research programme — a primary motivation for the construction of the LHC. Indeed, if a Higgs boson with mass  $< 1$  TeV is discovered, the Standard Model is complete. However, when computing radiative corrections to the Higgs propagator, modifying the bare Higgs mass, such as  $t\bar{t}$  vacuum polarisation diagrams, or boson self-energies including the Higgs self-coupling, the corresponding loop integrals diverge. To solve them, a cut-off parameter  $\Lambda_{\text{cut-off}}$  is introduced to which the integrals are quadratically proportional. The cut-off parameter sets the scale where new particles and physical laws must come in, regularising the diverging integral.<sup>2</sup> However, above the electroweak scale we know of only two scales exhibiting new physics: grand unification of the

<sup>1</sup>We could thus ask ourselves what the role of the weak phase is in the evolution of the universe. Does it carry a hidden purpose? Or is weak  $CP$  violation a meaningless ‘accident of Nature’: because there are three generations and because all quark flavours have mass there is quark mixing with four parameters of which three are three Euler angles and one is a  $CP$ -violating phase. The phase is not constrained by a symmetry and thus of order one ( $68^\circ$  [9]). Perhaps without major implications for Nature.

<sup>2</sup>In a renormalisable quantum field theory, divergences in single loop integrals frequently occur, but they are always cancelled to all perturbative orders by other diagrams contributing to the full matrix element of the scattering process under study.

electroweak and strong forces ( $\approx 10^{16}$  GeV) and the Planck scale. A cut-off at such large energies would require an enormous amount of fine-tuning to keep the physical Higgs mass small and stable. What could be a ‘natural’ value for the scale  $\Lambda_{\text{cut-off}}$ ? The following three diagrams give the largest contributions to the Higgs radiative corrections and hence to the physical Higgs mass:  $t\bar{t}$  loop:  $-(3/8\pi^2)\lambda_t^2\Lambda_{\text{cut-off}}^2 \approx (2\text{ TeV})^2$ ; gauge-boson loop:  $(9/64\pi^2)g^2\Lambda_{\text{cut-off}}^2 \approx (0.7\text{ TeV})^2$ ; and Higgs loop:  $-(1/16\pi^2)\lambda^2\Lambda_{\text{cut-off}}^2 \approx (0.5\text{ TeV})^2$ , where we have used  $\Lambda_{\text{cut-off}} = 10\text{ TeV}$  everywhere, and where  $\lambda_t$ ,  $g$ ,  $\lambda$  are respectively CKM, weak, and quartic Higgs couplings. The total mass-squared of the Higgs is the sum of these contributions and the tree-level term. What would be the cut-off (= new physics) scales if only small ( $\sim 10\%$ ) fine-tuning were allowed? We would find  $\Lambda_{\text{top}} < 2\text{ TeV}$ ,  $\Lambda_{\text{gauge}} < 5\text{ TeV}$ , and  $\Lambda_{\text{Higgs}} < 10\text{ TeV}$ . To naturally cancel these divergences, new physics at the TeV scale should couple to the Higgs and should be related to the particles in the loop (top, gauge, Higgs) by some symmetry.

The gauge hierarchy problem denotes this fine-tuning of parameters, and the strong dependence of physics at the weak scale on the physics at (presumably) much higher scale: if the Higgs radiative corrections are cut off at the scale of gravity, why is the scale of electroweak symmetry breaking so different from the scale of gravity? Why is  $m_W \ll M_P$ ? Equivalently, why is gravity so weak? Possible solutions to the hierarchy problem include: (i) new physics appears not much above the electroweak scale and regularises the quadratic divergences, (ii) new physics modifies the running of the couplings, approaching grand unification to the electroweak scale, (iii) gravity is not as weak as we think, it is only diluted in our four-dimensional world but it is as strong as electroweak interactions in, e.g., five or more dimensions with Planck scale  $M_P^{(5D)} \mathcal{O}(\text{TeV})$ , or (iv) the theory is fine-tuned and the explanation for the parameter values is statistical rather than dynamic (anthropic principle).

From the above discussion we retain that the Standard Model is in crisis. Most Standard Model extensions, developed with the goal to solve the hierarchy problem and/or to provide a dark matter candidate, introduce new particles at the TeV scale. To find these, we need a new, huge collider providing hard particle collisions with centre-of-mass energy well above 1 TeV.

## 2 The Large Hadron Collider

In principle, one could accelerate protons circulating in a magnetic ring almost illimitably to higher and higher energy by continuously passing them through a radio-frequency field. The energy loss through synchrotron radiation of a proton in the Large Hadron Collider (LHC) amounts to a few keV per turn (compared to a few GeV per turn for electrons in the  $e^+e^-$  collider LEP2), which is about one hundred times smaller than the acceleration the proton receives per turn. In practice however, the proton energy in the collider ring is limited by the superconducting dipole magnets that guide the circular beams:  $E_{\text{proton}} \simeq 0.3 \cdot B \cdot r$ . Because the radius of the LHC is fixed ( $r = 4.3\text{ km}$ ), one must use as strong fields as possible (8.3 T, compared to approximately 4 T at the HERA and Tevatron colliders), and fill all free LHC sections with dipole magnets ( $\approx 2/3$ ).<sup>3</sup> Because the effective centre-of-mass energy of the hard parton collision depends on the parton energy density distributions in the proton, with long tails towards a large energy fraction, accumulating larger statistics due to a high instantaneous luminosity effectively increases the available kinematic reach of the proton–proton collider. High luminosity (beyond  $10^{33}\text{ cm}^{-2}\text{s}^{-1}$ ), and good machine and data-taking efficiency (of the order of  $10^7$  seconds good-quality data taking per year), are also required to search for rare events, such as processes involving the Higgs boson, especially if the Higgs is light (Higgs production is an electroweak process with large momentum transfer, which has a cross section roughly a billion times smaller than inelastic QCD (so-called ‘minimum bias’) processes), and also for studies of the nature of new physics phenomena if discovered. To achieve high luminosity ( $L$ ), strong currents are necessary, requiring dense proton bunches containing up to  $N = 110$  billion protons each (for comparison:  $1\text{ cm}^3$  of hydrogen contains  $\approx 10^{19}$  protons), and as many LHC bunches

<sup>3</sup>More precisely, the total number of dipole magnets in the LHC is 1232, each of which has a magnetic length of 14.3 m, giving a total length of 17 618 m. The effective ‘bending radius’ amounts thus to:  $17\,618/(2\pi) = 2804\text{ m}$ , and hence  $E_{\text{proton}} \simeq 0.3 \cdot B \cdot r \approx 7\text{ TeV}$ .



( $k$ ) as possible filled with protons (maximum of  $k = 2808$  bunches out of a total of 3564 bunches). The bunches are spaced by 25 ns from each other, corresponding to a distance of 7.5 m. High luminosity also requires that the protons be transversely squeezed by magnetic lenses to a small spot to increase the probability that two protons collide. The typical transverse beam size, determined by the square-root of the product of an amplitude function characterising the beam optics (varying throughout the ring), and the constant phase space volume (emittance), amounts to  $\sigma_x^* = \sigma_y^* = 16 \mu\text{m}$  at 7 TeV beam energy (for smaller beam energies, the beam emittance increases with  $\varepsilon \propto 1/\gamma_p$ , as does the beam spot size as  $\propto \sqrt{\varepsilon}$ ).<sup>4</sup> The luminosity value is obtained from the formula

$$L = \frac{kN^2 f}{4\pi\sigma_x^* \sigma_y^*}, \quad (1)$$

where  $f = 11.25 \text{ kHz}$  is the revolution frequency determined by the LHC circumference and the speed of light of the protons. We thus obtain  $L = 3.5 \cdot 10^{30} \text{ cm}^{-2}\text{s}^{-1}$  per bunch, reaching  $10^{34} \text{ cm}^{-2}\text{s}^{-1}$  when all bunches are filled.

The LHC acceleration chain involves several steps (see Fig. 2 for a schematic view). The injector complex consists of the LINAC-2, preaccelerating the protons to 50 MeV, followed by the Proton Synchrotron Booster (PSB) consisting of four superimposed rings accelerating the protons to 1.4 GeV. Two large circular rings further accelerate the protons to 26 GeV (Proton Synchrotron – PS) and 450 GeV (Super Proton Synchrotron – SPS), which is the LHC injection energy. The beams are transferred from the SPS to the LHC via two newly built 3 km transfer lines. The PSB–PS–SPS complex required significant upgrades to be able to provide beams with the appropriate intensity, size, and bunch distance. The injection chain is particularly delicate because any increase of beam emittance during injection will be ‘remembered’ by the protons in the LHC and lead to a reduction of the available peak luminosity and/or beam lifetime (thus increasing beam-related backgrounds and reducing the integrated luminosity the LHC can deliver during a proton fill). We note that in each acceleration step, the energy increase lies between a factor of 10 and 20, which are reasonable ranges for the dipole magnets. The injector also has the task of creating the proton bunches and (fixed) bunch pattern for the LHC. The chain is as follows: 6 booster bunches are injected into the PS; each of these is split into 12 smaller bunches giving a total of 72 bunches at extraction; between 2 and 4 batches of 72 bunches are injected into the SPS giving from 144 up to 288 bunches; finally, a sequence of 12 extractions of (up to) 288 SPS bunches is injected into the LHC, giving a maximum of 2808 bunches (39 groups of 72 bunches). The filling scheme (difference between the 3564 possible and 2808 actually filled bunches) foresees a number of short gaps for, e.g., kicker magnet rise times in the injection chain, and one long gap of 119 empty bunches ( $3 \mu\text{s}$ ) for the rise time of the LHC beam dump kicker magnet. Once injected into the LHC, the protons are accelerated from 450 GeV to 7 TeV in a 20-minute acceleration process, during which the protons receive an average energy gain of 0.5 MeV per turn when passing the electrical radio-frequency (RF) fields created in 8 superconducting cavities per beam with a peak accelerating voltage of 16 MV.

The LHC consists of eight 2.45-km-long arcs with bending dipole magnets (see Fig. 3 for a schematic drawing of a dipole section),<sup>5</sup> and eight 545-m-long straight sections. Four particle detectors have been constructed and are housed in huge underground caverns located at four of the straight sections. They record the objects left by collision debris by interacting with them. The detectors are: ATLAS (A Toroidal LHC Apparatus), CMS (the Compact Muon Solenoid), ALICE (A Large Ion Collider

<sup>4</sup>The free ‘volume’ occupied by each proton in the interaction point is of the order of  $10^{-4} \mu\text{m}^3$ , which is huge compared to the size of an atom, so that strong-interaction collisions between protons are still rare. The probability of two protons colliding can be estimated to be approximately  $4 \cdot 10^{-21}$ , so that with  $1.1 \cdot 10^{10}$  protons per bunch one finds  $\approx 50$  interactions per bunch crossing, of which, however, only one-half are inelastic.

<sup>5</sup>The LHC magnet systems consists of a total of 1232 superconducting dipoles (cooled with 120 tons of superfluid helium down to 1.9 K), in which currents of 12 kA create the required 8.33 T magnetic field; 392 focusing quadrupoles; and 3700 multipole corrector magnets.

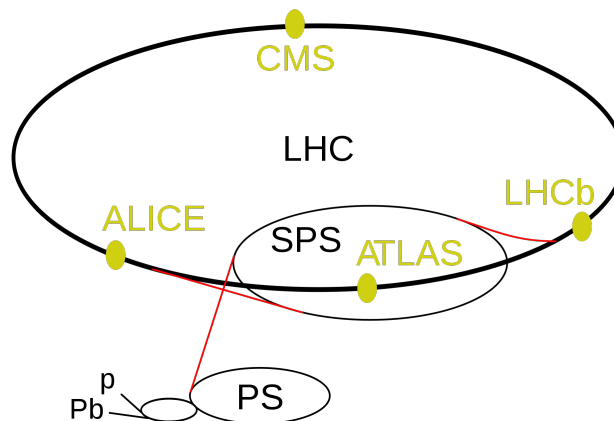


**Fig. 2:** Schematic view of the main elements of the LHC accelerator complex (see text) and the location of the four largest LHC experiments ALICE, ATLAS, CMS and LHCb.

Experiment), and LHCb (study of physics in  $B$ -meson decays at the LHC).<sup>6</sup> The remaining four straight sections are used by the RF cavities, the beam dump, and by two beam-cleaning systems using chains of collimators to absorb off-beam protons that would provoke magnet quenches and create so-called beam-halo backgrounds in the experiments. Although the energy of a single 7 TeV proton corresponds to only that of a flying mosquito ( $1 \mu\text{J}$ ), the total stored energy of 2808 bunches each filled with  $10^{11}$  7 TeV protons amounts to 360 MJ.<sup>7</sup> It is a huge challenge to control this energy and avoid damage to accelerator and experiments.

### 3 The high- $p_T$ general-purpose detectors ATLAS and CMS

The broad range of physics opportunities and the demanding experimental environment at high-luminosity 14 TeV proton–proton collisions impose unprecedented performance requirements and technological constraints upon the LHC particle detectors. ATLAS and CMS are general-purpose detectors, capable of adequately covering the entire physics programme reachable with high-luminosity 14 TeV proton–proton collisions: from charm and beauty physics at lowest transverse momenta ( $\sim 3 \text{ GeV}$ ), to new physics searches up to the highest reachable scales ( $\sim 4 \text{ TeV}$ ). The cross sections of the dominant QCD processes and those representing the primary physics channels for research differ by many orders of magnitude. For example, while at 14 TeV centre-of-mass energy, the total inelastic  $pp$  cross section amounts to approximately 70 mb (giving a 1 GHz event rate at  $L = 10^{34} \text{ cm}^{-2}\text{s}^{-1}$ ),<sup>8</sup> hard quark and gluon scattering into pairs of jets (or more) occurs roughly a thousand times less frequently; inclusive  $b$ -hadron production has a cross section of approximately 0.5 mb; inclusive  $W \rightarrow \ell\nu$  and  $Z \rightarrow \ell\ell$  boson production and decay have cross sections times branching fractions of approximately 20 nb and 2 nb,<sup>9</sup> respectively (compared to roughly a factor of 8 smaller at the Tevatron); top and antitop production has a cross section of almost 1 nb (rate of 10 Hz), two orders of magnitude higher than at the Tevatron; inclusive Higgs-boson production, dominated by gluon-gluon-to-Higgs fusion via a triangular top-quark loop, has a Higgs-

<sup>6</sup>In addition, there are two smaller experiments: TOTEM (Total Cross Section, Elastic Scattering and Diffraction Dissociation at the LHC) and LHCf (Large Hadron Collider forward) for very low- $p_T$  physics.

<sup>7</sup>The stored energy is sufficient to heat up and melt 12 tonnes of copper. It is equivalent to an Airbus A380 flying at 700 km/h speed, to 90 kg of TNT, 8 litres of gasoline, or 15 kg of chocolate.

<sup>8</sup>Recall that  $1 \text{ mb}^{-1} = 10^{27} \text{ cm}^{-2}$ .

<sup>9</sup>Because of the proton quark structure, producing more  $u\bar{d}$  than  $\bar{u}d$  quarks in scattering reactions, roughly a quarter more  $W^+$  than  $W^-$  are produced at the LHC [12] (while equal amounts of both charges are produced at the  $CP$  symmetric Tevatron collider).

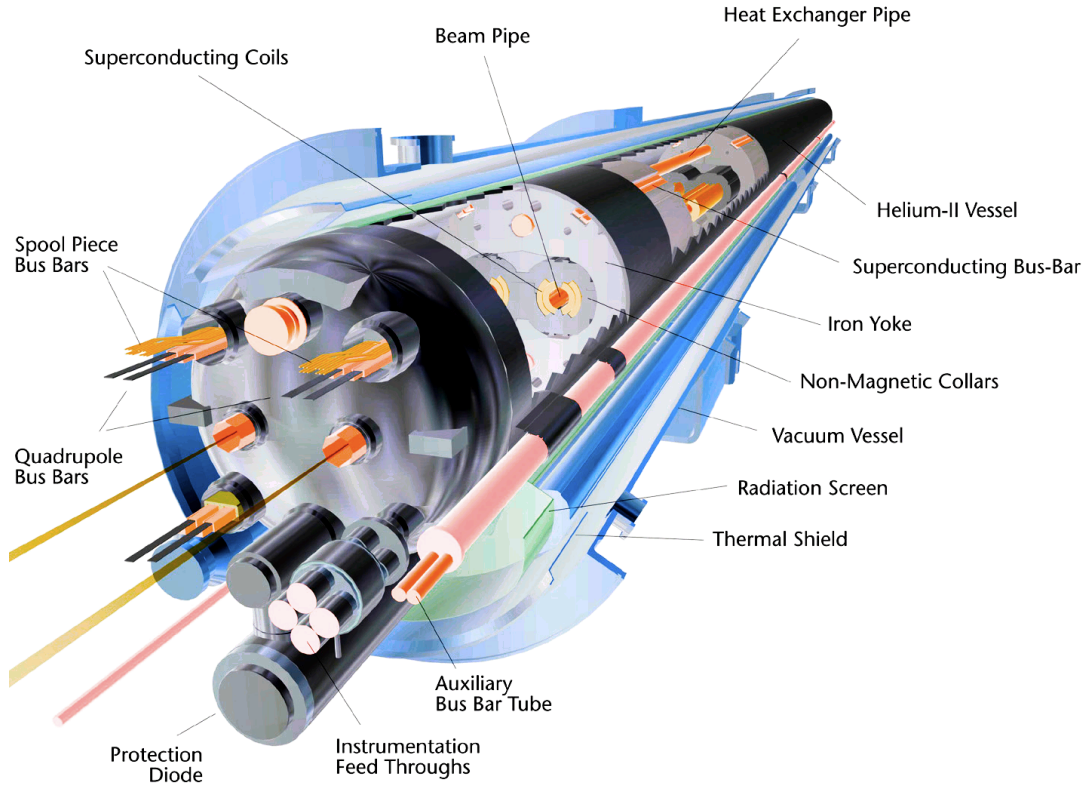


**Fig. 3:** Section view of a superconducting LHC dipole magnetic. The two beam pipes are wrapped into two oppositely poled superconducting coils.

mass dependent cross section between 45 pb ( $m_H = 120$  GeV) and 20 pb (180 GeV); and the production via gluon–gluon scattering of 1 TeV supersymmetric squarks and gluinos has a cross section of a few pb. These vast disparities, rendering physics analysis at the LHC like searching for needles in a giant haystack, drive the detector design.

Let us list some of the most outstanding LHC conditions and derive from these the corresponding design challenges.

- The 40 MHz bunch crossing rate<sup>10</sup> requires a fast trigger decision, precise timing and ‘pipeline’ electronics, locally storing readout data until the Level-1 (hardware) trigger response signal has been derived. For a pipeline memory depth of 100 bunch crossings, the Level-1 trigger latency must not exceed 2.5  $\mu$ s.
- The interaction rate of up to 1 GHz at maximum peak luminosity of  $10^{34}$  cm<sup>-2</sup>s<sup>-1</sup> (LEP and Tevatron:  $L_{\text{max}} = 10^{32}$  cm<sup>-2</sup>s<sup>-1</sup> and  $3.5 \cdot 10^{32}$  cm<sup>-2</sup>s<sup>-1</sup>, respectively), corresponding to approximately 25 inelastic interactions piling up in a single collision event, requires efficient pattern recognition to reduce the event rate from 1 GHz to 75 kHz (Level-1 output, high-level trigger input) to approximately 200 Hz (HLT output rate, events written to disk).
- The approximate data size of 1.5 MB per event together with the 200 Hz accepted trigger rate provides an average raw data throughput of 300 MB per second. Storage, worldwide distribution, prompt reconstruction and reprocessing of these data require adequate storage media, and powerful network and computing resources. The paradigm of distributed computing chosen by the LHC

<sup>10</sup>For comparison, the bunch crossing rates at LEP and the Tevatron are 45 kHz and 2.5 MHz, respectively, while the  $B$  factory PEP-II, an  $e^+e^-$  collider, has achieved 240 MHz, and the CLIC design foresees 2 GHz.

experiments requires the availability of several (order 10) large-scale computing centres (Tier-1s, demarcating ‘computing clouds’), with resources similar to those at CERN, and located representatively for the collaborations’ geographical extensions. These clouds embrace smaller computing centres for user analysis and simulation production.

- The irradiation rate after 10 years of successful LHC operation is expected to reach  $5 \cdot 10^{14}$  neutron equivalents per  $\text{cm}^2$  (300 kGy), requiring radiation-hard inner tracker (pixel detector with large signal-to-noise ratio and small silicon volume close to the interaction point) and forward calorimeter technology.
- The high charged multiplicity of up to 1000 tracks per event ( $4 \cdot 10^{10}$  tracks per second) requires the use of high-granular pixel/silicon or fine-grained straw tracker technologies. Three-dimensional pixel technology, replacing traditional silicon strip detectors close to the beam pipe, is mandatory to provide sufficient pattern recognition capability.
- Large background rates from beam-gas interactions, beam-halo muons, thermal neutrons and photons (‘cavern background’, bathing the detector during event pileup and afterwards due to activation of materials in the detector, its support structure, and the cavern), require precise muon timing, redundant pattern recognition, and radiation hardness.

Similarly, the detector design reflects the challenges posed by the physics programme.

- The search for rare  $B_{s(d)} \rightarrow \mu\mu$  decays, which have Standard Model branching fractions of  $3.3 \cdot 10^{-9}$  and  $1.1 \cdot 10^{-12}$ , respectively, and the measurement of time-dependent  $CP$  violation and the unitarity triangle angle  $\beta_s$  using (among others) flavour-tagged  $B_s \rightarrow J/\psi\phi$  decays, require good trigger efficiency and purity for muon tracks with transverse momenta as low as 3 GeV. To achieve sufficient purity, the HLT tracking algorithm must reconstruct charges as well as the  $B$  vertex and mass.
- Measuring the  $W$  mass to a precision better than the current world average [13] of  $(80.399 \pm 0.023)$  GeV, requires excellent alignment of the tracking detectors, good track reconstruction efficiency, calorimeter uniformity, and missing transverse energy resolution.
- A precision measurement of the top mass needs — apart from a better theoretical understanding of the nature of the measured top mass — excellent jet energy calibration, resolution and uniformity, as well as excellent  $b$ -tagging purity and efficiency.
- A sensitive search for the Higgs boson in the most promising final states  $2e(\mu)2\nu$ ,  $4e(\mu)$ ,  $2e2\mu$ ,  $\gamma\gamma$ ,  $\tau\tau$  (via weak boson fusion accompanied by forward jets) requires very pure and efficient particle identification, excellent electromagnetic and hadronic calorimeter resolution and uniformity, efficient high-luminosity tracking, and efficient reconstruction of forward jets.
- Searching for the multifaceted signatures from supersymmetry requires excellent jet and missing transverse energy resolution, low calorimeter noise, excellent  $\tau$  identification and reconstruction, as well as maximum detector acceptance.
- The search for heavy resonances of masses beyond 1 TeV, as they are predicted in models with excited weak bosons or extra spatial dimensions, requires good tracking (including charge reconstruction) and calorimeter resolution, and a large dynamic range (small calorimeter saturation) up to the highest reachable energies.

### 3.1 Detector design

The high- $p_T$  detectors, ATLAS and CMS, are designed as a result of careful optimisation processes to respond as well as possible to these unprecedented and sometimes conflicting requirements, while respecting budget limitations (approximately 550 million Swiss francs per detector). Both detectors have fast, multi-level trigger systems allowing one to select complex signatures, fast data acquisition based on broadband network switches, excellent inner tracking devices allowing efficient high- $p_T$  tracking

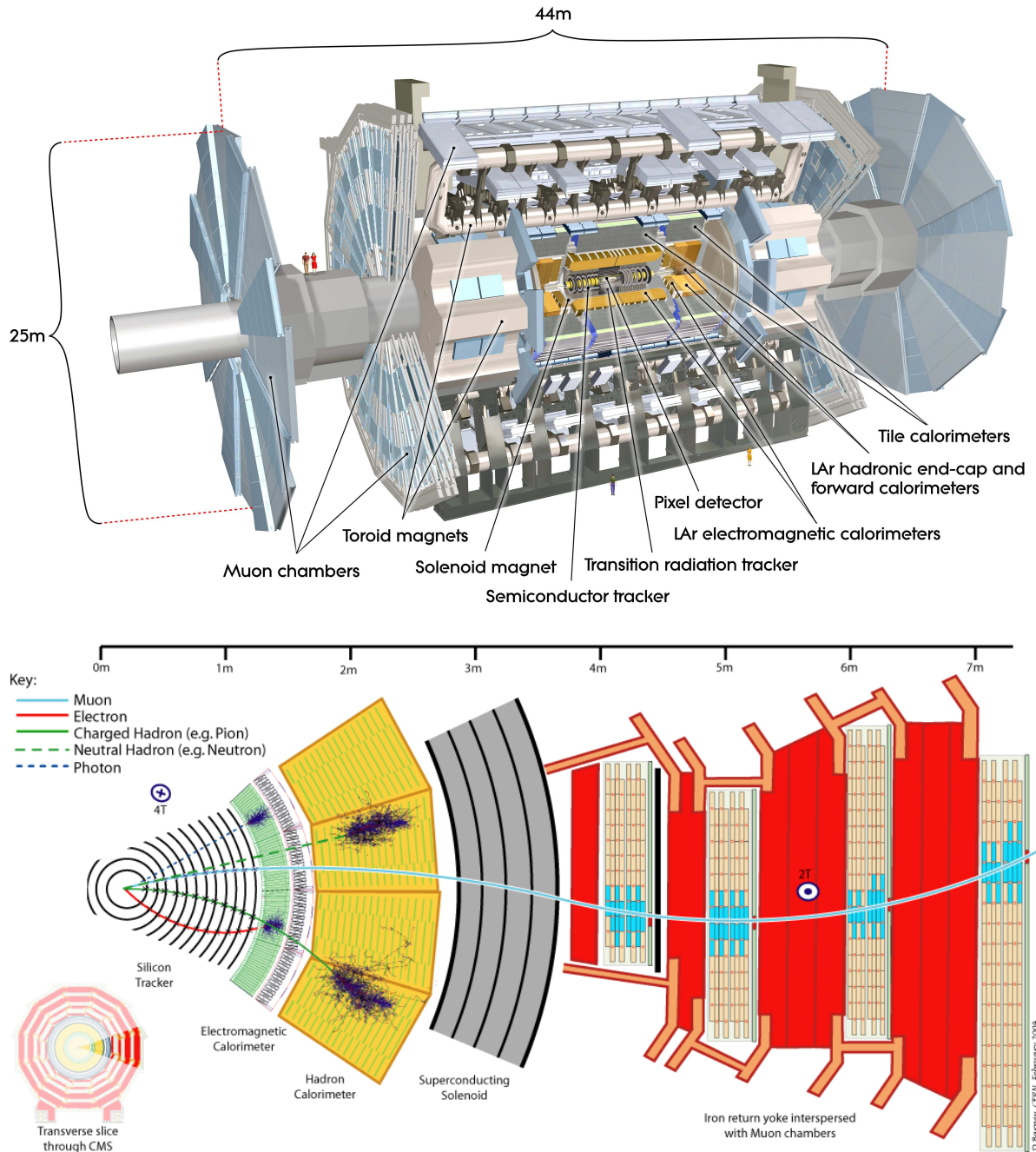


**Fig. 4:** Schematic drawings of the ATLAS detector (upper) and a slice of the CMS detector (lower), showing the trajectories of charged and neutral particles interacting with the various detector layers.

and secondary (*b*) vertex reconstruction in a high-luminosity environment; fine-grained, high-resolution electromagnetic calorimeters for excellent electron and photon reconstruction, complemented by full coverage hadronic calorimetry for accurate jet and missing transverse energy measurements, and an efficient identification of semileptonic  $\tau$  lepton decays; as well as high-precision muon systems with standalone tracking capability [1, 2, 14, 15]. Schematic drawings of the ATLAS and CMS detectors are shown in Fig. 4.

The most striking difference between ATLAS and CMS, strongly determining the entire detector design, is the **magnet structures**. CMS has a single, albeit huge solenoid (inner diameter 5.9 m, thick-

ness 60 cm, axial length 12.9 m), fully immersing the inner tracking systems and electromagnetic and hadronic calorimeters in a 3.8 T axial magnetic field<sup>11</sup> (18.2 kA current), and providing muon momentum measurement via the  $\sim 2$  T field in the flux return yoke made out of 10 000 tonnes of steel. ATLAS has three different magnet systems: a thin solenoid (inner diameter 2.46 m, thickness 5 cm, axial length 5.8 m, axial magnetic field 2 T at the centre of the tracking volume, 7.7 kA current) around the inner tracking system, and 8 barrel and  $2 \times 8$  endcap air-core toroid magnets (magnetic fields between 0.5 T and 4 T, strongly varying with the radial distance from the toroids, 20.5 kA currents), arranged radially around the hadron calorimeters such that the Lorentz force bends charged tracks along their  $z$  coordinates. The toroid magnets do not affect the central solenoid field. All magnet systems are superconducting.

The **inner tracking systems** are made out of semiconducting silicon pixel and silicon strip detectors for the inner and outer layers (disks in the endcaps), respectively, comprising approximately 80 million channels. Pixel systems close to the collision impact point are mandatory to cope with the large track density. The innermost barrel pixel layer, of a total of 3 layers, is as close as 5.0 cm (ATLAS) and 4.4 cm (CMS) to the beam line. The design  $R\phi$  position resolution of the pixel system is  $10 \mu\text{m}$ . In CMS silicon strip technology is used to cover the entire inner detector between pixel and electromagnetic calorimeter (radius of the outermost layer: 107–110 cm), providing a total of 14 measurement points. The ATLAS silicon strip detector, being shorter in radius, provides 8 measurement points. A transition radiation tracker made of 350 000 Kapton straw tubes of 4 mm diameter, providing on average 35 measurement points for pseudorapidity<sup>12</sup> lower than 1.8 (resolution of  $130 \mu\text{m}$  per straw), and between 18 and 35  $R\phi$  measurement points (no  $\eta$  measurement) between  $1.8 \leq |\eta| \leq 2.5$ , is inserted between the silicon strip tracker and solenoid. Transition radiation with 8 keV photons on average, emitted when charged ultrarelativistic particles traverse the boundary of two different dielectric media (foil and air), increases the signal size so that dual readout with low and high thresholds allows the identification of  $\beta = 1$  particles (electrons).

Owing mainly to the stronger solenoid magnetic field, CMS has better momentum resolution with  $\sigma(p_T) \simeq 1.5\%$  compared to 3.8% (ATLAS) for 100 GeV tracks at  $\eta = 0$ . At low momentum, multiple scattering that occurs due to the significant material in the tracking systems of both detectors (varying between  $0.3X_0$  at  $\eta \simeq 0$  and  $1.4X_0$  at  $\eta \simeq 1.5$ ) reduces this difference.

The **electromagnetic calorimeters** consist of a lead and liquid-argon sampling technique, radially shaped as an accordion to minimise inhomogeneities and cracks, chosen by ATLAS, versus high-granular lead tungstate ( $\text{PbWO}_4$ ) scintillating crystals in CMS (61,200 crystals in the barrel and 7,324 in each endcap). Both calorimeters have a geometry pointing towards the collision point, which simplifies the energy reconstruction of the incident particles. The lead absorber in the ATLAS calorimeter reduces the available light yield for energy measurement, thus limiting the stochastic resolution to  $\sigma(E) \simeq 10\text{--}12/\sqrt{E}$  with a constant term of 0.2–0.35%, compared to  $\sigma(E) \simeq 3\text{--}5.5/\sqrt{E}$  and a constant term of 0.5% for the CMS crystals. The influence of the constant term, originating from non-uniformities in the calorimeter response due to inhomogeneities and non-linearities, is small for ATLAS, while it becomes a limiting factor at energies beyond 40 GeV for CMS (hence, for example, affecting the measurement of  $H \rightarrow \gamma\gamma$ ). While CMS has only a single electromagnetic layer, the ATLAS calorimeter is longitudinally segmented in four layers (including the presampler, which corrects the measured energy for early electromagnetic showers in solenoid and cryostat), permitting one to measure the shower development and so distinguish electromagnetic from hadronic showers. It also allows one to reconstruct the direction of the incoming

<sup>11</sup>The solenoid is designed to deliver a 4 T field. Longevity considerations have however led to the decision to decrease the current from 19.5 kA to 18.2 kA, reducing the field to 3.8 T.

<sup>12</sup>The pseudorapidity is defined by

$$\eta \equiv -\ln\left(\tan\frac{\theta}{2}\right) = \frac{1}{2}\ln\left(\frac{|\mathbf{p}| + p_L}{|\mathbf{p}| - p_L}\right), \quad (2)$$

where  $\theta$  is the polar angle between the particle momentum  $\mathbf{p}$  and the beam axis ( $z$ ), and  $p_L$  is the longitudinal component of  $\mathbf{p}$ . In hadron collider physics, the pseudorapidity is preferred over the use of the polar angle because particle production is constant as a function of the pseudorapidity.



particle. The cell granularity for the ATLAS main sampling layer is  $\Delta\eta \times \Delta\phi = 0.025^2$  rad, improved in  $\eta$  by fine strips with  $\Delta\eta = 0.003$  (barrel number) in front of the main sampling layer to help identifying  $\pi^0$ . CMS has a crystal granularity of  $\Delta\eta \times \Delta\phi = 0.017^2$  rad in the barrel, and  $0.018 \times 0.003$  to  $0.088 \times 0.015$  in the endcaps. Saturation of the energy reconstruction occurs for energy depositions beyond 3 TeV (ATLAS) and 1.7 TeV (CMS). Biases due to saturation are corrected but lead to a decrease in the energy resolution.

The **hadronic calorimeters** use similar sampling techniques, based on iron (ATLAS) and brass absorbers (CMS) and scintillating tiles read out via wavelength shifting optical fibres guiding the light to photomultiplier tubes. The main difference in performance originates from the strong constraint imposed by the maximum achievable size of the CMS solenoid, resulting in a barrel hadronic calorimeter with insufficient absorption (radiation length of  $7.2\lambda$  at  $\eta = 0$  for all calorimeter layers including the crystals, compared to  $9.7\lambda$  for ATLAS) before the coil. A tail catcher had to be added around the CMS coil to complete the hadronic shower reconstruction and provide better protection against punch-through to the muon system, faking muons. The reduced sampling fraction of CMS versus ATLAS leads to an approximately twice worse jet resolution of  $100\%/\sqrt{E}$  for CMS, and a worse constant term of up to 8% in the barrel. It similarly affects the missing transverse energy resolution. Energy flow algorithms, attempting to replace charged hadrons in the shower by the corresponding measurement in the inner tracker, improve the energy resolution for hadrons and jets, in particular at low energies.

Hermeticity of the detectors for an excellent missing transverse energy measurement, but also to tag forward jets occurring, for example, in weak boson fusion processes, requires calorimeter coverage up to the very forward direction. The **forward calorimeters** of ATLAS and CMS extend the energy measurement to pseudorapidities of 5 (polar angle of 0.77 degrees). They are located in different parts of the detector. The ATLAS forward calorimeter, made of copper and tungsten absorbers with gaps filled with liquid argon, is fully integrated into the cryostat that houses the end-cap calorimeters, which reduces the neutron fluence in the muon system and, with careful design, has minimal impact on the neutron fluence in the inner tracker. The CMS forward calorimeter, made out of steel and quartz fibres and operating with Cherenkov light, is situated 11 m from the interaction point, thereby minimising the amount of radiation and charge density during operation.

Driven by the design of the magnets, the **muon systems** strongly differ between ATLAS and CMS. While CMS measures muons within the instrumented flux return, requiring the extrapolation of the track into the inner tracker, ATLAS has standalone muon tracking inside the large area spanned by the air-core toroids. Both experiments use drift tubes and cathode strip chambers (forward direction) for the precision muon measurements, and fast resistive plate chambers (thin gap chambers in the ATLAS endcaps) for fast muon Level-1 trigger signals. The pseudorapidity coverage amounts to  $|\eta| < 2.7$  (2.4) for ATLAS (CMS) for muon measurements, lowering by 0.3 units for triggering. The combined momentum resolution for a 100 GeV (1 TeV) track at  $\eta = 0$ , reconstructed in the inner tracker and muon systems, is  $\sigma(p_T) \simeq 2.6\%$  (10.4%) (ATLAS) and  $\sigma(p_T) \simeq 1.2\%$  (4.5%) (CMS). The resolution significantly deteriorates in CMS for forward muons due to the reduced bending power of the solenoid (6 T.m at  $|\eta| = 2.5$  compared to 16 T.m at  $\eta = 0$ ).

Apart from these main detector systems, both ATLAS and CMS have dedicated luminosity detectors in their forward regions.

In summary, we may recall that ATLAS has put emphasis on excellent jet and missing transverse energy resolution, particle identification, and standalone muon measurement, while CMS has prioritised excellent electron, photon and tracking (muon) resolution. Both detectors have good hermeticity (very few ‘cracks’).

References [1, 2] present the essential performance parameters of the ATLAS and CMS experiments, sub-divided into track reconstruction, muon, electron and photon identification and reconstruction, jet and hadronic tau reconstruction, *b*-flavour tagging and the trigger selection (see below). Many of the results given are supported by existing test beam and cosmic ray measurements (also discussed in

these lecture notes), in particular for the single-particle response of the detector elements to electrons, photons, pions and muons at various benchmark energies. Others rely on the simulation of the detector response and the underlying physics processes. They are affected by numerous uncertainties also due to hard-to-quantify soft-QCD and machine background effects.

### 3.2 Trigger and data acquisition

In former times, when particle physics experiments used bubble and cloud chamber techniques, data acquisition (DAQ) was made by means of stereo photographs. There was effectively no trigger. Instead, each bubble expansion was photographed based on the constant (and known) accelerator cycle. The high-level trigger was *human*, realised by scanning teams operating worldwide with varying trigger efficiencies (rumours claim that physicists had the worst scanning efficiency). The slow operation rate of this setup allowed one to measure only the most common processes. Later, electronic signals were used to trigger the camera to photograph an event (a single trigger level). The dead time occurred while the film advanced after a trigger.

The trigger [16] is a function of the fast detector response to a collision event providing a binary accept or reject signal. Its task is to look at (almost) all bunch crossings and select the most interesting ones. Data acquisition (DAQ) collects all detector information and stores it for offline analysis. Requirements for a DAQ system are the provision of online services, such as a state machine ('Run Control'), governing the run sequences, and data quality monitoring. It must keep records of the detector configuration and run conditions, avoid corruption or loss of data (and hence verify the data sanity), be robust against imperfections in the detector and associated electronics and readout systems, and minimise dead time.<sup>13</sup> Because the trigger latency even for the fastest level is longer than the 25 ns bunch crossing period, the electronics signals need to be saved locally in so-called pipelines until the trigger signal arrives.

A problem for any trigger at the LHC is that one cannot (and does not want to) save all events. 'Old' (known) physics occurs more often than 'new' physics, i.e., the new physics is buried under huge amounts of old physics. We have seen that the interesting physics occurs at rates of 10 Hz (for top antitop production) and below at highest peak luminosity. The remit is thus to keep *all* of those events, while rejecting most of the others. One exception to this is low-mass flavour physics, which — although being 'old' — has still important potential for discoveries. We hence must aim at fitting the best possible physics cocktail into the available bandwidth. Efficient selection and background rejection requires one to include the response of the entire detector in the trigger decision. This can only be achieved by splitting the trigger decision into several levels with increasing complexity. The first level has short latency and high efficiency and must only aim at the rejection of the 'obviously' uninteresting events (once rejected, events are rejected forever!). Later levels, which can be slower thanks to the rejection in the previous level, perform fine-grained selection and rejection.

The trigger systems of ATLAS and CMS are separated into a first-level ultra-fast hardware trigger, based on information from the calorimeters and dedicated muon systems only. The detector data are transferred to large buffer memories after a Level-1 accept. The data rates to DAQ and the next level triggers are massive: with approximately 1 MB event size at 100 kHz event rate one has a rate of 100 GB/s (i.e., 800 Gbit/s). The subsequent high-level trigger (HLT) uses partial event data readout or powerful network switches to feed reconstruction and software selection algorithms running on farms

<sup>13</sup>Dead time is the fraction of time where valid interactions could not be recorded for various reasons. Typical system-imminent dead time is of the order of up to 10%. It originates from the readout and trigger system, from operational dead time (e.g., the time to start and stop a run or to configure the detector systems), trigger or DAQ down-time (e.g., following computer failure), or detector down-time (e.g., following a high-voltage trip). For a multi-level trigger, the total dead time is the sum of the dead times of all levels. The trigger dead time for a given level is computed from the product of the trigger rate of the previous level and the latency for this level. The readout dead time is given by the product of the final (highest-level) trigger rate and the local readout time. Note that trigger dead-time logic is *required* to prevent triggering another event before the detector has been fully read out. Given the investment in the accelerators and the detectors for a modern HEP experiment, it is clearly important to keep dead time to a minimum.



with several thousand central processing units. In ATLAS the HLT is separated into two independent steps. A fast Level-2 trigger using only detector information from so-called ‘regions of interest’, which are sections along azimuthal and pseudorapidity cuts around triggered Level-1 objects, and including only the detector systems required by the Level-2 algorithm. The Level-2 decision must come within a few milliseconds and reduce the outgoing Level-1 rate from 75 kHz to 2 kHz, which is the input rate to the event builder requiring to read out the full detector. A subsequent Level-3 trigger (‘Event Filter’) then further reduces the event rate to approximately 200 Hz, which is written to disk. These events are promptly reconstructed at CERN and, in parallel, distributed to 10 worldwide computing centres. In CMS, the large HLT input rate is tamed by factorising the event building into a number of slices each of which sees only a fraction of the rate. This requires a large and expensive total network bandwidth, but avoids the need for a very large single network switch.

An important requirement for the event building is a proper timing-in of the various detectors. Indeed, within the 40 MHz bunch crossing rate, particles can only travel 7.5 m through the detectors, which are significantly larger than that (ATLAS has a height of  $2 \times 11$  m and a length of  $2 \times 23$  m). In addition, the collection of the detector signals, notably in the large muon drift tubes, can take up to 40 bunch crossings ( $1 \mu\text{s}$ ). To properly collect the signals belonging to the same bunch crossing (i.e., ‘event’) and to keep the exposure time per event as small as possible, trigger-decision and detector response collection delays must be aligned to a few nanoseconds. Timing-in is one of the first commissioning tasks for all detector systems.

#### 4 Detector commissioning — Overview

All detector systems, as well as the performance and physics groups developed detailed commissioning strategies for initial running with colliding beams. Even before beams collide in the LHC, as more and more systems are being installed, extensive stand-alone and combined studies with cosmic ray events and detector calibrations are performed. These studies as well as dress rehearsals using simulated data exercise the full data acquisition chains, including the online and offline data quality assessment tools, and the streaming of the events into several physics and calibration streams based on the trigger decision.

The cosmic ray data provide important information to align the detectors relative to each other (but not relative to the beam axes). They set an initial reference geometry for most of the barrel muon detector, and will be used to correct the alignment based on precise survey data and optical sensors. Muons from beam halo data taken during single-beam LHC commissioning runs will be used as an initial validation of the end-cap muon detector alignment. For example, in ATLAS the magnetic field strengths of the toroids, determining the muon energy scale, are known to better than 0.5% versus  $\phi$  from survey data of the measured coil positions. Later the precision can be improved to 0.1–0.2%, using a system of Hall probes. The field of the solenoid immersing the inner detector has been mapped to a precision of a few Gauss, which approaches the design goal.

Charge injection or pulsed calibrations of the electronic boards and pedestal runs provide initial settings for channel thresholds, ramp and delay values, pedestals, etc. for the various systems, and are used to map noisy and to some extent dead channels. Hadronic calorimeters also perform calibration with laser-light and radioactive caesium sources. These tasks together with test beam measurements contribute to achieving a sufficient quality of the first collision data.

As an example, the ATLAS operational status as of autumn 2009 is given in Table 1. The experiment’s start-up and ultimate design goals in terms of the tracking and calorimeter performance are summarised in Table 2.

With the start-up of the LHC,<sup>14</sup> and after timing-in the detector systems with the colliding LHC bunches and the trigger signal, minimum bias triggers from scintillator counters will provide Level-1

<sup>14</sup>All event numbers given in this overview section refer to 14 TeV LHC centre-of-mass energy. The impact from lower centre-of-mass energies (10 TeV and 7 TeV) is briefly discussed in Section 11.

**Table 1:** Number of channels and operational status as of autumn 2009 of the ATLAS subdetectors.

ATLAS subdetector	Number of channels	Operational fraction (%)
Pixel Tracker	80 million	97.9
Silicon Strip Tracker	6.3 million	99.3
Transition Radiation Tracker	350 000	98.2
Liquid-Argon Electromagnetic Calorimeter	170 000	98.8
Tile Hadronic (Extended) Barrel Calorimeter	9800	99.2
Hadronic Endcap Liquid-Argon Calorimeter	5600	99.9
Forward Liquid-Argon Calorimeter	3500	100
Muon Drift Tubes	350 000	99.7
Muon Cathode Strip Chambers	31 000	98.4
Barrel Muon Trigger	370 000	98.5
Endcap Muon Trigger	320 000	99.4
Level-1 Calorimeter trigger	7160	99.8

accepts for initial physics studies at a luminosity less than or equal to  $10^{31} \text{ cm}^{-2}\text{s}^{-1}$ . These events can be used to provide first occupancy tests of the inner tracking systems, and to refine the dead channel maps. Copious isolated tracks from minimum bias events will allow the experiments to refine the inner detector alignment using the distributions of residuals between measured hits and fitted tracks, and the comparison of  $E/p$  for pions of opposite charge. Alignment monitoring information will also be derived from  $K_S^0$  and  $\Lambda$  invariant mass and azimuthal decay vertex distributions. The  $K_S^0$  invariant mass together with the known, ideally uniform decay-angle distribution can be used for a data-driven determination of the tracking efficiency. In ATLAS, high and low threshold transition radiation hits from isolated pion tracks will be compared to the expectation from simulation. Minimum bias events will help both experiments to monitor the uniformity of the calorimeter response, which can be done azimuthally and by comparing positive and negative pseudo-rapidity regions. In this initial phase it will also be possible to some extent to validate the calorimeter simulation by comparing shower shapes for isolated hadronic tracks and low energetic jets. The statistics corresponding to a few days of low-luminosity data taking without toroid fields will allow the collection of enough straight muon tracks to calibrate the ATLAS muon optical alignment system to better than  $100 \mu\text{m}$ . It will be improved to up to  $30 \mu\text{m}$  at higher luminosity, which is required to take full advantage of the spatial resolution of  $40 \mu\text{m}$  per muon chamber, providing a 10% measurement of 1 TeV muon tracks.

While the trigger system is being commissioned, simple inclusive Level-1 calorimeter and muon triggers will be included first, followed by more complex Level-1 triggers, involving, for example, isolation and missing transverse energy. At the same time, the HLT systems will begin to operate, initially in pass-through mode, allowing the experiments to test the algorithms, and later using the full power of the HLT, while continuing to run pre-scaled triggers in pass-through mode. Combinations of pre-scaled multi-threshold triggers will be used to determine efficiency curves for the three trigger levels (so-called ‘bootstrapping method’). The data collected with the complete low-luminosity trigger menu will contain copious quantities of low-energy leptons from heavy quark decays and also from direct  $J/\psi$  and  $\Upsilon$  production. Approximately  $5000 W \rightarrow \mu\nu$  and  $500 Z \rightarrow \mu\mu$  decays should be reconstructed per  $1 \text{ pb}^{-1}$  of integrated luminosity (the expected rates are somewhat lower for electrons). The low-luminosity trigger menu will also provide abundant samples of high- $p_T$  jets, prompt photons mainly from  $\gamma$ -jet events, and semileptonic  $\tau$  decays.

**Table 2:** Expected calibration and alignment accuracies at the LHC start-up and the ultimate design goals for the ATLAS experiment. Examples for physics channels or measurements driving the requirements are given in the last column.

	Start-up of LHC	Ultimate goal	Physics goals
EM energy uniformity	1–2%	0.7%	$H \rightarrow \gamma\gamma$
Electron energy scale	$\sim 2\%$	0.02%	$W$ mass
Hadronic energy uniformity	2–3%	$< 1\%$	Missing $E_T$
Jet energy scale	$< 10\%$	1%	Top-quark mass
Inner detector alignment	50–100 $\mu\text{m}$	$< 10 \mu\text{m}$	$b$ tagging
Muon spectrometer alignment	$< 200_{\text{barrel}} \mu\text{m}$	30 $\mu\text{m}$	$Z' \rightarrow \mu\mu$
Muon momentum scale	$\sim 1\%$	0.02%	$W$ mass

All these events will be crucial for the initial validation of the detector performance. More specifically, the inner detector material can be mapped with photon-to- $e^+e^-$  conversions to order 1% with the statistics available after a few months of data taking. This procedure can be validated by studying the momentum dependence of the reconstructed invariant masses of low-mass resonances. Inclusive electrons can be used to test bremsstrahlung recovery in the inner detector. The inner detector alignment is expected to converge to the relative design accuracy of approximately 10  $\mu\text{m}$  soon after the full detector commissioning has started (the alignment with cosmic ray events will be insufficient in the endcaps), allowing the constant term in the tracking resolution to be below 20% of the full resolution. Local inner detector misalignment can be studied with the use of resonances with known masses and lifetimes decaying to lepton pairs, and with high- $p_T$  muons in combined track fits with the muon spectrometer.

Preliminary electromagnetic inter-calibration can be obtained at low luminosity using the azimuthal and  $\pm\eta$  symmetry of inclusive isolated electrons from various sources. It is, however, not clear whether this procedure improves the intrinsic electromagnetic calorimeter inter-calibration determined in test beams at the higher energy scales of interest for most of the physics analyses (it will be useful for CMS where only 9 out of 36 supermodules of the electromagnetic calorimeter could be calibrated in the H4 test beam, see Section 5). The ultimate high-energy electromagnetic inter-calibration will use  $Z \rightarrow ee$  events, requiring about 100  $\text{pb}^{-1}$  recorded integrated luminosity to significantly improve the expected initial uniformity of 1–2% to a statistical precision of  $\sim 0.7\%$  (ATLAS) with high granularity, provided the inner detector material is well enough understood. These events will also serve to calibrate the global electromagnetic energy scale.

Hadronic track and jet inter-calibration will employ  $E/p$  measurements (assuming an aligned inner tracker) and  $E_T$  balancing in di-jet,  $\gamma$ -jet and also  $Z$ -jet events, versus  $\phi$ . The latter two channels also determine the global jet energy scale with an expected precision better than 5% after a few months of data taking. Di-jet events will also be used to validate the forward  $E_T$  scale and resolution. The expected number of  $\sim 500$  fully reconstructed  $t\bar{t}$  events for 100  $\text{pb}^{-1}$  with one  $W$  decaying hadronically and the other one leptonically (electron or muon) allows a first calibration of narrow jets with invariant mass fits to  $W \rightarrow qq'$  decays. It will also be important to study the stability of the electromagnetic and hadronic cluster reconstruction with respect to varying calorimeter noise (significant event pileup is expected to occur only above peak luminosities of  $\mathcal{O}(10^{33} \text{ cm}^{-2}\text{s}^{-1})$  for the nominal LHC bunch pattern scheme).

The performance of heavy-flavour jet tagging crucially relies on locally aligned silicon detectors. Flavour tagging will be calibrated using  $t\bar{t}$  events, but initially also using orthogonal information from tagging algorithms based on track fits and soft-muon reconstruction in di-jet events.

One of the most difficult detector observable to measure accurately is missing transverse energy

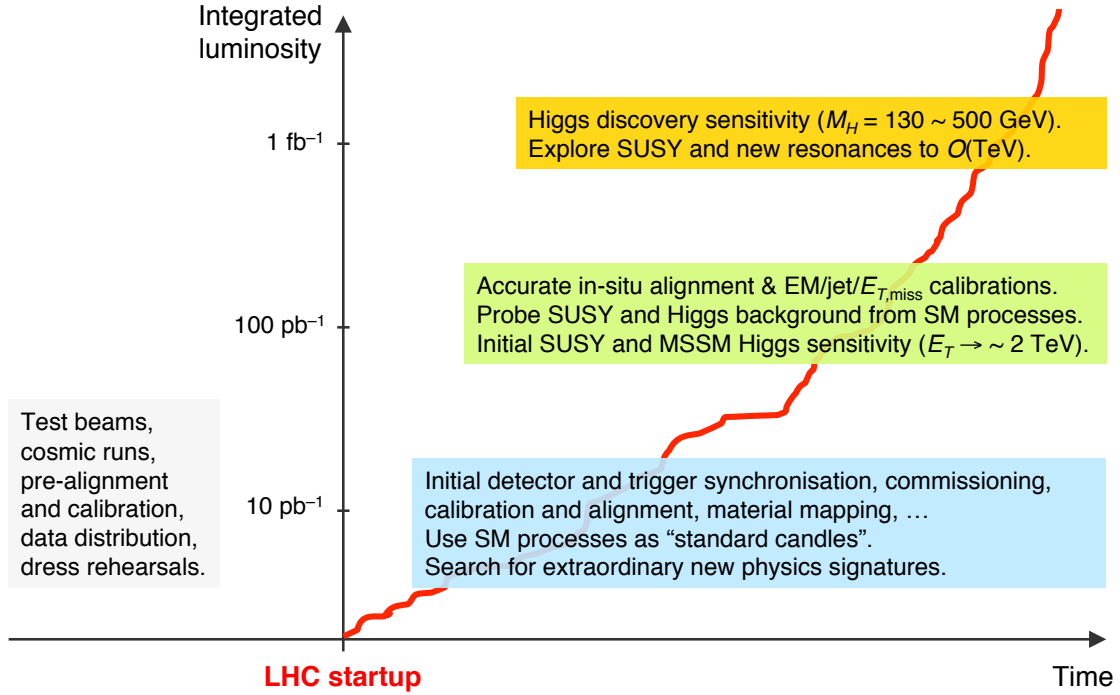


**Fig. 5:** Sketch for a commissioning and early physics roadmap at the LHC.

( $\cancel{E}_T$ ). Because it is sensitive to many new physics signatures, the tails of its distribution, dominated by resolution and instrumental effects, must be precisely calibrated with data before they can be used for discrimination and reconstruction purposes. The computation of  $\cancel{E}_T$  requires the cleaning of the event from beam halo muons, beam gas collisions, cavern background, and cosmic rays. Moreover, the calorimeter cells must be calibrated (for both electromagnetic and hadronic showers), and deficient calorimeter cells (including noise) must be mapped and corrected. Initial data-driven  $\cancel{E}_T$  studies will use minimum bias events, analysing the  $\cancel{E}_T$  resolution as a function of the  $E_T$  sum and comparing it with the expectation from simulated data, the transverse  $W$  mass in  $W \rightarrow e(\mu)\nu$  events,  $Z \rightarrow ee(\mu\mu)$  events, and, with rising statistics, mass-constrained  $t\bar{t}$  and  $Z \rightarrow \tau\tau$  events decaying to charged leptons and hadrons (approximately 7000 of the latter events with  $p_T(\mu) > 15$  GeV are expected in  $100 \text{ pb}^{-1}$ , allowing one to calibrate the absolute  $\cancel{E}_T$  scale to about 5%).

For muon tracks, the correlation of muon spectrometer and inner detector provides powerful reconstruction cross-checks for both systems. The muon reconstruction efficiency for stand-alone (muon spectrometer or inner detector only) and combined tracks can be determined with  $Z \rightarrow \mu\mu$  events by reconstructing one muon and probing the reconstruction of the other one (‘tag-and-probe method’). The muon fake rate, expected to be negligible at low luminosity, will become significant above  $10^{33} \text{ cm}^{-2}\text{s}^{-1}$ , due to the neutron and photon background in the cavern. The fake rate concentrates, however, at very low  $p_T$ , and remains small enough so that the impact on most physics analyses should be negligible. The overall muon energy scale will be calibrated with  $Z \rightarrow \mu\mu$  events, where a statistical precision of 0.8% and reasonable geometrical granularity can be reached with  $100 \text{ pb}^{-1}$  integrated luminosity. With more data available, local misalignment problems in towers of chamber triplets could also be resolved with  $Z$ -mass constraints. A sketch for the commissioning and early physics roadmap at the LHC is displayed in Fig. 5.

Initial physics measurements will primarily focus on Standard Model processes with high cross-sections. Among these are the multiplicity and pseudo-rapidity distribution of minimum bias events and cross sections of events with jets. Low- $p_T$  physics mainly dedicated to the study of  $B_s$  decays will

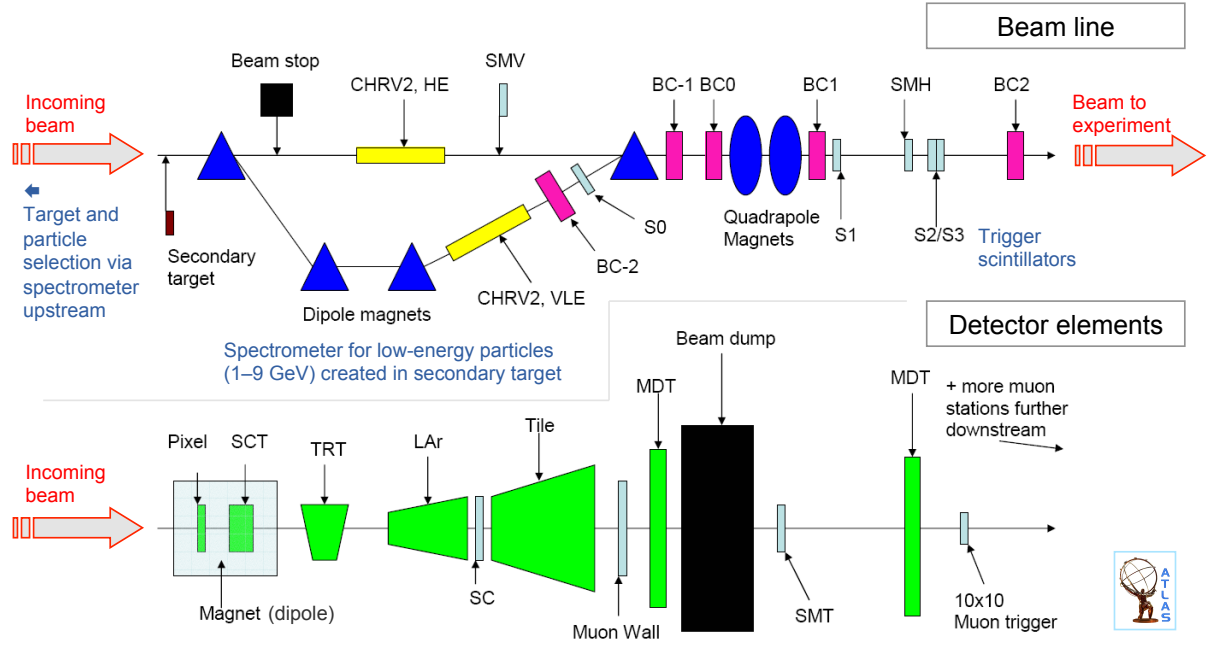


**Fig. 6:** H8 beam line of the ATLAS combined test beam 2004. Protons from the SPS, accelerated to 450 GeV energy, hit a target producing hadrons, electrons and muons with energies in the range of 1 to 350 GeV, which are selected upstream by a mass spectrometer. The composition of the incoming monochromatic particle beam is measured with Cherenkov counters (upper picture). The beam is focused and passes trigger scintillators before entering a complete ATLAS barrel slice (lower picture) with realistic geometry composed of Pixel and silicon strip detector (SCT) layers, immersed in a 1.4-T magnetic dipole field parallel to the beam, a transition radiation tracker (TRT) module outside the magnetic field, liquid-argon electromagnetic and tile hadronic calorimeter layers, interleaved with a scintillator to measure the energy lost in the liquid argon cryostat, and a series of muon drift tube and resistive plate chambers before and after a beam dump block.

begin by measuring  $J/\psi$  to  $Y$  cross section ratios, which involves the validation of vertexing tools, and cross sections and lifetimes of  $B$ ,  $B_s$  and  $\Lambda_b$  mesons using decays to  $J/\psi$ . Statistically competitive lifetime measurements for these mesons can be expected with  $\sim 100 \text{ pb}^{-1}$  integrated luminosity. The cross section of  $t\bar{t}$  production using semileptonic decays can be measured to a precision better than 20% with  $100 \text{ pb}^{-1}$  integrated luminosity, without requiring  $b$  tagging. Moreover, a significant single-top signal is expected to be seen in this data sample. Analyses aiming at searches for new phenomena will initially concentrate on the understanding of the detector performance and Standard Model processes, using calibration channels and studying phase space areas where new physics contamination is expected to be small.

The subsequent sections describe in some detail several of the commissioning and early physics studies mentioned above.

## 5 Commissioning with test beams

Both ATLAS and CMS have performed series of measurements with test beams of known energies and particle types. Electrons, photons, muons, pions, protons with energies between 1 and 350 GeV and varying magnetic field configurations were collected to test the tracking efficiency, alignment and particle identification, (inter-)calibrate the electromagnetic and hadronic calorimeters, test the muon trigger efficiency, tune Monte Carlo simulation, etc.

Figure 6 shows a sketch of the ‘H8’ beam line used for the ATLAS 2004 combined test beam.

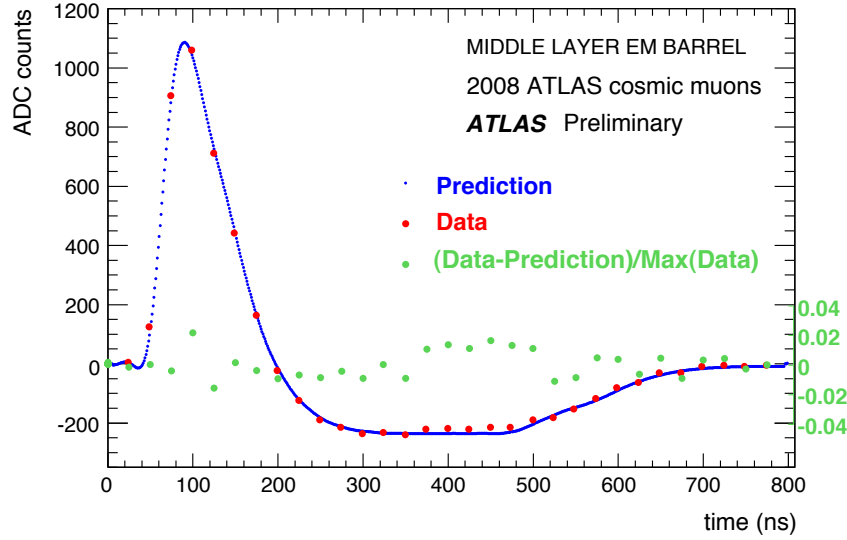


**Fig. 7:** Digitised bipolar ionisation pulse shape of a 15 GeV cosmic-ray signal measured in the middle layer of the ATLAS electromagnetic calorimeter. The signal is shaped and sampled with 40 MHz frequency, corresponding to a sample period of 25 ns, and a total sampling window of 800 ns (during normal data-taking only 5 samples (125 ns) are read out). The study of the pulses measured with 32-sample readout allows one to determine the drift time in the liquid argon gaps related to the undershoot of the pulse, and the electrode position related to the rise at the end of the pulse. The curve shows the expectation agreeing to better than 2% with the measurement.

A full barrel slice, from the innermost tracking detectors and magnetic field to the outermost muon spectrometer, was exposed to the particle beams. The experimental setup was kept as close as technically possible to the ATLAS geometry. The distance between subdetectors, the pointing geometry, and the magnetic field orientation were preserved where permitted. The most important goals of this test beam campaign were: (i) test the detector performance with final or close to final electronics equipment, data acquisition and trigger infrastructure and reconstruction software, (ii) validate the description of the data by Monte Carlo simulations down to energies of 1 GeV to prepare the simulation of the ATLAS data, and (iii) perform combined studies in a setup very close to that of ATLAS (e.g., combined electromagnetic and hadronic calorimetry, and combined tracking and calorimetry).

### 5.1 Energy reconstruction in the ATLAS liquid-argon electromagnetic calorimeter

The ionisation signal generated in the ATLAS electromagnetic calorimeter is collected from the readout electrodes and brought via cables to the front-end electronics where it is amplified, shaped and sampled at a 40 MHz frequency. The samples (usually five) are stored in an analog pipeline until the arrival of a trigger accept decision. The samples belonging to the accepted event are then digitised and transmitted by the calorimeter backend electronics to readout driver modules, where the signal amplitude is reconstructed and converted to MeV. Figure 7 shows a fully digitised pulse shape with 32 samples from a cosmic-ray event with an unusually large energy deposit. The full cell-energy reconstruction from the digitised pulse samples is encoded in the following conversion formula

$$E_{\text{cell}} = F_{\mu\text{A} \rightarrow \text{MeV}} \cdot F_{\text{DAC} \rightarrow \mu\text{A}} \cdot \left( \frac{M_{\text{phys}}}{M_{\text{calib}}} \right)^{-1} \cdot R \left( \sum_{i=1}^{N_{\text{samples}}} a_i (s_i - p) \right), \quad (3)$$

where the subscripts specify the conversion type. The sum over the digitised samples on the right-hand side is computed from the measured ADC counts, corrected for an overall pedestal ( $p$ ), obtained in regular calibration runs — together with noise and autocorrelation terms — from random triggers in physics

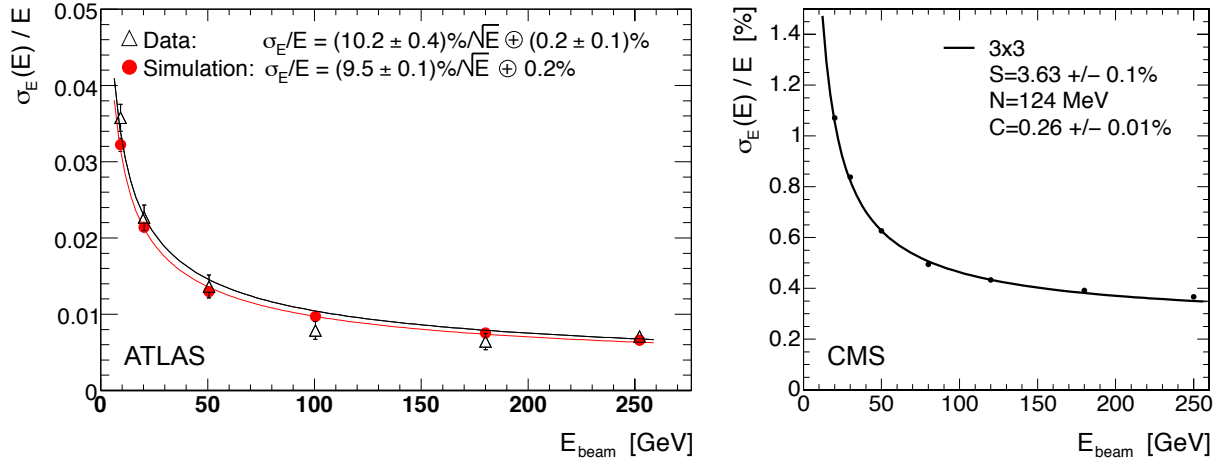


**Fig. 8:** Fractional electromagnetic energy resolution versus the incident energy obtained from electron test beams. Left: result for the ATLAS liquid-argon calorimeter obtained, behind  $1.6X_0$  material thickness, from the H8 combined test beam in 2004. Right: result for the CMS crystal calorimeter obtained without upstream material for 9 out of 36 tested supermodules at the H4 test beam in 2006. The energy was measured in an array of  $3 \times 3$  crystals with electrons impacting the central crystal.

events, and multiplied by the sample-specific ‘optimal filtering coefficients’  $a_i$ , obtained from so-called ‘delay’ runs where calibration signals are injected to measure the pulse shape. The sum is taken as an argument to the ADC-to-DAC ramp function  $R$ , obtained from dedicated electronics calibration runs, where known charges are injected and the corresponding ADC output is measured and fit to a linear function. Differences between the calibration and physics pulse shapes are corrected via the  $M$  ratio. The DAC values are then converted to  $\mu\text{A}$ , which is related to the calibration injection resistance and computed taking into account cable and other attenuation effects. Finally, the  $\mu\text{A}$  signal is converted to MeV by applying the corresponding current-to-energy conversion factor, and by correcting the energy lost in the absorber material (sampling fraction). Once the cell energies are reconstructed, cells are summed to form a cluster over all three longitudinal compartments and the presampler of the electromagnetic calorimeter.

This procedure provides the electromagnetic energy scale. Physics events such as  $Z \rightarrow ee$  will be used to achieve absolute energy calibration. For hadrons and jets, one needs to account for hadronic shower corrections, that is, one must pass from the electromagnetic to the hadronic energy scale.

## 5.2 Electromagnetic energy resolution

The resolution of an electromagnetic calorimeter is driven by the amount of active material in which the electromagnetic shower develops, and by the shower containment. Containment requires a calorimeter thickness of many radiation lengths  $X/X_0 > 20$ , where the radiation length  $X_0$  is a material characteristic related to the energy loss of high-energy particles interacting electromagnetically with the material.<sup>15</sup> Test beams with known particle content and energy allow the experiments to measure resolution, linearity and uniformity of the calorimeter energy response. The resolution results obtained by ATLAS and CMS for electron beams with different energies are shown in Fig. 8 (the measurements were obtained under different experimental conditions, see figure caption). Calorimeter resolution is conveniently expressed as a function of the incident electron/photon energy,  $E$ , by the expression

<sup>15</sup>The radiation length is both the mean distance over which a high-energy electron loses all but  $1/e$  of its energy by bremsstrahlung, and  $7/9$  of the mean free path for pair production by a high-energy photon.



$$\frac{\sigma(E)}{E} = \frac{S}{\sqrt{E} \text{ (GeV)}} \oplus C \oplus \frac{N}{E \text{ (GeV)}}, \quad (4)$$

where the first term on the right-hand side determines the *stochastic* resolution resulting from statistical fluctuations in the number of shower particles<sup>16</sup> and in the shower containment, the second *constant* term is due to non-uniformities in the calorimeter response introduced by inhomogeneities and non-linearities, and the third *noise* term quantifies electronics noise and in-time physics pile-up. The ‘ $\oplus$ ’ indicates that the different resolution terms are added in quadrature. Some numbers obtained for these terms from fits to electron test beam data are quoted on the plots in Fig. 8. Taking into account the full detectors and materials, one expects for ATLAS (CMS) the following benchmark resolution parameters:  $S = 10\text{--}12\%$  ( $3\text{--}5.5\%$ ),  $C = 0.2\text{--}0.35\%$  ( $0.5\%$ ),  $N = 250 \text{ MeV}$  ( $200\text{--}600 \text{ MeV}$ ), where the better (worse) numbers refer to the barrel (endcaps).<sup>17</sup> With the 9 out of 36 super-modules calibrated in the 2006 test beam, CMS also found excellent energy-response uniformity of 0.27%.

### 5.3 Hadronic energy resolution

During the ATLAS H8 combined test beam campaign, pion beams with 6 discrete energies ranging from 10 GeV to 350 GeV were used to study the hadronic energy reconstruction in the calorimeters. Hadron showers originate from interactions of hadrons with nuclei. The density of hadron calorimeters is therefore appropriately expressed in terms of the nuclear interaction length  $\lambda$ , which quantifies the mean free path of hadrons in material between strong collisions. For example, silicon has  $\lambda = 45.5 \text{ cm}$ , iron 16.8 cm, lead 17.1 cm, and water 83.6 cm, to be compared to  $X_0 = 0.56 \text{ cm}$  for lead and 1.76 cm for iron. Hence  $\lambda \gg X_0$  and one can separate electromagnetic showers, which are short-ranged, from far-ranged hadronic showers, which also clarifies why calorimeters are called and arranged as they are: electromagnetic calorimeters fully absorb electromagnetic showers, but only parts of the showers initiated by hadrons; the following calorimeter layers (usually sampling calorimeters) entirely absorb the hadronic showers.

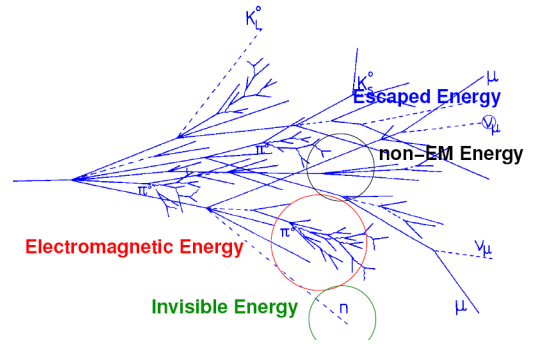


**Fig. 9:** Simulated hadron shower consisting of electromagnetic and non-electromagnetic, invisible and escaped energy.

Hadronic showers (Fig. 9) consist of approximately 50% electromagnetic energy (e.g.,  $\pi^0 \rightarrow \gamma\gamma$ ), 25% non-electromagnetic energy (such as  $dE/dx$  from  $\pi^\pm$ ,  $\mu^\pm$ ,  $K^\pm$ ), another 25% invisible energy (nuclear fission and excitation, neutrons), and 2% escaped energy (e.g. neutrinos). Invisible and escaped

<sup>16</sup>The number of particles produced in the shower is proportional to the energy of the incident particle:  $N_{\text{part}} \propto E$ . The error in the energy measurement is due to statistical fluctuations in  $N_{\text{part}}$ , i.e.,  $\sigma(E) \propto \sqrt{N_{\text{part}}}$ . One thus finds for the stochastic contribution to the energy resolution  $\sigma(E)/E \propto 1/\sqrt{E}$ . Because in sampling calorimeters the absorber material does not contribute to the energy measurement, the electromagnetic energy resolution is worse than for crystal calorimeters, provided that the crystals have sufficiently large  $X/X_0$  so that the full shower can be contained. This is the case for the  $\text{PbWO}_4$  scintillating crystals used by CMS, which have very high density so that the total calorimeter has  $28X_0$  (for comparison, the ATLAS calorimeter has  $22X_0$ ). The sampling fractions in the ATLAS electromagnetic calorimeter are  $f_{\text{sampl}} = 0.17$  ( $0.20$ ) for  $|\eta| \leq 0.8$  ( $|\eta| > 0.8$ ). The measured energy must thus be corrected for the dead material  $E_{\text{true}} = f_{\text{sampl}}^{-1} E_{\text{meas}}$ , so that the stochastic resolution becomes  $\sigma(E)/E \propto \sqrt{d_{\text{sampl}}/f_{\text{sampl}}}/\sqrt{E} \approx 3/\sqrt{E}$ , where  $d_{\text{sampl}}$  is the thickness of the sampling layers (finer sampling provides better resolution). Hence the approximately three times worse intrinsic electromagnetic energy resolution in ATLAS compared to CMS.

<sup>17</sup> With these parameters, a back-of-the-envelope calculation for  $H \rightarrow \gamma\gamma$  gives for the di-photon mass resolution as a function of the photon energy:  $\sigma(M_{\gamma\gamma})|_{E_\gamma} \propto M_H \sigma(E_\gamma)/(\sqrt{2}E_\gamma) \approx 1.2 \text{ GeV}$  ( $0.7 \text{ GeV}$ ), for ATLAS (CMS) and where  $M_H = 120 \text{ GeV}$  has been assumed. To obtain a realistic estimate of the resolution one must also include the error on the opening angle (photon directions), as well as  $\gamma \rightarrow e^+e^-$  conversions (20–60% of all photons from  $H \rightarrow \gamma\gamma$  decays, strongly increasing for large  $|\eta|$ ). Both effects reduce the effective resolution difference between the experiments.



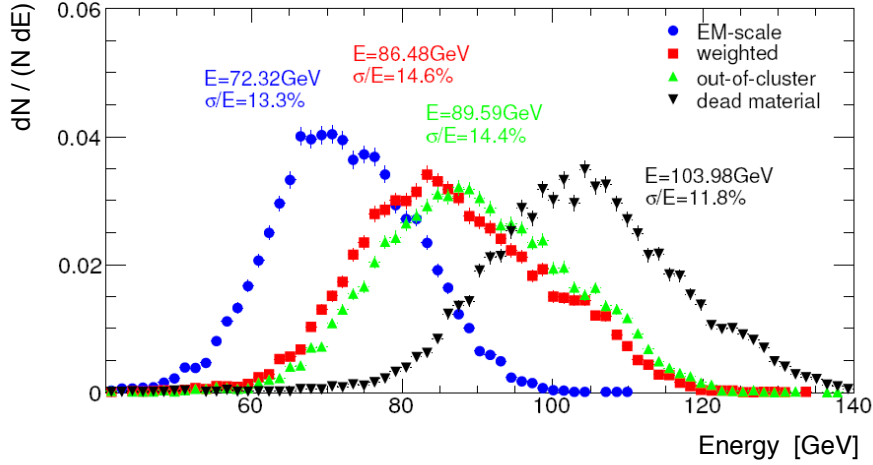


**Fig. 10:** Reconstructed energy for 100 GeV test beam pions in a slice of the ATLAS barrel electromagnetic and hadronic calorimeters. Shown are: raw measured energy (circles), after reweighting from the electromagnetic to the hadronic scale (squares), after applying out-of-cluster corrections from shower leakage (top-oriented triangles), and after dead-material corrections (bottom-oriented triangles).

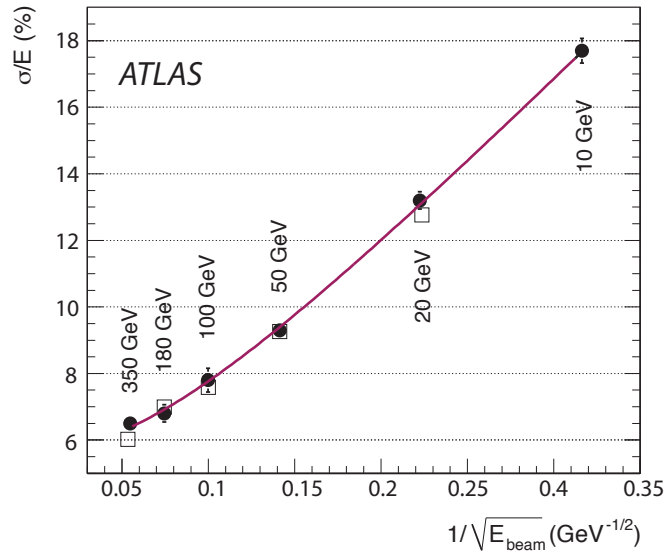


**Fig. 11:** Fractional energy resolution for pions at 0.35 pseudorapidity (equivalent calorimeter depth  $7.9\lambda$ ), versus the incident energy from test beam data in the ATLAS hadronic calorimeter (full circles), and compared to Monte Carlo simulation (open squares).

energy causes worse resolution for hadronic showers than for electromagnetic ones. When uncorrected it also causes an underestimate in the measured energy with respect to the true hadron energy. Figure 10 shows the reconstructed energy in the ATLAS barrel calorimeter slice for 100 GeV pions from test beams. The raw measured energy at the electromagnetic scale undershoots by 28% with the largest contributions to the bias coming from invisible and escaped energy, and from dead material. While the various corrections recover the overall energy scale, they cannot improve the resolution (unless event-by-event corrections as a function of the longitudinal and transverse shower shapes are applied).

The final energy resolution obtained from pion test beam data for the ATLAS calorimeter is shown in Fig. 11, and compared to the expectation from Monte Carlo simulation (Geant-4). One finds benchmark values for single hadrons of 53%, 3%, and 0.5 GeV, for the stochastic, constant and

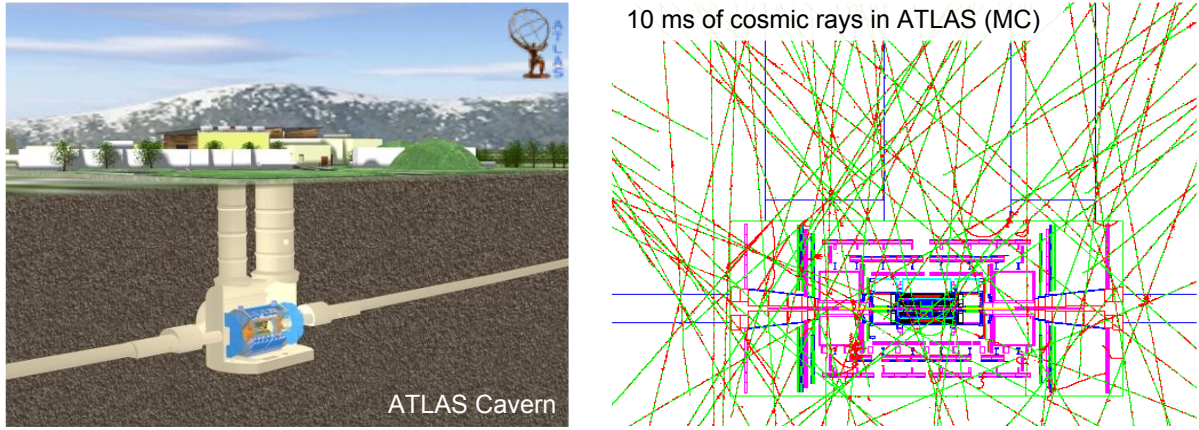


**Fig. 12:** Schematic drawings of the ATLAS underground cavern with supply shafts (left — two lateral elevator shafts are not drawn), and simulated cosmic rays through ATLAS within 10 ms exposure time (right).

noise terms, respectively (*cf.* Eq. 4). For comparison, for central jets Monte Carlo simulation predicts 60%, 3%, and 0.5 GeV for the resolution parameters, and a missing transverse energy resolution of  $\sigma(E_T^{\text{miss}})/\sum E_T \approx 55\%$ . These values are somewhat worse in CMS due to the reasons mentioned in Section 3.

## 6 Commissioning with cosmic rays

ATLAS and CMS have performed extensive campaigns of cosmic ray data-taking, initially with the individual systems, later including more and more detector systems with the completion of the installation in the pits. The goals of these studies are — along with exercising the detector operation, and the full data taking, reconstruction and analysis chain — tracking alignment (with and without magnetic field), deriving dead channel maps, measuring the muon trigger and tracking efficiencies, analysing calorimeter pulse shapes, improving the detector timing, tuning Monte Carlo simulation, etc.

Cosmic rays stem from cosmic nuclei (90% protons, i.e., hydrogen nuclei) that interact strongly with the Earth's atmosphere, creating hadrons — mainly pions and kaons with relative intensity 1:0.054 [17], which decay to minimum ionising relativistic muons that reach sea level on Earth,<sup>18</sup> or which undergo nuclear interactions with nuclei in air. The muon flux at the surface is approximately 130 Hz per m<sup>2</sup> for  $E_\mu > 1$  GeV, and the average muon energy is about 4 GeV. The ATLAS detector, being separated from the surface by 100 m of earth and stone, receives a muon flux of approximately 4 kHz in the fiducial volume of the muon spectrometer, and 15 Hz in the TRT barrel (numbers from Monte Carlo simulation). The supply and elevator shafts (see left-hand plot of Fig. 12) provide reduced shielding, which translates into an increased occupancy of the detector elements underneath the shafts or close by

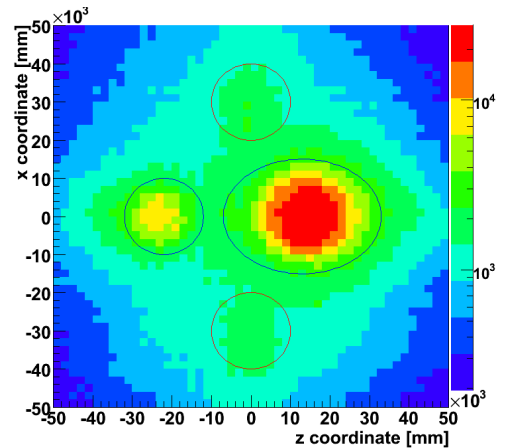


**Fig. 13:** Reconstructed cosmic tracks (6.6 million) in the ATLAS resistive plate chambers, extrapolated to the surface. The ellipses indicate the supply and elevator shafts.

<sup>18</sup>Cosmic rays have been, and are still, sources of major discoveries in particle physics. For example, in 1932, Anderson (Cal Tech, USA) discovered the antielectron (positron) in cosmic rays. Later in 1946, Rochester and Butler (Manchester, England) observed two tracks ‘out of nothing’ in cosmic rays, which were pions from the decay of a neutral (‘strange’) kaon, thereby initiating particle physics. Today, very high energy cosmic rays are extensively studied.

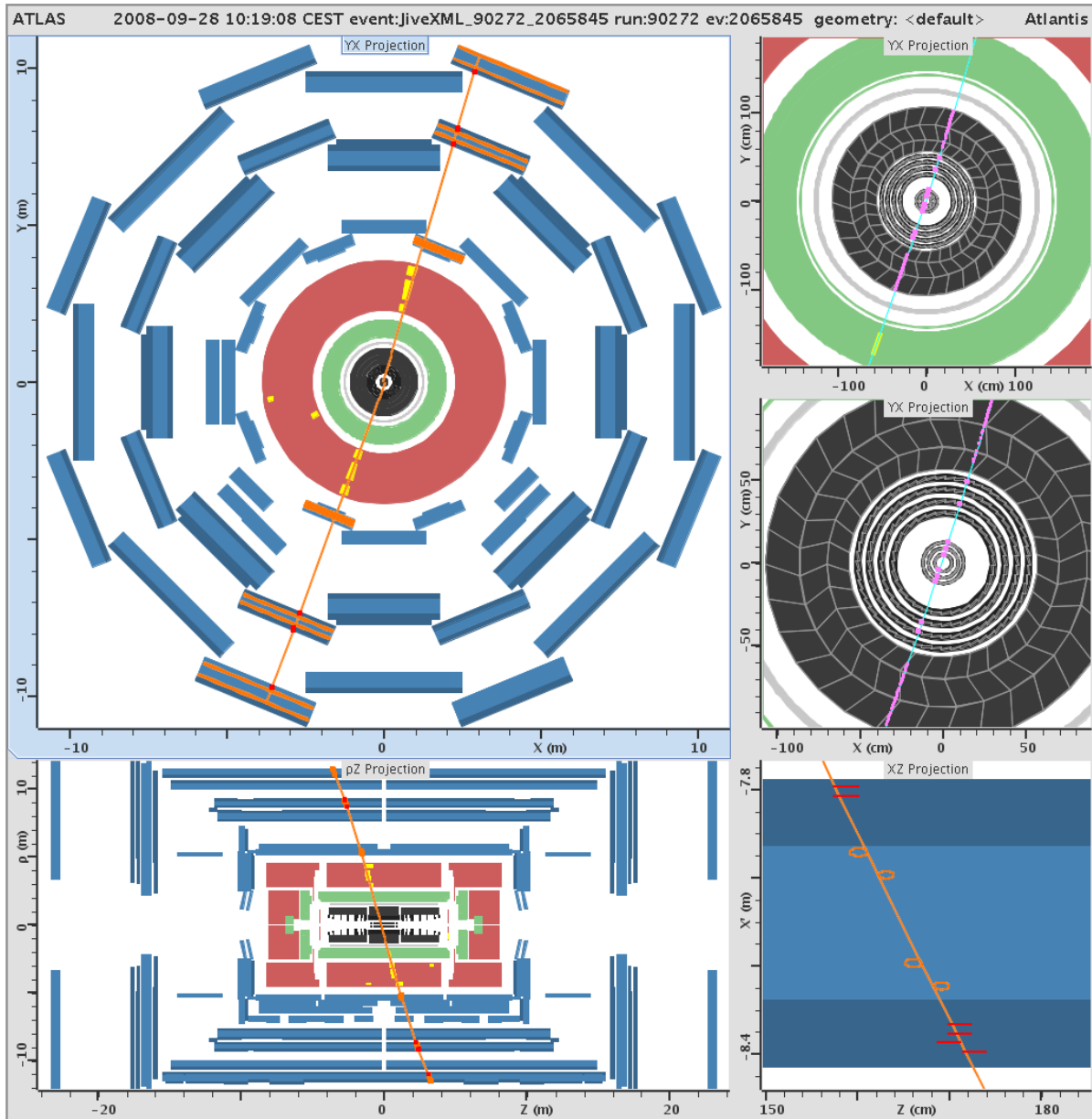


**Fig. 14:** A cosmic ray muon measured by ATLAS. Seen are hits in the muon spectrometer and the inner tracking systems, as well as energy deposits in the hadronic tile calorimeter. All magnets were switched off in this run.

(Fig. 13). The right-hand plot of Fig. 12 shows a simulated 10 ms snapshot of the ATLAS detector bombarded by cosmic rays. High-energy cosmic rays sometimes also produce so-called ‘air showers’ (and *extensive* air showers), where an avalanche of secondary scattering particles is created. Such air showers have been observed by the experiments, giving rise to events with large numbers of muons (order 10 to 100), jets, and large deposited energy (events with 6 jets, all exceeding 20 GeV transverse energy, have been seen).

Figures 14–17 show event displays of cosmic rays in ATLAS and CMS, measured with the full detectors. ATLAS accumulated 580 million combined cosmic ray events between September 13 and October 29, 2008, and in June/July and October/November 2009. CMS recorded 370 million combined events between October 13 and November 11, 2008 during the CRAFT exercise (many more cosmic ray data have been recorded by CMS during other campaigns). All events have been promptly reconstructed

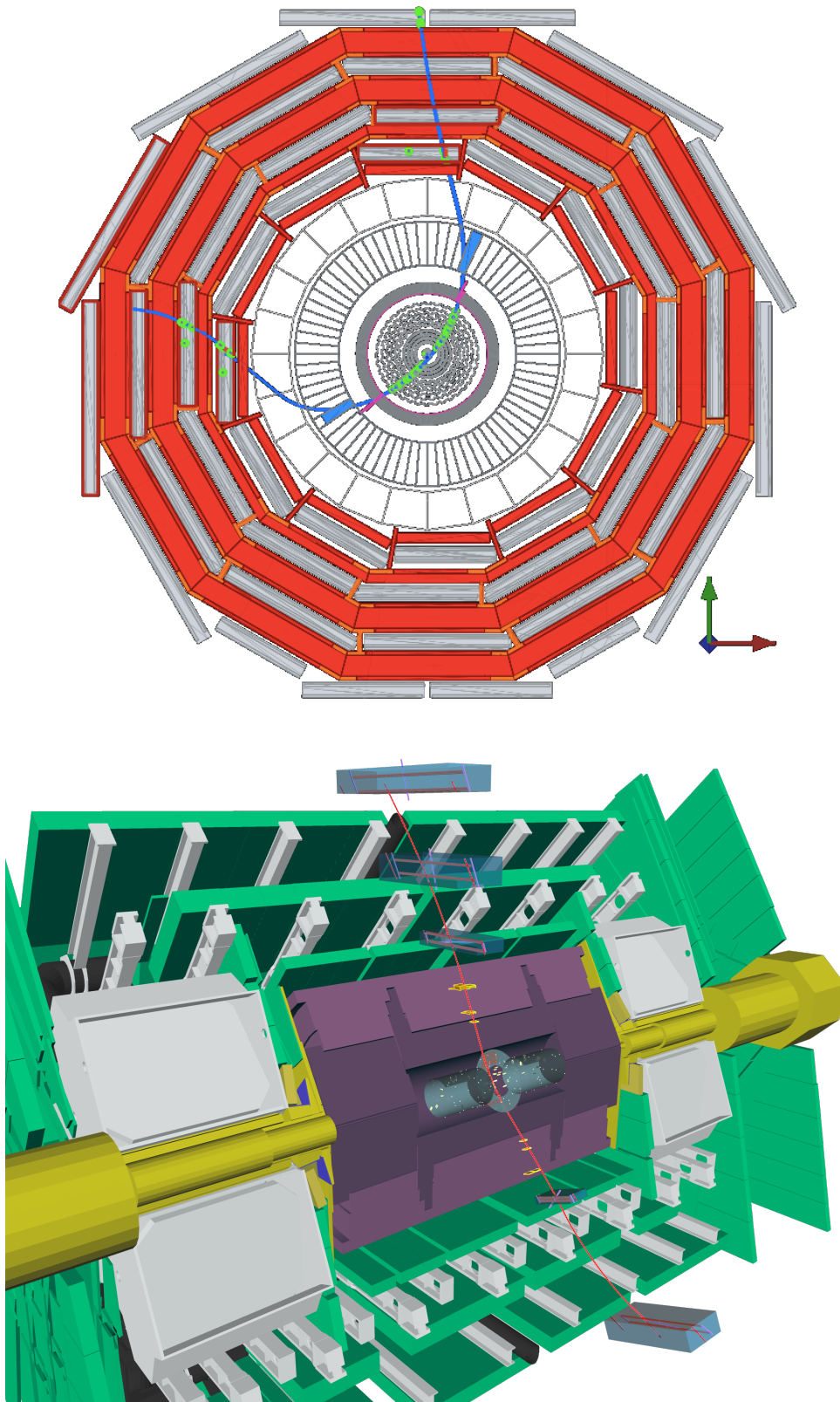


**Fig. 15:** Top: a cosmic ray muon measured by CMS, strongly bent in the transverse plane by the 3.8 T solenoid field. Bottom: three-dimensional view of a cosmic ray muon in ATLAS.



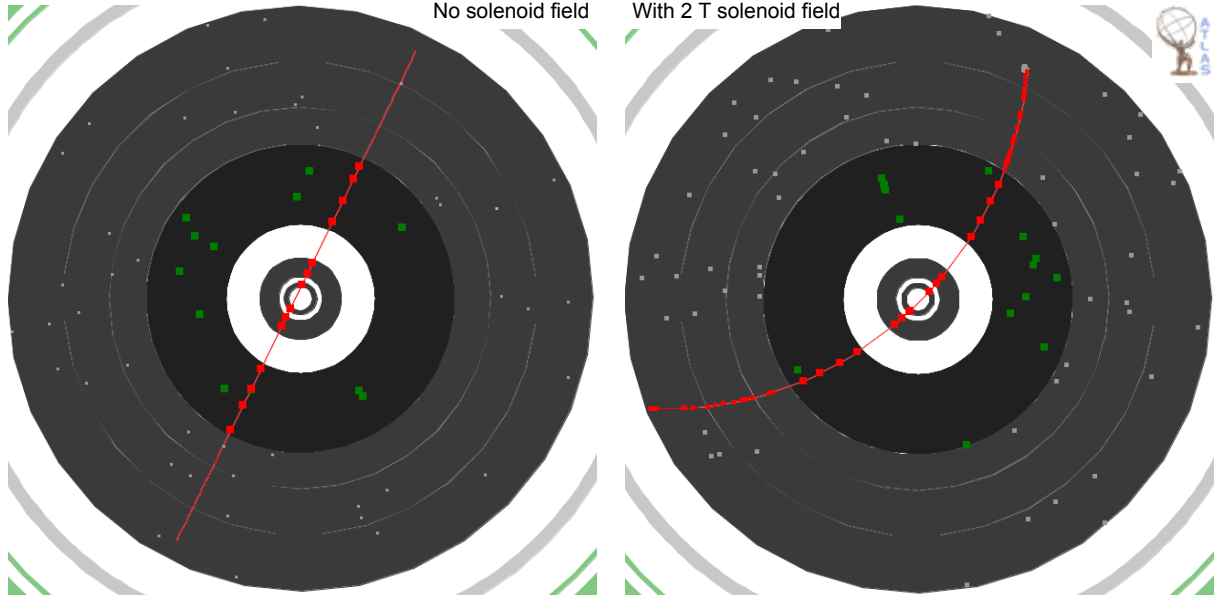


**Fig. 16:** Transverse views of cosmic ray tracks measured in the ATLAS pixel (the three innermost hits depicted by the dots) and silicon strip detectors (four double hits at about half radius in the event displays). The left (right) drawing shows a straight track measured with the solenoid field off (on). The right plot shows also transition radiation tracker hits.

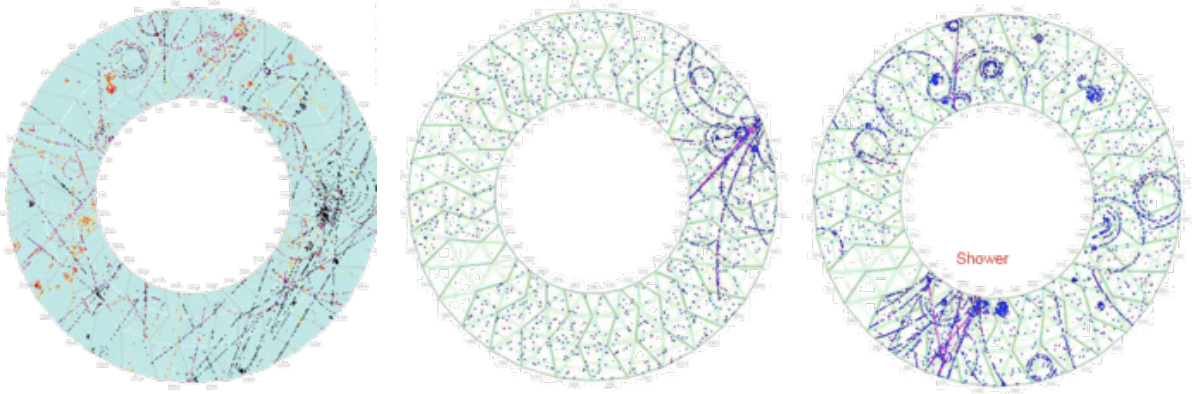


**Fig. 17:** Cosmic ray shower tracks seen in the ATLAS transition radiation tracker.

at the CERN Tier-0 centre, reprocessed after software and conditions upgrades at the Tier-1 worldwide computing centres, and distributed for analysis on the LHC Computing Grid.

### 6.1 Cosmic ray spectra in the inner tracker

Tracks bent in a magnetic field are characterised by five parameters. The parameters are defined with respect to a reference point, the perigee, which is the point of closest approach to the beam axis (along  $z$ ). The impact parameters  $d_0$  and  $z_0$  are the signed distances to the  $z$ -axis and the  $z$ -coordinate of the perigee, respectively. Accordingly, the angles  $\phi_0$  and  $\theta_0$  are defined in the transverse plane and with respect to the  $z$ -axis at the perigee, respectively. The fifth parameter,  $q/p$ , is the charge of the cosmic muon divided by its momentum, defining curvature and orientation of the track helix.

Figure 18 shows the angular and impact parameter distributions of cosmic muon tracks measured in the ATLAS inner tracker. The asymmetries reflect the top-down nature of cosmic tracks, and the shaft

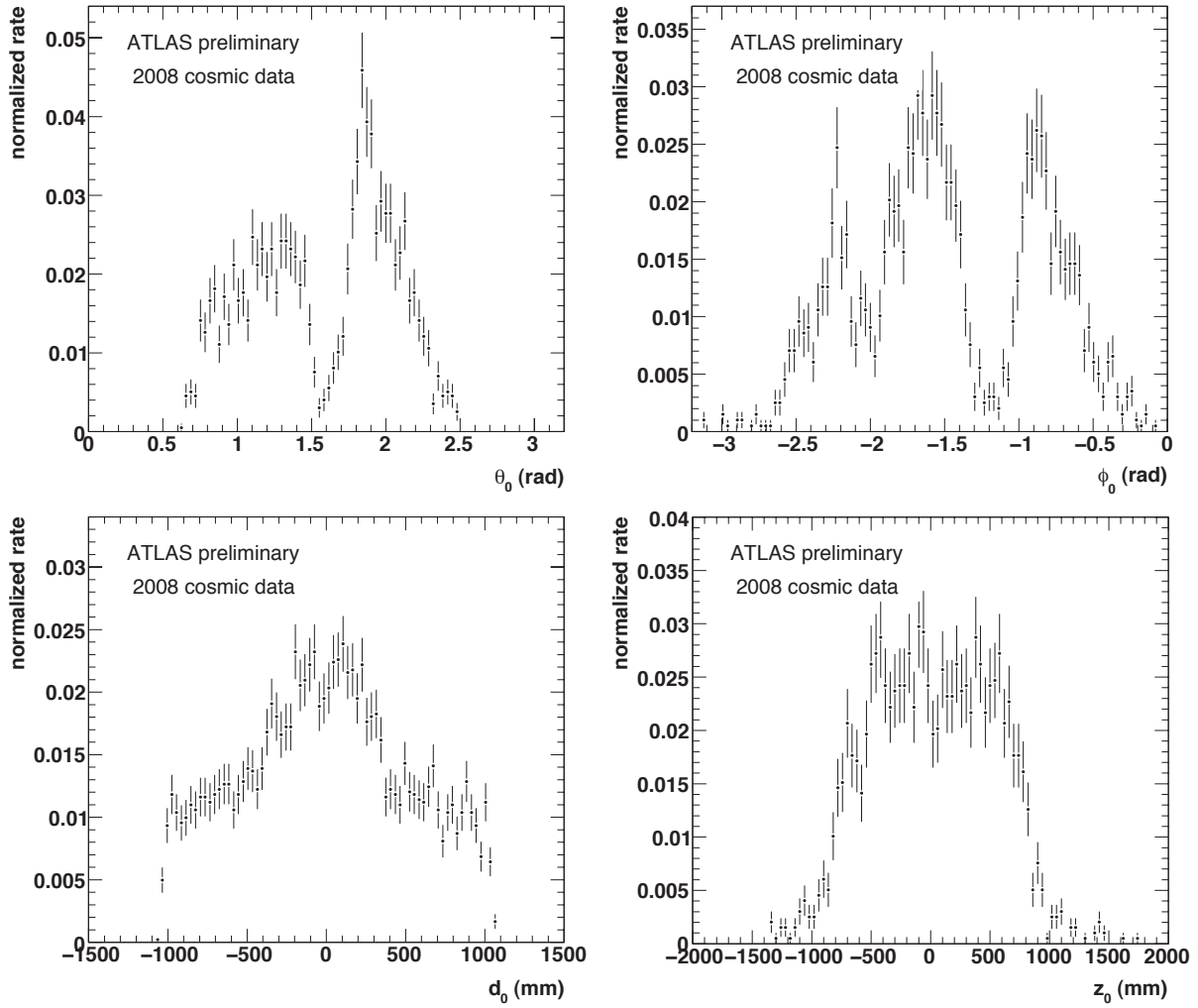


**Fig. 18:** Track parameter distributions of cosmic muon tracks measured in the ATLAS inner tracker. Shown are the polar and azimuthal angles (upper plots) and transverse and longitudinal impact parameters (lower plots). The asymmetries reflect the top-down nature of cosmic tracks, and the shaft architecture of the ATLAS cavern.

architecture of the ATLAS cavern (Fig. 13). For the  $\theta_0$  and  $z_0$  distributions, the tracks are required to have hits in the silicon detectors, because these parameters are not measured by the transition radiation tracker (barrel).

## 6.2 Inner tracker alignment

The high-precision tracking detectors of ATLAS and CMS, and the huge muons systems (especially in ATLAS) challenge the accuracy with which the positions of the active detector elements must be known. And although the detectors have been built and installed with the greatest care, it does not meet the requirements imposed by the detector performance and by physics. Therefore the detectors have to be empirically *aligned*. Alignment signifies measuring the real detector positions and orientations from data, and correcting the reconstruction software accordingly. (It does not mean moving detector parts!). Several methods of varying complexity to solve alignment problems exist, and it is convenient to separate the alignment procedure into alignment levels, such as system, layer, and module, requiring increasing statistics due to an increasing number of degrees of freedom.

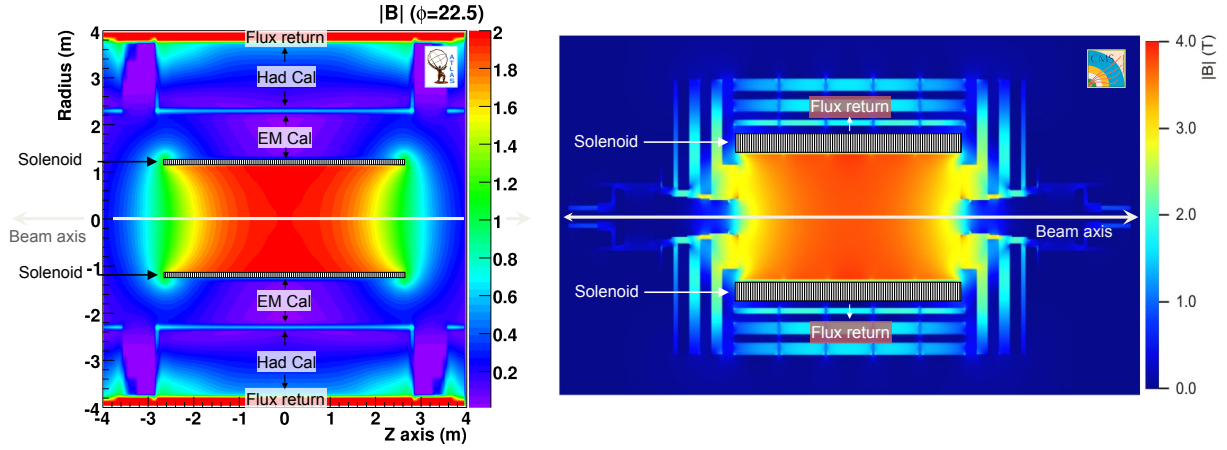


**Fig. 19:** Solenoid fieldmaps for ATLAS (left) and CMS (right). The colour scales are indicated on the vertical axes. Because the CMS solenoid is much longer (axial length of 12.9 m compared to 5.3 m in ATLAS), the inner tracking detectors, with total active lengths of 5.6 m (ATLAS) and 5.4 m (CMS), see a more homogeneous field in CMS than in ATLAS, where the inhomogeneities in the endcaps can reach up to 50% (which are however accurately mapped with magnetic field surveys and properly included in the reconstruction).

### Alignment of the inner tracking systems

The inner tracking systems of ATLAS and CMS (*cf.* Section 3) provide excellent position resolution, with (ATLAS-barrel numbers)  $10\ \mu\text{m}$  ( $r\phi$ ),  $115\ \mu\text{m}$  ( $z$ ) for the Pixel device (total of 1744 modules),  $17\ \mu\text{m}$  ( $r\phi$ ),  $580\ \mu\text{m}$  ( $z$ ) for the silicon strip detector (4088 modules), and  $130\ \mu\text{m}$  ( $r\phi$ ) per straw for the transition radiation tracker (2688 modules). A reasonable challenge is to align all parts of the detectors so that the track degradation due to misalignment not exceed 20% of the intrinsic resolution. The sources of information used for alignment are fourfold: (i) assembly knowledge: construction precision and survey data, for the initial alignment precision, and for corrections and uncertainties; (ii) online monitoring and alignment: lasers and optical cameras, before and during a run; (iii) offline track-based alignment: using physics and track residual information; (iv) offline monitoring: using physics observables, tracks and particle identification parameters.

Before coming to the alignment based on track residuals, let us briefly recall how a track momentum is measured. Charged particles are deflected in the homogeneous<sup>19</sup> axial field (i.e., the field is oriented parallel to the  $z$  coordinate along the beam line) of the solenoid magnet. Since the Lorentz force is perpendicular to the magnetic ( $B$ ) field and to the particle's flight vector, the particle trajectory projected onto the plane perpendicular to the  $B$  field describes a circle with radius  $r[\text{m}] = p_T [\text{GeV}]/(0.3 \cdot B [\text{T}])$ . Thus, for transverse momenta between 10 GeV and 1000 GeV, one finds radii between 17 m (9 m) and 1700 m (895 m), for ATLAS (CMS), which are to be compared with the radius of  $\sim 1$  m of the ATLAS and CMS inner tracking systems. Tracks with transverse momenta smaller than 0.3 GeV (ATLAS) or 0.6 GeV (CMS) become so-called ‘loopers’, which travel a full circle in the inner tracker and do not reach the barrel electromagnetic calorimeter. The  $r$  and  $p_T$  values of a track are derived from the measurement of the track's sagitta ( $s$ ) by  $r \approx L/(8s)$  (if  $s \ll L$ ), where  $L$  is half the length of the transverse distance vector between the two extreme measurement points of the arc in the tracking system, and the sagitta determines the maximum distance between the intersection of the transverse distance vector with the radius vector, and the arc (the sagitta measures the deviation of the arc from a straight line,  $L$ , *cf.* Fig. 26). The smaller the sagitta  $s$  the larger the radius and therefore the momentum of the track and, for constant precision on  $s$ , the larger the relative error on the sagitta determination and hence on  $p_T$ :  $p_T \propto s^{-1}$  and  $\sigma(p_T)/p_T \propto p_T$ .

<sup>19</sup>Not quite, as seen below.

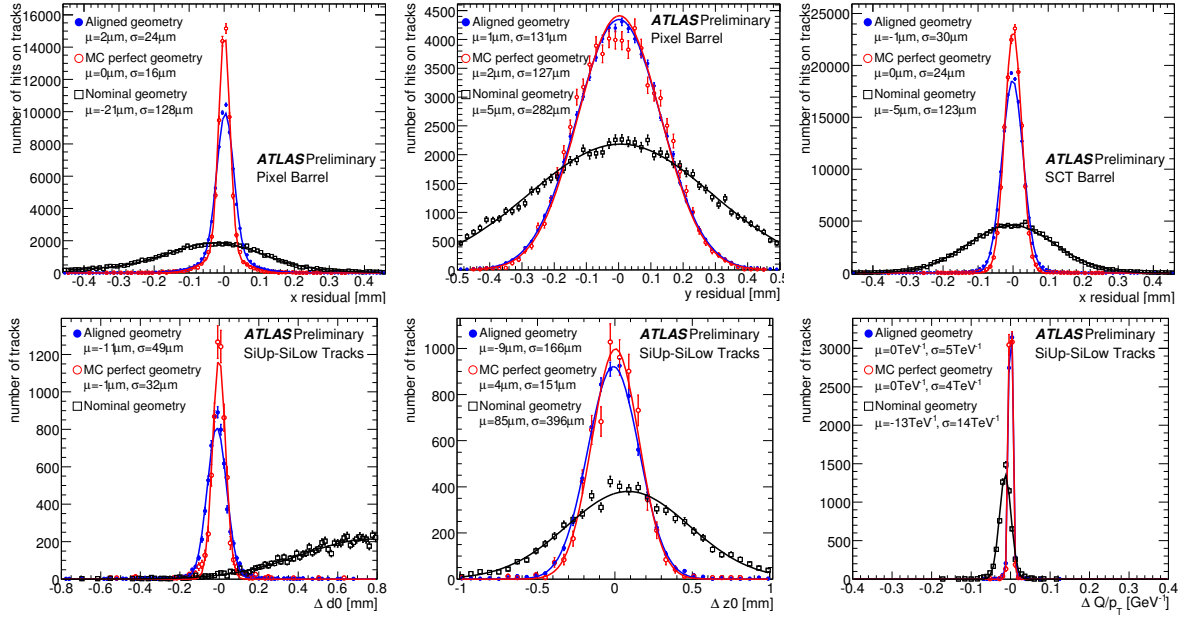


**Fig. 21:** Hit residuals (upper plots) for the ATLAS pixel and silicon strip detectors before alignment (open squares), after alignment with cosmic ray tracks (full circles), and for ideal conditions from Monte Carlo simulation (open circles). The lower plots give the impact parameter resolution for the same three data samples. The resolution is obtained with the track-splitting technique (see text).

Track fitting in the LHC environment is very challenging. It must deal with ambiguities, hit overlaps, multiple scattering, bremsstrahlung, multiple vertices, etc. Track fitters take Gaussian noise (e.g., Kalman filter) and non-Gaussian noise (e.g., Gaussian sum filter) into account. Owing to the large number of tracks per event and because tracks are used for selection in the high-level trigger, the fits must be very fast.

Figure 19 shows the superconducting solenoid field maps for ATLAS and CMS. Inhomogeneities in the magnetic field strengths occur towards the end of the solenoids, which are strongly influenced by the magnetic structure of the nearby detector elements. The  $\sim 2$  T flux return yoke in CMS is used for muon momentum measurement. (The ATLAS return yoke, integrated into the tile hadronic calorimeter and its support structure, also produces a  $\sim 2$  T.m azimuthal track deviation, which is, however, not measured precisely in the muon spectrometer and hence not used for momentum measurement.)

The alignment algorithm minimises the track residuals by fitting detector positions (layers and modules) to measured tracks (Fig. 20). The fit minimises a global estimator, which could be written by  $\chi^2 = \sum_{i \in \text{hits}} (m(\vec{\alpha}) - h_i)^2 / \sigma_i^2$ , where the function  $m$  corresponds to the model prediction (track) at module of hit  $i$ ,  $\vec{\alpha}$  is the vector of track parameters, and  $h_i$  and  $\sigma_i$  are the measured hits and their errors. The full global  $\chi^2$  function must, however, also account for correlations so that it becomes:  $\chi^2 = \sum_{\text{tracks}} (r^T V^{-1} r)$ , where the residuals  $r$  are functions of the track parameters, the alignment parameters and the hit measurements along a track. The  $\chi^2$  function is simultaneously minimised with respect to the track and the alignment parameters.

The smallest movable object in the alignment procedure is a module, which has 6 degrees of

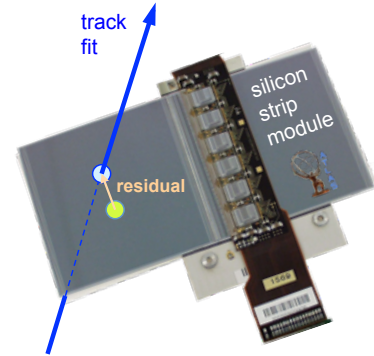


**Fig. 20:** Sketch of a track model through an ATLAS silicon strip tracker module, and a measured close-by hit defining the hit residual.



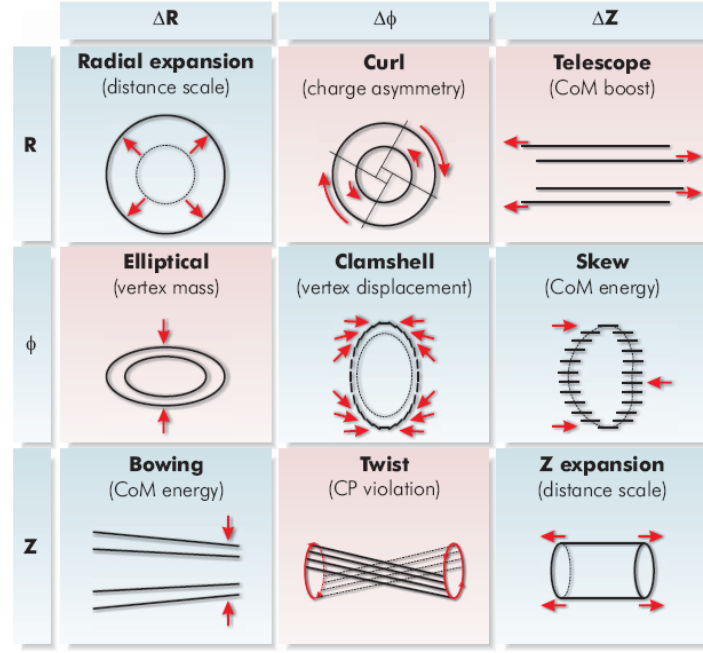


**Fig. 22:** Different types of misalignment according to transverse distortions in  $R$ ,  $\phi$ , and deformations along the beam axis ( $z$ ). The pink types leave the  $\chi^2$  estimator approximately invariant ('weak modes').

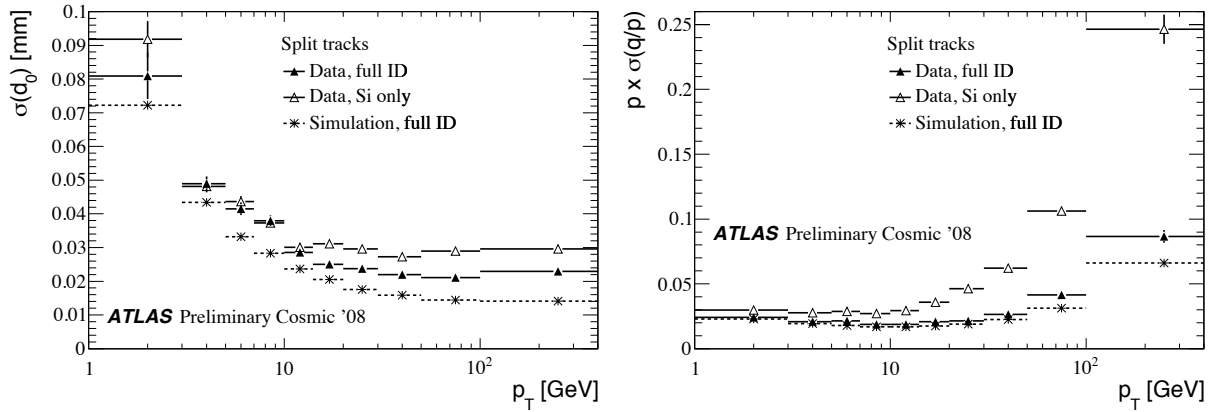
freedom: 3 translation coordinates and 3 rotation angles. Taking into account the total number of modules of ca. 8500 (ATLAS number), one obtains 51 000 degrees of freedom that need to be determined by the fit. Depending on the alignment level (whole barrel/endcap, layers/disks, modules) different techniques can be used, where for either of these the correlations between fit parameters are important ingredients to help the fit converge rapidly. Neglecting correlations may not lead to a wrong fit result, after full convergence, but it is less efficient.

Figure 21 shows residual distributions for the ATLAS pixel and silicon strip detectors, as well as impact parameter and  $Q/p_T$  distributions, before and after alignment with cosmic ray tracks. The widths of these distributions are convolutions of the intrinsic hit and tracking resolution (seen under ideal conditions), and misalignment effects. The impact parameter and transverse momentum resolutions are obtained by splitting a cosmic ray muon track traversing the full detector into two tracks that are re-fit independently and compared.<sup>20</sup> A total of 4.9 (2.7) million tracks with solenoid field on (off) have been used by ATLAS (similar numbers of tracks are used by CMS for alignment), of which 1.2 million (230 thousand) have silicon strip (pixel) track components so that they can be used to align these detectors. Alignment results close to ideal have been obtained.

### Weak modes

Unfortunately, the minimisation of hit residuals does not guarantee that indeed the true positions of the detector elements have been determined. This is because the residuals, and hence the  $\chi^2$  estimator, are insensitive against some types of misalignment, which may nevertheless impact the physics performance. Examples for such 'weak modes' are elliptical skews, i.e., distortions of the type  $\delta\phi = \lambda + \beta/R$  or  $\delta z \approx R$ . Figure 22 summarises the various types of misalignment. The pink-coloured types represent weak modes in the global residual-based  $\chi^2$  estimator. Weak modes contribute to the lowest part of the eigenspectrum. Their deformations bias physics measurements and lead to systematic effects. The understanding of these effects is thus of utmost importance. Weak modes can be constrained by adding

<sup>20</sup>The resolution is the RMS of the difference divided by  $\sqrt{2}$ .



**Fig. 23:** Transverse impact parameter resolution (left) and relative momentum resolution (right) versus the transverse momentum for the ATLAS inner tracker. The full (open) triangles give the results for all inner tracker detectors combined (only silicon pixel and strip detectors), and the asterisk is the expectation from Monte Carlo simulation with ideal alignment conditions.

more information to the fit, such as: (i) cosmic ray and beam halo tracks (off-beam axis) in addition to beam collision data; (ii) vertex and beam-spot constraints; (iii) resonance masses ( $Z$ ,  $J/\psi$ ,  $Y$ ,  $K_S$ , ...); (iv)  $E/p$  measurements for electrons; and (v) survey data and mechanical constraints.

### 6.3 Inner tracker resolution

The tracking resolution for cosmic ray muons in the inner tracker is studied by comparing track parameters at the perigees using the track-splitting technique. Because both tracks emerging from the splitting have errors, the quoted resolution is the RMS of the residual distribution of a track parameter divided by  $\sqrt{2}$ . Well reconstructed tracks are selected for these studies. ATLAS requires a minimum number of hits in Pixel, silicon strip detector and transition radiation tracker of 2, 6 and 25, respectively, and  $|d_0| < 40$  mm and  $p_T > 1$  GeV, and good timing properties. The left-hand plot of Fig. 23 shows the transverse impact parameter resolution versus the transverse momentum for the ATLAS inner tracker. In the low  $p_T$  region, the resolution is dominated by multiple scattering. At higher momenta, the resolution becomes independent of the momentum as is expected for almost straight tracks. Including the transition radiation tracker information improves the resolution due to the extended lever arm. The difference between data and the Monte Carlo prediction is a measure of the remaining misalignment. The right-hand plot of shows the relative momentum resolution versus  $p_T$ . At intermediate momentum, reduced multiple scattering counterbalances the  $p_T$ -dependent rise of the error due to a decreasing relative accuracy of the sagitta measurement. This latter effect dominates at higher momentum. Again, the difference with respect to the Monte Carlo expectation stems from residual misalignment.

### 6.4 Muon spectrometer alignment

The huge active volumes of the ATLAS and CMS muon spectrometers require a detailed understanding of the inhomogeneous magnetic fields (especially for ATLAS and the CMS endcaps) and the chamber positions to achieve design performance. To derive quantitative requirements, let us briefly recall how the muon precision measurements are obtained. Both experiments use drift tubes, which are standalone coaxial cylindrical drift chambers functioning similarly to proportional tubes, in the barrel (ATLAS also in the outer endcaps for  $|\eta| < 2.0$ ), and cathode strip chambers in the forward direction.

The drift tubes in ATLAS (denoted ‘monitored drift tubes’ — MDT) are made of thin aluminium tubes with 3 cm diameter (4 cm in CMS, 4 mm for the ATLAS transition radiation tracker), filled with a 93% argon and 7%  $\text{CO}_2$  gas mixture at 3 bar pressure (Fig. 24). A  $50\ \mu\text{m}$  gold-plated tungsten wire in

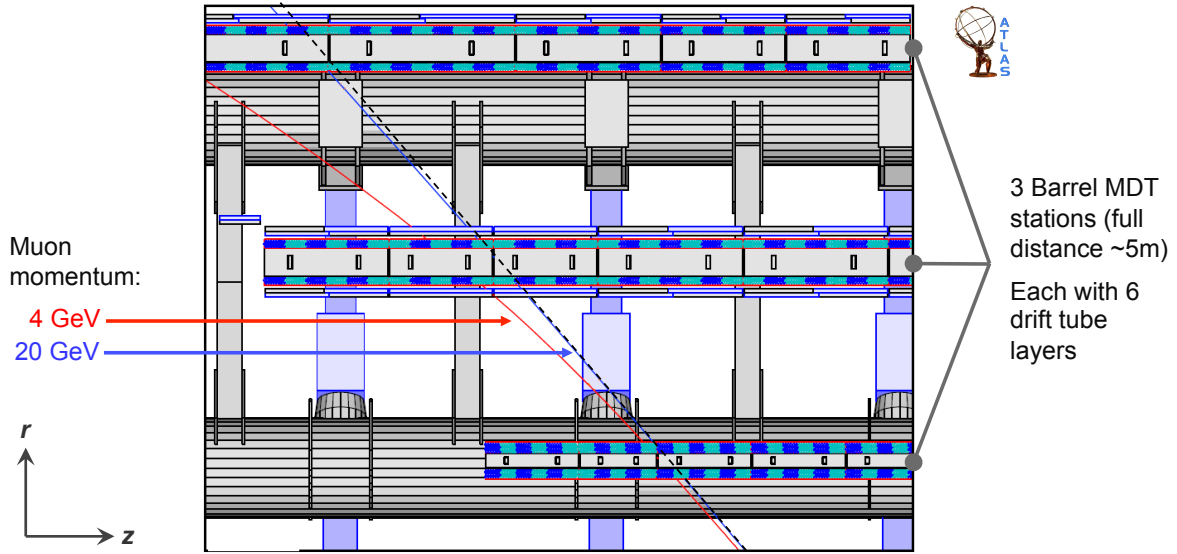


**Fig. 25:** Drawing of ATLAS barrel monitored drift tube stations. There are three of these spanning a full radial distance of  $\sim 5$  m. Shown by the curved lines are simulated muon tracks with 4 GeV (red) and 20 GeV (blue), bent in the  $z$  direction by the toroidal magnetic fields. The curvature is hardly visible for the latter track (see straight dashed line for comparison). The MDT system is designed to measure 1 TeV tracks with 10% relative accuracy, requiring a position alignment of better than  $40 \mu\text{m}$ .

the centre of each tube serves as anode with an applied potential of 3080 V. A charged track traversing the tube ionises the gas and the ionised electrons drift in the electrical field to the wire, while the ions drift to the cathode (cylinder). From the measured hit time of the induced electrical pulse, and the known drift velocity ('space-drift time ( $r-t$ ) relation'), it is possible to determine a *drift circle* around the anode wire, tangential to which the track has passed.

The measurement of several adjacent layers of tubes provides the redundant information required for a full track fit. The measured drift time in a tube reaches up to 800 ns corresponding to a drift velocity of approximately 18 km/s. The average position resolution is  $80 \mu\text{m}$  per tube ( $250 \mu\text{m}$  in CMS), but varies strongly along the drift radius: tracks very far from the anode wire are measured with better precision than close tracks, due to the smaller dispersion in the drift time of the incoming electrons.

The ATLAS drift tubes are arranged in large-sized MDT chambers with six tube layers oriented along  $\phi$  to allow for a precise measurement of the  $z$  coordinate, the direction of which the charged particles are bent in the toroidal magnetic fields. Three almost equally spaced stations of MDT chambers (inner, middle and outer) are installed in the barrel with about 2.5 m radial distance from each other (Fig. 25). A 1 TeV track has a sagitta of about  $s = 500 \mu\text{m}$  at  $\eta = 0$  (cf. sketch in Fig. 26). A measurement of that sagitta with 10% accuracy requires the error induced by misalignment to be significantly smaller than  $50 \mu\text{m}$ . With  $\sigma(s) \approx \sqrt{3/2} \cdot \sigma(z)$ , one finds  $\sigma_{\text{misalign}}(z) \ll 40 \mu\text{m}$ , which represents a tremendous alignment challenge given the size of the system.

Figure 27 shows an example of a misaligned MDT chamber in ATLAS (from simulation). In the

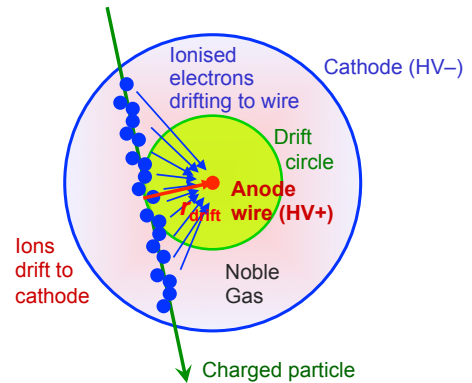


**Fig. 24:** Principle of a drift tube used for precision measurement in the ATLAS and CMS muon systems, and also in the ATLAS transition radiation tracker.

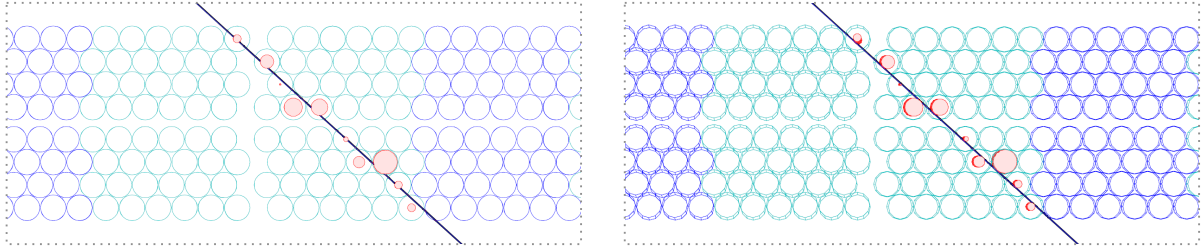


**Fig. 27:** Example of a misaligned drift tube chamber in the ATLAS barrel muon spectrometer (simulation). In the left-hand picture, without alignment corrections, it is not possible to draw a straight line track through the drift circles. After alignment (right-hand picture) the chambers have been slightly tilted so that a good track fit can be obtained.

left drawing, where no alignment corrections have been applied, the track is not tangential to all drift circles. The  $\chi^2$  of the track fit is bad. In the right drawing the chambers have been aligned leading to a good track fit.

### *Optical muon chamber alignment in ATLAS*

ATLAS implements a twofold alignment strategy for the muon system: fits to measured tracks from cosmic rays and collision events, in particular using straight tracks without the toroid fields, provide the absolute MDT chamber positions.<sup>21</sup> Relative chamber movements due to temperature-dependent ‘breathing’ and when switching on the toroid magnets, are monitored by means of an optical alignment system, designed to detect slow chamber displacements, occurring at a timescale of hours or more. The system is based on optical and temperature sensors, and on alignment bars, which are up to 9.6 m long instrumented aluminium tubes used as precision reference rulers. The information from the optical system together with the track-based alignment is used in the offline track reconstruction to correct for the MDT chamber misalignment. Similar to ATLAS, CMS is instrumented with a precise and complex opto-mechanical alignment system that provides a common reference frame between tracker and muon detection systems by means of a net of laser beams. We discuss in the following the ATLAS system.

To first order, only the relative alignment of triplets of chambers traversed by the same muon track is important for a precise sagitta measurement. The barrel optical alignment system thus uses 3-point straightness monitors, which are installed on the inner, middle and outer chambers to form projective lines pointing to the interaction region.<sup>22</sup> The straightness monitor creates a highly redundant image of a coded mask (for example a chess-like pattern) through a lens onto a charged-coupled device (CCD) acting as screen. The mask is lit by infrared LEDs passed through a diffuser to minimise effects of imperfections in the light source. The relative position in transverse direction to the projective lines is measured along the line mask, the

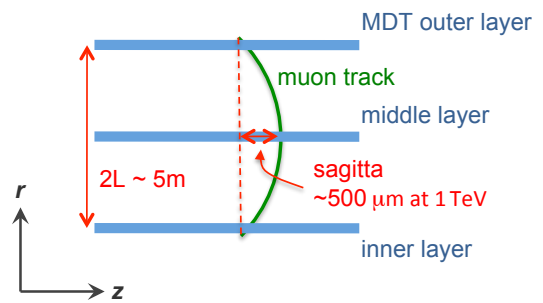


**Fig. 26:** Sketch for the muon sagitta measurement in ATLAS. For a 1 TeV track the sagitta measures about  $500 \mu\text{m}$ .

<sup>21</sup>Full alignment not only requires a proper positioning of the chambers and tubes in the chambers, but one must also correct for the wire sag in the drift tubes, which has been measured from survey data for a fraction of the tubes, and must be derived from track fits for the remaining ones. The wire-sag induced error in the position measurement amounts to  $20\text{--}30 \mu\text{m}$ , depending on the size of the MDT chamber.

<sup>22</sup>In the endcaps, projective lines cannot be installed because the cryostats of the endcap toroid magnets block the way to the interaction region. The optical alignment system thus relies on high-precision reference rulers and alignment bars forming an alignment grid.

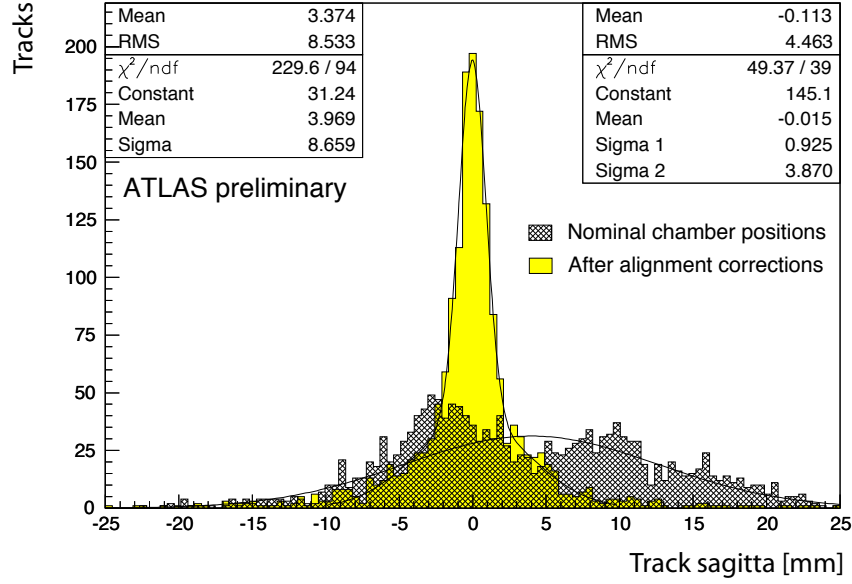


**Fig. 28:** Track ‘sagitta’ for straight cosmic ray muon tracks (toroid fields off) in the ATLAS endcaps before (dark shaded) and after (light shaded/yellow) applying the optical alignment. The sagitta is calculated from the distance in the precision coordinate of the middle chamber segment from the line joining the inner and outer endcap segments. After alignment, the resolution (width) is dominated by multiple scattering effects.

optical centre of the lens, and the CCD camera. It is also possible to measure the (relative) rotation of the mask or the sensor, and the relative rotation around any axis of the mask with respect to the CCD camera. Finally, by computing the actual image size and comparing it with the known mask size (magnification), the position of the lens along the longitudinal axis can be obtained. A total of 6000 (7000) optical lines have been installed in the ATLAS barrel (endcap). Not all of these are projective. In the barrel, praxial lines align adjacent chambers in each layer. In the endcaps there are bars, polar and proximity lines.

The absolute resolution of the optical alignment system is of the order of 300–500  $\mu\text{m}$ , which is insufficient for precision measurements. Hence the necessity to rely on track measurements for absolute chamber positions. The relative optical alignment accuracy has been evaluated with simulated muon shifts of the H8 test beam arrangement and found to correct misalignment within 14  $\mu\text{m}$  error (RMS) on the sagitta, which is well within the specified requirement [18]. Figure 28 shows the distribution of sagitta values for straight cosmic muon tracks (the toroid magnets were turned off so the expected sagitta is zero) in the ATLAS endcaps before and after applying the optical alignment. The sagitta is computed from the distance in the precision coordinate of the middle chamber segment from the line joining the inner and outer chamber segments. The resolution found is compatible with the expectation. The tails in the sagitta distribution after alignment originate from *multiple scattering*.

**Digression.** Multiple scattering denotes the deflection by (or convolution of) successive small-angle scatters of a charged particle traversing a medium. The multiple scattering cross section, dominated by Coulomb scattering from nuclei, is proportional to  $\sqrt{\text{pathlength}/X_0} \cdot p^{-1}$ , i.e., it is enhanced for soft particles and dense matter. The angular distribution is approximately Gaussian at small angles (owing to the central limit theorem), but also large-angle Rutherford scattering occurs with a differential cross section  $\propto \sin^4(\theta/2)$ . Multiple scattering is analogous to diffusion. Figure 29 shows the effect of light diffusion on a wet windscreen. The more matter in terms of radiation lengths a particle traverses in the tracking volume, the more the detector ‘sees’ the particle as we see other cars at night in rainy weather with a broken wiper. Multiple scattering complicates the track fitting and limits the resolution of the momentum measurement.

Figure 30 (left) gives the contributions to the standalone muon momentum resolution versus the incident momentum of the ATLAS barrel muon spectrometer. Multiple scattering (black line) determines the resolution for momenta below  $\sim 200$  GeV. At very low momentum (below 20 GeV) the fluctuations in



**Fig. 29:** Multiple scattering (diffusion) of light passing through a wetter and wetter windscreen (left to right).

the energy loss of the muon traversing the calorimeters becomes the dominant effect (cyan coloured line — the blue line indicates the resolution with respect to the entrance at the muon spectrometer). However, below 100 GeV the momentum measurement is in any case dominated by the inner tracking system. For high-momentum muons the contribution from the intrinsic drift tube resolution and  $r$ - $t$  calibration is of similar magnitude as the expected systematic error in the mechanical alignment, hence the challenge for the alignment system. The right-hand plot in Fig. 30 shows the fractional standalone momentum resolution measured by comparing top and bottom muon spectrometer tracks in cosmic ray data (track splitting method). The measured resolution is compatible with the expected one from Monte Carlo simulation at transverse momenta below 100 GeV, and is degraded at higher momenta. The degradation is caused by imperfect alignment of the muon chambers and by limited timing accuracy because cosmic muons are not synchronous with the artificial LHC clock used in drift time measurements (no fixed time reference).

### 6.5 Muon charge asymmetry in cosmic rays

The charge ratio of positive to negative muons in cosmic rays, with momenta in the range 10–300 GeV, has been measured to be 1.27 at sea level [19], and is expected to increase somewhat with the muon momentum due to a growing influence from kaon decays (the charge ratio of pion decays is expected to be approximately 1.25, while it is 2 for kaons [20]).

In 2006, during the ‘Magnet Test and Cosmic Challenge (MTCC)’, CMS performed a measurement of the muon charge asymmetry on the surface, using a 30° slice of the detector including the muon drift tubes in presence of a 4 T solenoid field [21]. Owing to the high muon rate at the surface, 337 000 high quality tracks with hits in at least 3 (of 4) barrel stations and transverse momentum larger than 3 GeV could be selected. The most important systematic effect on the charge measurement stems from the charge-dependent alignment uncertainty, in particular for high muon momenta. The resolution-induced charge misidentification probability is estimated from Monte Carlo simulation and also contributes significantly to the systematic error above 100 GeV (no inner tracking used). The total systematic error varies between 2% below 10 GeV, ~8% at 100 GeV, and up to and beyond 20% above 100 GeV. It exceeds the statistical errors at all muon momenta. To compare the raw charge ratio measurement with other measurements, the result is expressed in terms of the muon momentum before entering CMS using Monte Carlo simulation. The resulting momentum correction is about +7 GeV and almost independent of the muon momentum. Figure 31 (right plot) shows the charge-ratio measurements versus the corrected muon momentum, together with results from other sources (see references in Ref. [21]). Within their uncertainties, the CMS results can be regarded as independent of the muon momentum, giving the



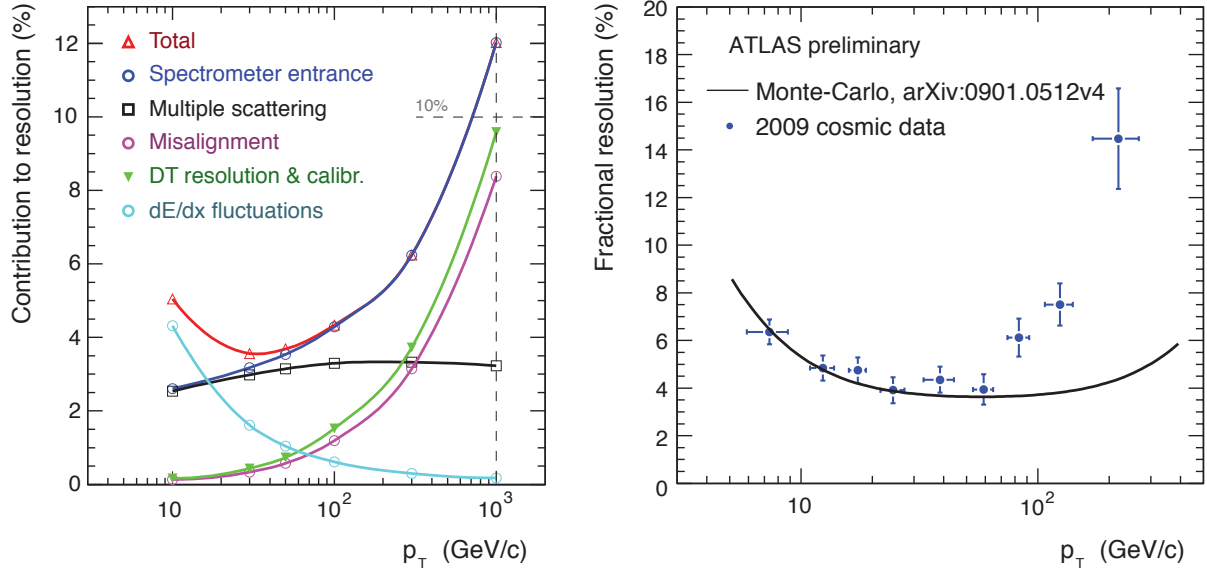


**Fig. 30:** Left: expected contributions to the standalone muon momentum resolution of the ATLAS barrel muon spectrometer (Monte Carlo simulation). See text for a discussion of the various terms. Right: fractional standalone momentum resolution measured by comparing split top and bottom muon spectrometer tracks in cosmic ray data. The degradation of the measured resolution with respect to the expected one is mainly due to imperfect alignment, but also due to  $r$ - $t$  relation inaccuracies due to the missing LHC clock reference.

average  $R_{\mu^+/\mu^-} = 1.282 \pm 0.004 \pm 0.007$ , where the first error is statistical and the second systematic. The left plot in Fig. 31 gives a compilation of previous muon charge-ratio data between 0.1 and 7 TeV taken from a MINOS publication [20]. Superimposed is the model expectation.

## 6.6 Combining muon and inner tracker reconstruction

The comparison of cosmic muon track measurements in the muon system and in the inner tracker allows one to study the momentum scale and the energy loss in the calorimeters, and to tune the Monte Carlo simulation. Figure 32 shows a comparison between standalone track fits to cosmic ray muons in the ATLAS spectrometer and the inner tracker. Shown are the polar and azimuthal angle correlation, the azimuthal angle and impact parameter differences, and the momentum scale difference. A satisfactory agreement is observed between the detectors, and between data (dots) and the Monte Carlo prediction (histograms), showing that the relative alignment and the momentum scales are understood within the available statistics (a single run was used for these plots).

The difference in the momentum scale of 3 GeV on average corresponds to the energy loss of the muons between spectrometer and inner tracker, mainly when traversing the calorimeters.<sup>23</sup> It is well described by the simulation.

## 6.7 Cosmic ray muons in the inner tracker

One of the first measurements performed with cosmic ray muons is the verification of the hit reconstruction efficiency in the silicon trackers, which is expected to be very high ( $> 99\%$ ). The method is as

<sup>23</sup>One can attempt a back-of-the envelope calculation of the expected energy loss to understand the magnitude of the effect. The barrel ATLAS hadronic calorimeter uses iron absorber and plastic scintillator tiles. Inserting the corresponding densities and  $dE/dx$  expectations for cosmic ray muons one finds:  $\langle \Delta E(\text{Had cal}) \rangle \simeq 200 \text{ cm} \cdot (0.4 \cdot dE/dx|_{\text{Fe}} \cdot 11.8 \text{ g/cm}^3 + 0.6 \cdot dE/dx|_{\text{C}} \cdot 2 \text{ g/cm}^3) \approx 2.1 \text{ GeV}$ . Similarly one finds for the electromagnetic liquid-argon accordion calorimeter:  $\langle \Delta E(\text{EM cal}) \rangle \simeq 100 \text{ cm} \cdot (0.4 \cdot dE/dx|_{\text{Pb}} \cdot 16.9 \text{ g/cm}^3) \approx 1.0 \text{ GeV}$ , and for the contribution from the thin solenoid magnet:  $\langle \Delta E(\text{solenoid}) \rangle \simeq 5 \text{ cm} \cdot (0.4 \cdot dE/dx|_{\text{Cu}} \cdot 8.9 \text{ g/cm}^3) \approx 0.1 \text{ GeV}$ . The sum of all contributions gives roughly 3.2 GeV expected energy loss.

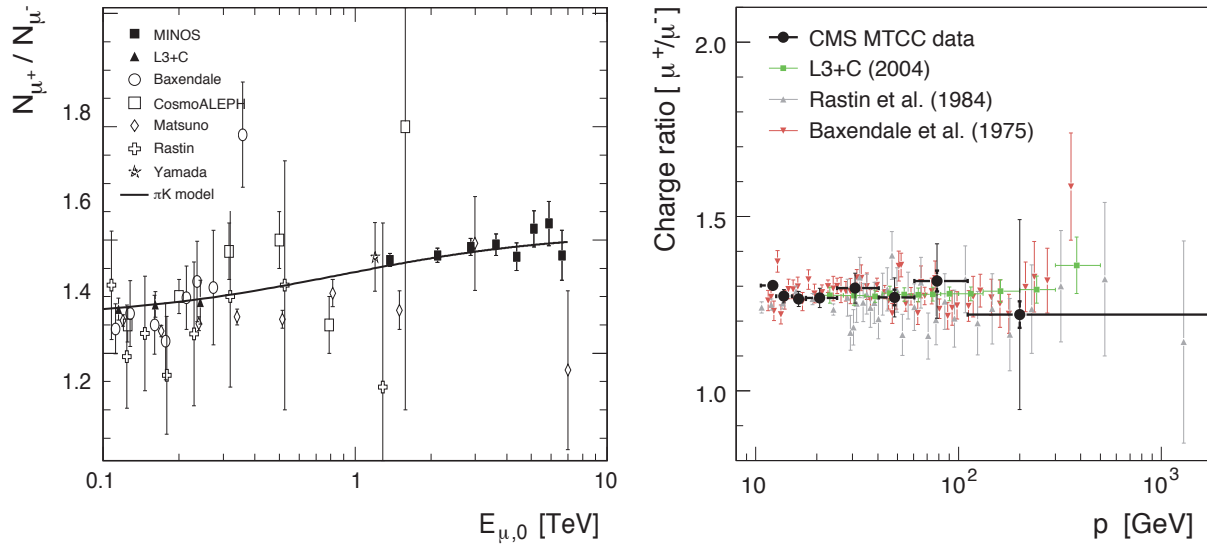


**Fig. 31:** Left: muon charge-ratio measurements compiled by the MINOS experiment [20]. Right: muon charge ratio measured by CMS (black dots) with statistical (bold bars) and systematic errors (thin bars), together with results from other experiments (see Ref. [21] for references).

follows.

1. Selection of good quality tracks by requiring a large number of silicon hits, satisfying goodness-of-fit and a small incident angle.
2. To measure the efficiency of the  $i$ -th layer, the hits from this layer (if there are any) are excluded, and the track is refitted without the  $i$ -th layer.
3. The hit efficiency is computed by searching for hits in the  $i$ -th layer within a narrow road around the refitted track.

The hit reconstruction efficiencies obtained with this method for the ATLAS barrel silicon strip tracker are shown in Fig. 33. Here the tracks were required to have at least 10 hits in the silicon tracker, 30 hits in the transition radiation tracker, and an average  $\chi^2$  per degree of freedom smaller than 2. Furthermore their intersection with the modules had to be within 40 degrees of normal incidence, and there had to be a hit of some kind on the track before and after the module being studied. Finally a guard region around the edge of the active silicon was excluded. The silicon efficiency was then found to be 99.75% on average. Very similar results have been found for the ATLAS pixel detector using the same measurement technique, and also for the CMS silicon pixel and strip detectors.

The hit reconstruction efficiency per straw for the ATLAS transition radiation tracker depends on the distance of the track to the anode wire (maximum distance 2 mm). There is a plateau region below 1 mm where the efficiency reaches 97.2%, decreasing to  $\sim 90\%$  (80%) at 1.5 mm (1.8 mm) and steeply dropping beyond that distance.

## 6.8 Measurement of the Lorentz angle

The solenoid field applies a Lorentz force on moving charges that deflects the track-induced ionisation electrons and holes, travelling through the depleted substrate of the silicon junction along the high-voltage potential (Hall effect). The deflection angle is denoted *Lorentz angle*. The value of the Lorentz angle depends on the mobility of the charge carriers as well as the external magnetic field. For silicon immersed in a magnetic field  $B$  the Lorentz angle  $\alpha_L$  is given by  $\tan \alpha_L = \mu_H B = \gamma \mu_d B$ , where  $\mu_H$  is the Hall mobility,  $\gamma$  represents the Hall factor which is of order unity, and  $\mu_d$  is the drift mobility, which is a



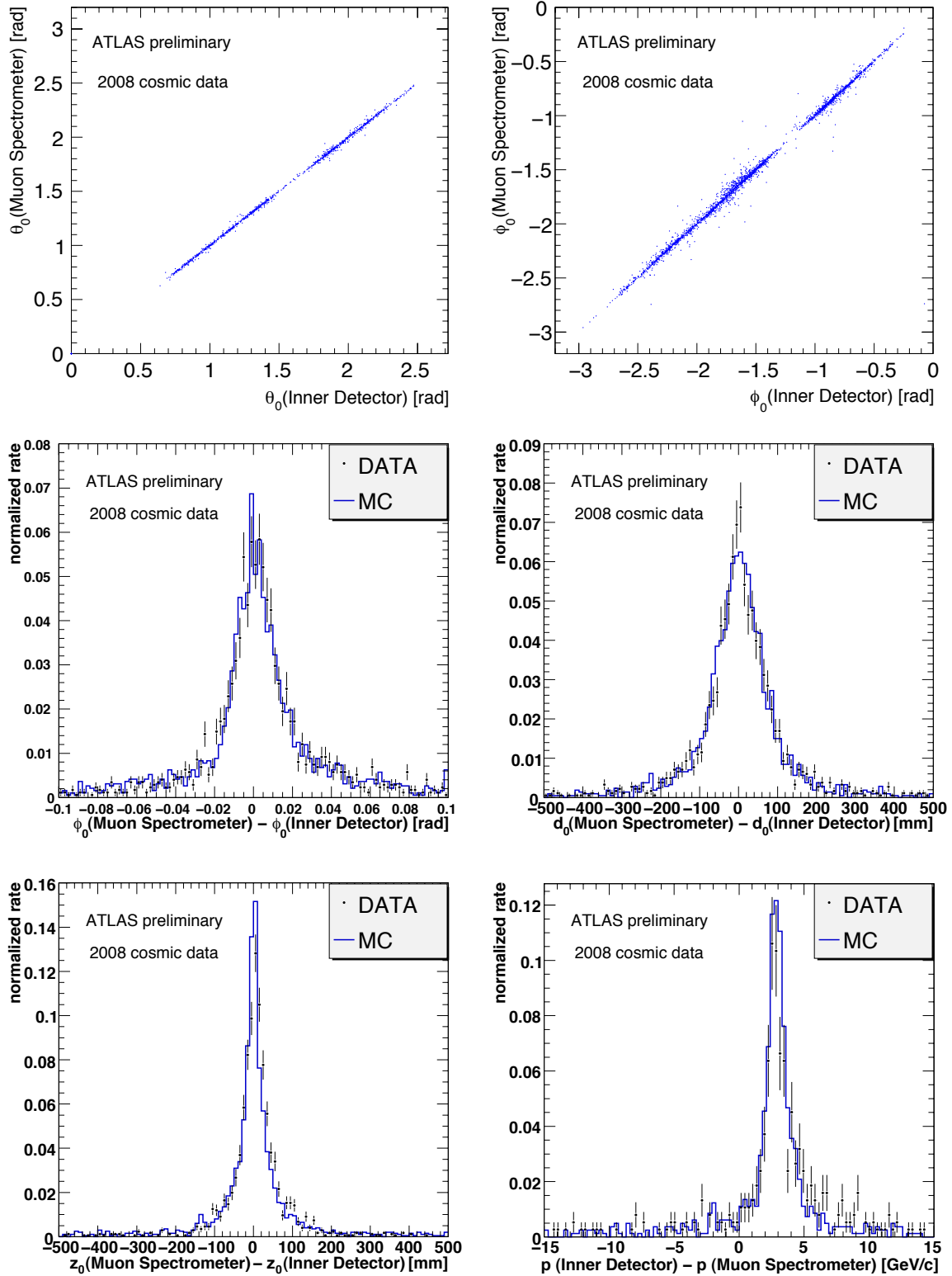


**Fig. 32:** Comparison between standalone track fits to cosmic ray muons in the ATLAS muon spectrometer and the inner tracker. Shown are the polar and azimuthal angle correlation (upper plots), azimuthal angle and impact parameter differences (middle and lower left plot), and momentum scale difference (lower right plot, sensitive to the energy loss of the muons when traversing the calorimeters). The dots are data and the histograms correspond to the Monte Carlo prediction.

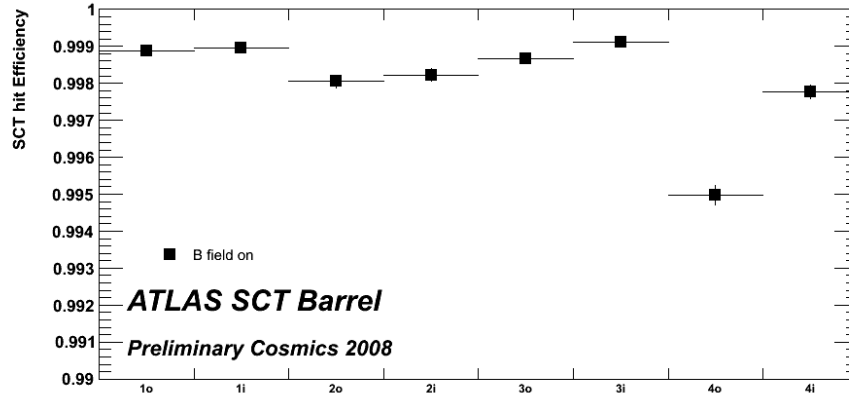


**Fig. 33:** Hit efficiencies for the ATLAS barrel silicon strip tracker as measured with cosmic muon tracks (see text for details of track requirements and procedure).

function of the ratio of drift velocity to the electric field induced by the bias voltage. The drift velocity for both electrons and holes saturates at high electric field. This leads to a drop in the mobility thus decreasing the Lorentz angle.<sup>24</sup>

Figure 34 sketches the Lorentz deflection effect. Owing to the opposite charge of electrons and holes, both carriers are deflected into the same transverse direction along the Lorentz force. The deflection generates a bias in the position measurement (cluster barycentre) of the track incident in the silicon strip or pixel. The bias could be reduced by tilting the modules in the direction of the Lorentz angle, and indeed the modules in the ATLAS and CMS silicon detectors are tilted (*shingled*). The values for the tilts chosen are, however, due to technical reasons to allow overlaps between adjacent modules.<sup>25</sup> Instead of a mechanical solution, the position bias due to the Lorentz deflection is corrected by software. The correction must be recalibrated at regular intervals because the size of the depletion region in the semiconductor reduces with rising irradiation and constant bias voltage, thus reducing the position bias.

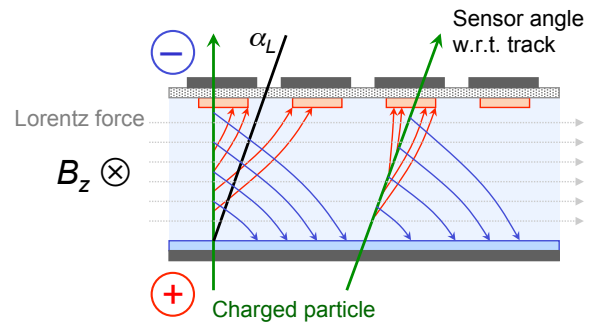


**Fig. 34:** Sketch illustrating the deflection of moving ionisation charges in the solenoid field, leading to a bias in the position measurement. Tilting the modules by the amount of the Lorentz angle  $\alpha_L$  would correct for the bias.

The Lorentz angle is determined empirically by minimising the measured cluster width of hits on tracks. Figure 35 shows the cluster width versus the cosmic muon track incident angle with respect to the module normal for the ATLAS barrel silicon strip tracker. Measurements with and without magnetic field are shown. The value of the Lorentz angle, extracted at the minimum cluster size, is found to be  $\alpha_L = (3.93 \pm 0.03 \pm 0.10)^\circ$ , where the first error is statistical and the second systematic (for comparison, the Lorentz angle for the ATLAS pixel device is  $12.3^\circ$ ).

<sup>24</sup>The electron and hole mobility and hence the Lorentz angle also depend on the temperature: increasing temperature reduces the mobility and thus the Lorentz angle.

<sup>25</sup>In ATLAS the chosen tilts with respect to the pointing axis are 11 degrees ( $-20$  degrees) for the silicon strip tracker (pixel tracker), whereas the Lorentz angle for non-irradiated modules is 4 degrees (13 degrees).

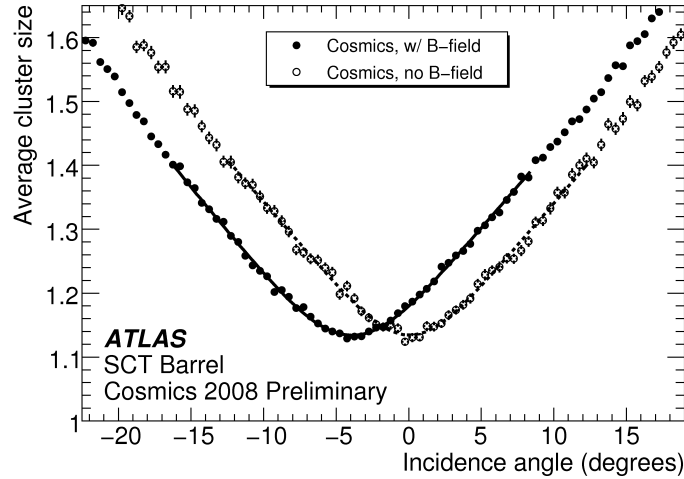


**Fig. 35:** Measurement of the mean cluster size versus the incidence angle with respect to the module normal in the ATLAS barrel silicon strip tracker, using cosmic ray muon tracks. Measurements with and without magnetic field are shown (the Lorentz angle vanishes without external field). The value of the Lorentz angle is extracted from the position of the minimum cluster size.

## 6.9 Particle identification with transition radiation

Hits from ultrarelativistic particles, generating transition radiation photons in the keV range that contribute to the gas ionisation in the ATLAS transition radiation tracker (TRT), are identified via dedicated high-threshold readout. It turns on at a gamma factor above  $\simeq 1000$  (with  $p = \beta\gamma m \simeq \gamma m$ , the threshold momenta for  $\gamma = 1000$  are 0.5 GeV, 105 GeV and 139 GeV for electrons, muons and pions, respectively), and thus essentially only for electrons in the typical energy range, so that it can be used for electron identification.

The principle of the creation of transition radiation via an electric dipole is sketched in Fig. 36. Figure 37 shows the high-threshold hit probability obtained for the ATLAS barrel TRT from 2004 combined test beam data (*cf.* Section 5) for different particle species (left plot), and for cosmic ray muons (right plot). The turn-on curves are found to be in good agreement.

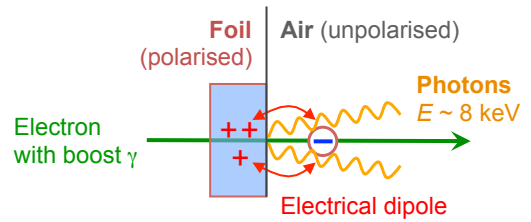


**Fig. 36:** Transition radiation is produced when charged ultrarelativistic particles traverse the boundary of two different dielectric media (e.g., polymer fibres/foil and air). The radiation is intense enough to be measured for  $\gamma > 1000$  and more than 100 boundaries.

## 6.10 Calorimeter performance with cosmic ray muons

Cosmic ray muons have also been exploited by the calorimeter groups of ATLAS and CMS to study pulse shapes, and occupancy distributions, detect bad channels, understand the muon energy loss in the calorimeters and tails in energy distributions, and for energy inter-calibration purposes.

The total energy sum of all cells along a muon track in the ATLAS hadronic calorimeter is shown in the left-hand plot of Fig. 38. The peak of the minimum-ionising particles (i.e. a particle whose mean energy loss rate through matter is close to the minimum), is well distinguished from the correspond-

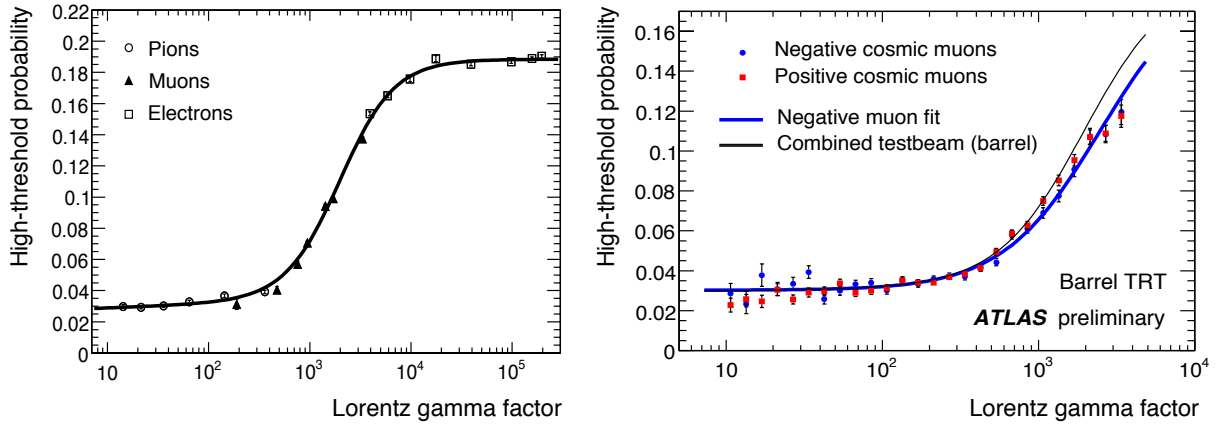


**Fig. 37:** Left: average probability of a high-threshold hit in the ATLAS barrel transition radiation tracker (TRT) as a function of the Lorentz  $\gamma$  factor for electrons (open squares), muons (full triangles) and pions (open circles) in the energy range 2–350 GeV, as measured in the 2004 combined test beam. Right: transition radiation turn-on versus  $\gamma$  in the ATLAS barrel TRT for cosmic muon tracks. The data points are shown for both muon charges (positive: red dots, negative: blue dots) and are compared with test beam results (black line). The blue line gives a fit to the results obtained with the cosmic data.

ing noise distribution obtained from randomly triggered events. The energy of the cosmic ray muons deposited in the active parts of the hadronic calorimeters of ATLAS and CMS exceeds the one in the electromagnetic calorimeters by approximately a factor of 10. The ionisation energy loss of the muons when traversing the electromagnetic calorimeters is measured by comparing the momenta between the muon system and the inner tracker (*cf.* Fig. 32). It can be correlated on an event-by-event basis to the measured calorimeter energy deposits. This has been done by CMS in the right-hand plot of Fig. 38, where the average electromagnetic calorimeter deposits are drawn versus the muon momentum. Overlaid is the expected energy loss, which is found to be in good agreement with the measurement. The results indicate the correctness of the tracker momentum scale and of the calorimeter energy scale calibrated with electrons at test beams.

The energy deposition can also be directly compared to Monte Carlo simulation, as done by ATLAS in the upper plot of Fig. 39 (see Ref. [22]), showing the energy reconstructed in the first and second layers for data and Monte Carlo cosmic ray events. Good agreement is observed up to the tails both for the shape and the absolute scale. This result can be used to measure the uniformity in the energy response of the calorimeter versus the pseudorapidity by integrating over the response in the azimuth angle (the statistics is insufficient to make a full  $\eta \times \phi$  uniformity map). The estimation of the muon energy is done with a fit of the cluster energy distribution using a Landau function, which accounts for fluctuations of the energy deposition in the ionisation process, and a Gaussian describing essentially electronic noise (and also cluster non-containment). The response uniformity is computed from the RMS of the normalised difference between the data and Monte Carlo most probable values (MPV) of the Landau distribution in each  $\eta$  bin. The resulting distribution for the second (and main) liquid-argon calorimeter layer in ATLAS is shown in the lower plot of Fig. 39. The observed dispersion is in agreement with statistical fluctuations, i.e., no significant non-uniformity is seen at the per cent level. Similar results have been obtained by CMS where an intercalibration with cosmic muons (aligned to the crystal axis and with a reference energy of 250 MeV (MPV)) achieved an intercalibration of better than 1.5% in the barrel and better than 2.2% in the forward region. All 36 CMS crystal supermodules could thus be intercalibrated with cosmic muons, which was an important achievement because only 9 supermodules (25%) had been calibrated with electron test beam data prior to the calorimeter installation.

The reconstruction of jets and missing transverse energy requires the electromagnetic and hadronic

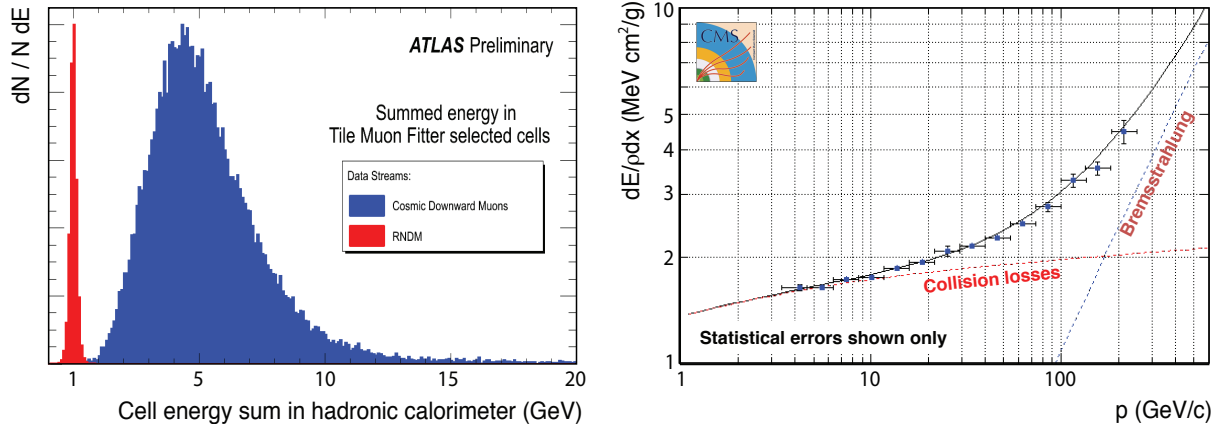


**Fig. 38:** Left: total energy sum of all cells along a muon track in the ATLAS hadronic calorimeter (blue) and the corresponding noise distribution obtained from randomly triggered events (red). The minimum ionising muon signal is well separated. Right: average energy deposits in the CMS electromagnetic calorimeter versus the muon momentum measured in the tracking devices. Overlaid is the expected energy loss for the lead-tungsten calorimeter. Indicated by the dotted lines are the contributions to the energy loss from collisions (red) and bremsstrahlung (blue).

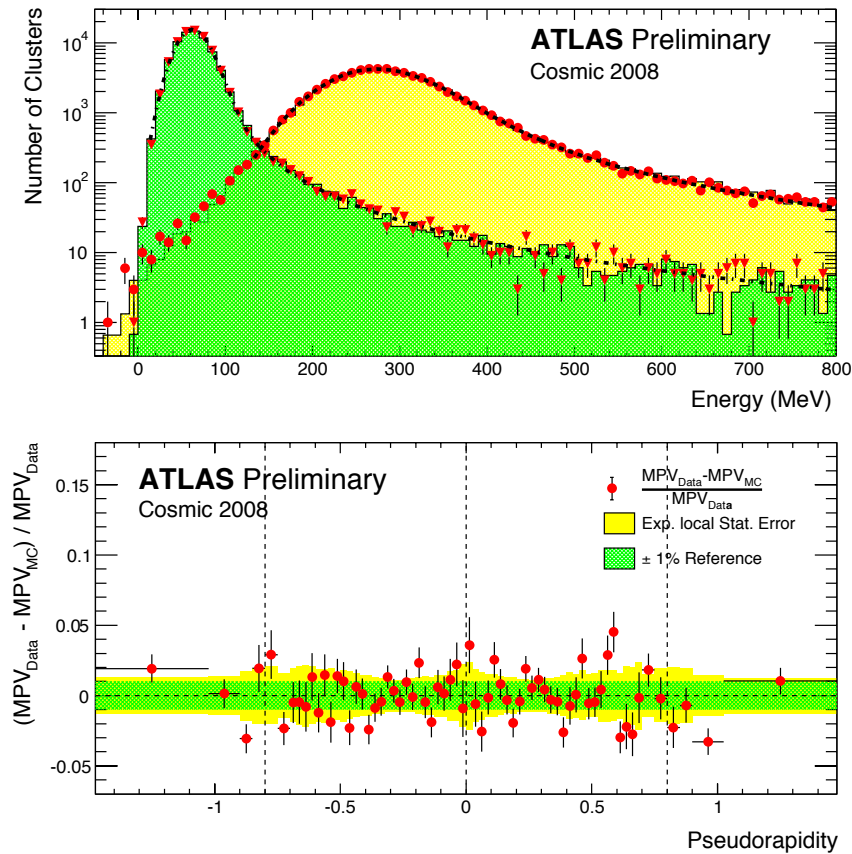


**Fig. 39:** Top: reconstructed cosmic muon energy in a  $2 \times 1$  cluster in the first layer (dark shaded/green histogram for Monte Carlo and triangles for data) and in a  $1 \times 3$  cluster in the second layer (light shaded/yellow histogram and dots for data) of the ATLAS electromagnetic calorimeter. Bottom: electromagnetic calorimeter energy response dispersion between data and Monte Carlo simulation versus the pseudorapidity, as measured with cosmic muons for the second (main) layer of the ATLAS electromagnetic calorimeter. The dark shaded (green) band indicates the  $\pm 1\%$  region for reference, and the light shaded (yellow) band indicates the expected statistical accuracy ( $1\sigma$  error band) of the measurement.

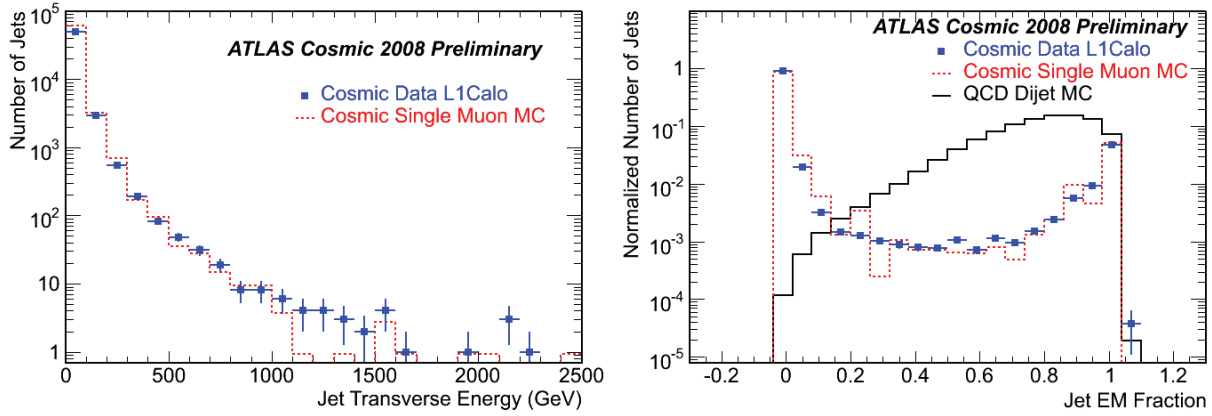


**Fig. 40:** Left: distribution of the jet energy for data (dots) and Monte Carlo simulation (dotted histogram). Only events with at least one jet that exceeds 20 GeV transverse energy are included. The Level-1 trigger inefficiency and cosmic air showers are not simulated. Right: electromagnetic fraction of jets for data (dots) and Monte Carlo (dotted), where the fraction is defined by the ratio of energy deposited in the electromagnetic calorimeter divided by the total deposited energy. The distributions are normalised to unity. Only jets with  $E_T > 20$  GeV are included. Shown by the solid histogram is the expected distribution for QCD di-jet events as they originate from proton–proton collisions.

calorimeter responses to be combined. It can be studied with highly energetic cosmic muons releasing a Level-1 calorimeter trigger-accept signal. Jets from muon showers with energies exceeding the TeV scale are found in the data. Figure 40 (left) shows the distribution of the jet energy for calorimeter triggered events for data and Monte Carlo simulation. Because the simulated data do not include the Level-1 trigger inefficiency, the Monte Carlo distribution is normalised to data in the 100–300 GeV range. Only events that have a jet with  $E_T > 20$  GeV are included in the figure. Good agreement between data and simulation is observed. A small excess at large transverse energy in data may be due to air-showers, not included in the simulation. The right-hand plot in Fig. 40 shows the electromagnetic (EM) fraction of jets for data and Monte Carlo, where the fraction is defined by the ratio of energy deposited in the electromagnetic calorimeter divided by the total deposited energy. The distributions are normalised to unity. As before, only jets with  $E_T > 20$  GeV are included. Also shown for comparison is the distribution expected for QCD di-jet events as they originate from proton–proton collisions. The most likely value for the EM fraction is 0 or 1 for fake jets from cosemics, because the high energy deposition from photons originating from highly energetic muons will localise either in the electromagnetic or the hadronic calorimeter. QCD jets have a broad distribution of the EM fraction with a maximum at around 0.8. Electromagnetic fractions less than 0 or larger than 1 are due to small negative energy contributions from noise. One concludes from the plot that good separation between QCD jets and fake jets from cosmic rays can be obtained by vetoing jets with EM fractions close to 0 and 1.

## 7 Commissioning with single proton beam data

A lucky period between September 10 and 13, 2008, with — for the first time — single beams of 450 GeV LHC injection energy circulating in both directions of the LHC, gave the experiments the opportunity to commission the detector and the data taking chain with proton-beam background in synchronisation with the LHC clock. A single ‘pilot’ bunch containing approximately 3 billion protons — radio-frequency captured and not, with closed and open collimators, stably circulating or lost — travelled through the injection chain, transfer lines and finally the LHC. The single-beam exercise at injection energy was briefly repeated in 2009, at the restart of the LHC after an accident that caused a one-year delay in the commissioning and physics schedule.



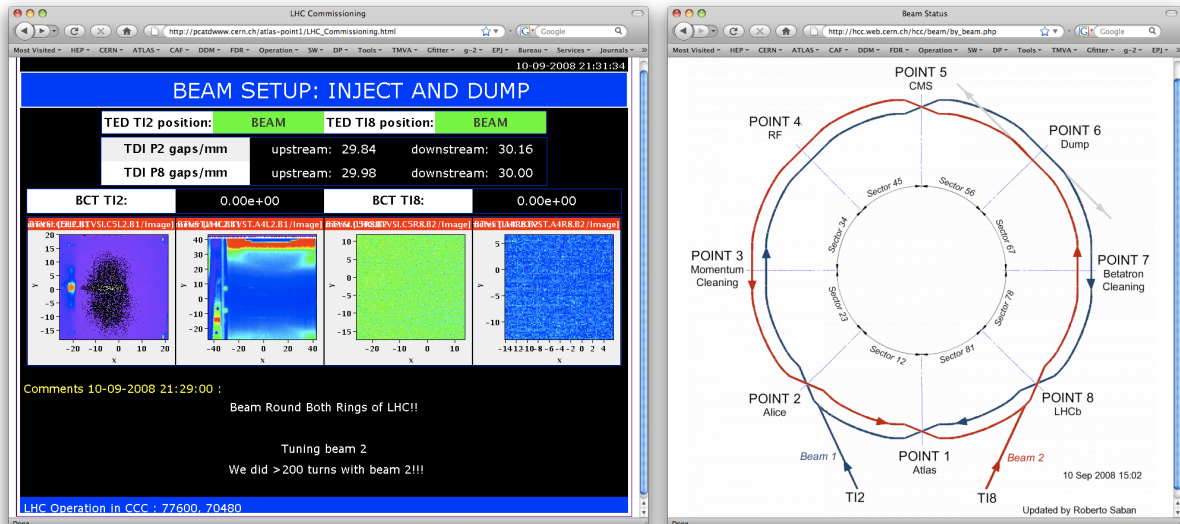


**Fig. 42:** Main LHC information displays sent from the CERN Control Room (CCC, ‘Triple-C’) to the experiments and the interested world. The left picture displays basic quantities such as the currents (in number of protons per bunch) passing through the two transfer lines serving to inject the LHC beam lines. Apart from displaying sometimes cryptic information displays and plots, it features useful operator comments on the bottom of the display: “Beam Round Both Rings of LHC !!” (one notices the capital letters and the abundant use of exclamation marks, which appropriately reflect the mood of the day). The right panel is a sketch of the two LHC beams. The colour codes are important: Beam Blue (1) must *always* be blue, and Beam Red (2) must *always* be red (source: Steve Myers, LHC coordinator). The detectors are located at four out of eight straight sections: Point 1 (ATLAS), Point 2 (ALICE), Point 5 (CMS) and Point 8 (LHCb). The remaining four straight sections serve beam acceleration, beam cleaning and dump purposes (see Section 2).

Figure 42 shows two of the most important information panels provided to the experiments (and the general public) by the LHC operators. One notices the particular location of Point 1 (ATLAS cavern) on the right panel: both beams need to make a full turn before reaching ATLAS. It was hence the last experiment to see beam, and it is affected by any problem along the beam line. A few photographs taken on 10 September in the LHC, ATLAS, CMS, and LHCb control rooms are shown in Fig. 43.



**Fig. 41:** The Google search page at ‘Jour J’ — the LHC start-up, 10 September 2009.

## 7.1 Beam-on-collimator events

Somewhat unexpectedly and all of the sudden, events where the entire detector was lit appeared on the event displays. A few typical events are collected in Fig. 44. The reaction in the ATLAS control room upon the arrival of the first event is witnessed by the photo in Fig. 47. *What happened?*

The events seen belong to so-called ‘beam splash’ type events, which originate from pilot-beam-on-collimator dumps. Collimators are placed at a distance of about 140 m on both sides of the experiments. If they are closed, the beam dumps on them, producing an avalanche of scattered particles that reach the detector. For such an event occurring every 42 seconds during a short period ATLAS typically recorded 300 000 silicon strip tracker hits (on lowered voltage for safety reason, reducing the hit efficiency; the pixel detector was switched off) and 350 000 transition radiation tracker hits, approximately all passing high-threshold discrimination. The sum of all calorimeter cells in these events exceeds 3000 TeV. Moreover 350 000 drift tube hits were recorded in the muon spectrometer and 320 000 (65 000)



**Fig. 43:** Snapshots taken on 10 September in the LHC (upper left), ATLAS (upper right), CMS (lower left), and LHCb (lower right) control rooms, exhibiting untypical occupancy.

muon trigger hits in the barrel (endcaps). Apart from being spectacular, beam splash events are useful in many ways for the experiments. Their main purpose is to serve timing-in the various detector parts and systems including the trigger with respect to each other. It is also interesting to correlate position and energy response in splash events, and to use them to identify dead channels. In the November 2009 beam splash period, after the LHC restart, it was also possible to exercise, for the first time in realistic conditions, the ATLAS standalone beam abort system using the diamond Beam Condition Monitor (BCM) detectors. By lowering the abort thresholds, a deliberate BCM beam abort was triggered by a beam splash event reaching ATLAS. No fake abort was observed. Beam splash events have also been observed in the forward detectors of the experiments, designed to measure the relative luminosity. In total, ATLAS recorded about 70 beam splash events (of a total of approximately 100 delivered) in September 2008, and another 106 events (all triggered) in November 2009. CMS received and recorded an order of magnitude more beam splash events.

An example for a timing study is given in Fig. 45. Shown in the left plot is the mean hit time (expected minus measured) versus the endcap disk, where a larger absolute number corresponds to a larger absolute pseudorapidity. The measurement corresponding to a single beam-splash event is shown. The event arrives from the A-side (+ $z$  side) so that the hit time behaves as expected for a collision event for the far side (C-side), but wrongly for the A-side with respect to the expected collision timing used in the event reconstruction (the event comes from behind and the hit time is thus anticipated). A similar behaviour is observed for all other detector systems.

Beam splash events from both sides can be used to adjust the timing for both far sides. The right plot in Fig. 45 shows the mean time residual along the  $z$  coordinate of all ATLAS muon drift tube chambers using the synchronous front of splash particles and the very large particle flux. A linear relation



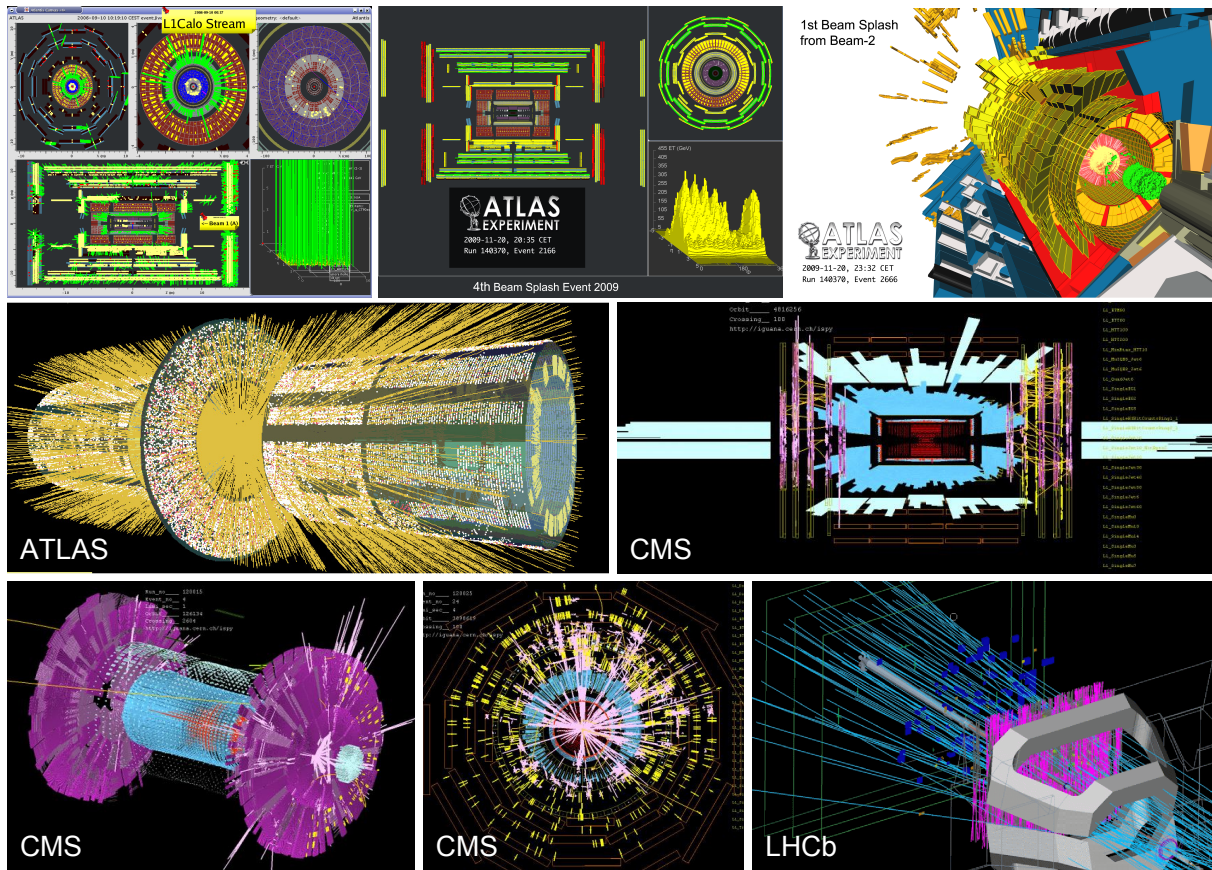


**Fig. 44:** Event displays of beam-on-collimator ‘splash’ events recorded by ATLAS (upper plots and centre left), CMS (centre right, lower left and middle), and LHCb (lower right).

is found with a slope determined by the speed of light. A timing study with beam splash events in the CMS hadronic calorimeter is shown in Fig. 46. Drawn are the differences between reconstructed and expected cell times for beam splash events before (left panel) and after timing adjustment (right) using previously measured beam splash events. The large deviations from zero in the left panel are due to collision time settings. CMS also correlated the energy deposits in the hadronic and electromagnetic calorimeters for beam splash events, reproducing nicely the expected linear dependence and a relative coefficient of  $E_{\text{HCAL}} \simeq 6.5 \cdot E_{\text{ECAL}}$ .

## 7.2 Beam background events

After the beam splash events, the collimators were all opened allowing the beam to circulate in the LHC and to pass by the experiments. Beam passages without interactions are measured primarily in the beam pickup detectors based on electrostatic current induction. These detectors are installed  $\pm 175$  m away from the interaction points of the experiments (many more such beam pickups are installed along the LHC for beam monitoring purposes). They provide input signals to the Level-1 triggers, indicating filled LHC bunches, and also a time reference for the detector systems. In case of beam collisions, the coincidence of signals in the two beam-pickup detectors can be used to identify colliding bunches and, more importantly, their timing difference (measured by an oscilloscope) can be used as input to the beam



**Fig. 47:** A ‘beam splash’ event being seen in the ATLAS control room.

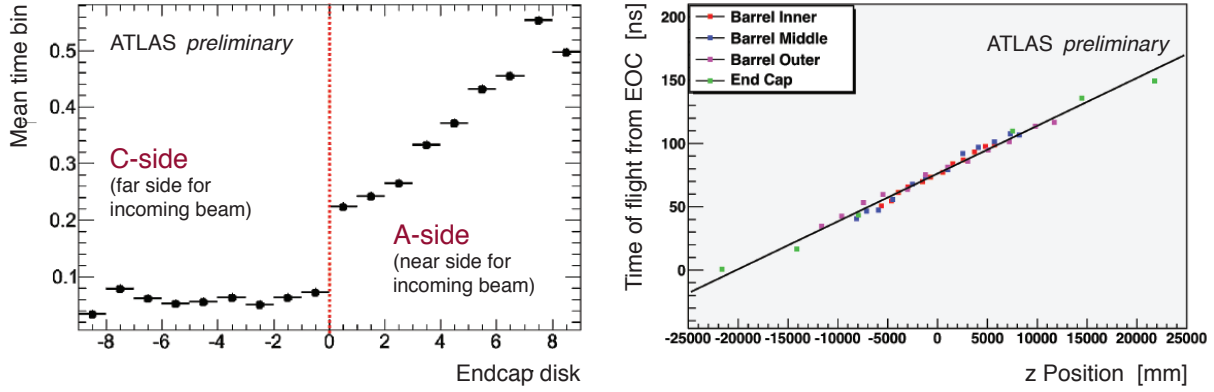


**Fig. 45:** Left: timing properties of a single beam-splash event originating from the A-side in the ATLAS silicon strip tracker (see text). Right: time residual versus the  $z$  coordinate along the ATLAS muon drift tube chambers for a beam splash event. The slope is determined by the speed of light.

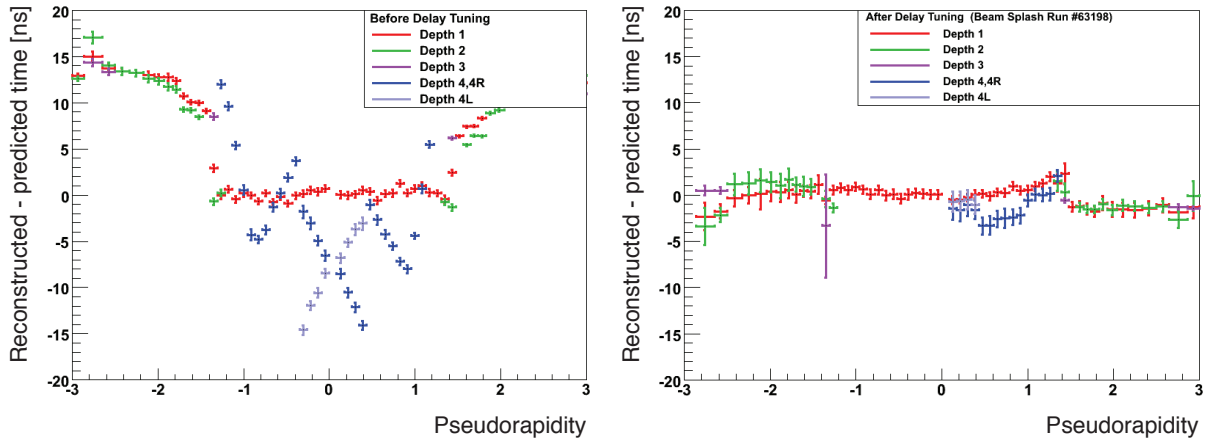


**Fig. 46:** Difference between reconstructed and expected cell time versus the pseudorapidity for beam splash events in the various layers and geometrical regions of the CMS hadronic calorimeter. Left is uncorrected assuming collision timing, and right is after correction with the use of previously observed events.

‘cogging’, that is a relative radio-frequency phase adjustment of the bunches to ensure collisions in the interaction point ( $z = 0$ ) without longitudinal shift. In the Level-1 trigger the beam pickup signals are put in coincidence with the other triggers to reduce background from cosmic rays. This requires, however, a proper timing-in of the various trigger signals.

Circulating single-beam bunches can also provide beam-related background particles that are measured by the experiments. At low beam intensities, there are two main sources of beam backgrounds referred to as ‘beam–gas interactions’, which are interactions of beam particles with residual gas in the beam pipe or with the beam pipe wall. Via the decay of pions such a process also produces muons, which travel with the proton beam in what is called the ‘beam halo’ (usually referred to as ‘beam-halo background’, which is what seems to be the primary single-beam background seen so far in the detectors). Such beam related backgrounds originating from fixed-target collisions are strongly boosted in the forward direction. Figure 48 shows the distributions of the track polar angle with respect to the beam axis for single-beam data, simulated beam-halo background, and cosmic ray events taken with no beam present in the LHC. Whereas the beam background peaks at small angles, cosmic ray tracks peak at larger values, which are, however, much below the  $\sim 1.5$  rad that would be expected, because a forward trigger has been used to select these events. The orange shaded histogram shows the distribution of single-beam

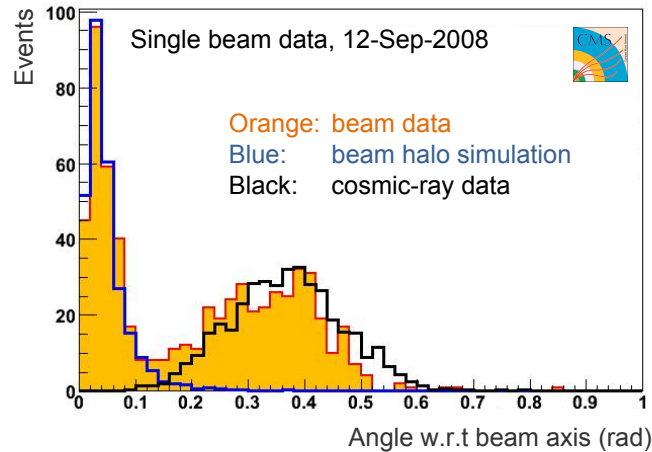


**Fig. 48:** Distributions of the track polar angle with respect to the beam axis obtained by CMS for single-beam data (orange shaded), beam-halo background simulation (blue line), and cosmic ray data with no beam (black line).

events accepted by the same trigger. One clearly distinguishes the beam-related background from the cosmic muon contamination.

Event displays of beam background events with halo muons taken by ATLAS and CMS are shown in Fig. 49. In ATLAS the toroidal magnetic fields in the muon spectrometer bend the muon tracks longitudinally in the  $z$  coordinate.

### 7.3 Radio-frequency bunch capture

After injection into the LHC, the protons in a bunch start to spread longitudinally and transversely due to their mutual repulsion. Within milliseconds the bunch thus ‘debunches’.<sup>26</sup> Debunching can be directly observed by the experiments via a decaying beam pickup signal during circulating beam. An example for this is displayed in the upper plot of Fig. 50 showing the beam pickup signal amplitude in volts versus the time in nanoseconds as measured by ATLAS. The spikes represent the induced signal when a bunch passes nearby an ATLAS beam pickup detector. The time difference between adjacent spikes amounts to  $89\text{ }\mu\text{s}$ , which corresponds to an LHC revolution period. The signal weakens while the bunch disintegrates. The lower panel of Fig. 50, sketches the radio-frequency field bucket structure of the LHC. A bunch filled with protons is captured within a bucket of  $2.5\text{ ns}$  length (precisely:  $2.495\text{ ns}$ , i.e., a radio frequency of  $400.79\text{ MHz}$ ).<sup>27</sup> Only every tenth bucket is filled providing the design bunch period of  $25\text{ ns}$ .

Figure 51 shows a series of attempts in September 2008 to capture a bunch in the LHC within a radio-frequency bucket. The horizontal lines represent a measured beam pickup signal after 10 LHC turns. The leftmost plot shows the decaying bunch in absence of a radio-frequency (RF) field. The signal induction from the debunched beam becomes unmeasurable after 250 turns. The centre-left plot shows a first capture attempt, at a wrong injection phase, so that the bunch is split into two by the RF field, leading to a fast decay. For the centre-right plot the injection phase has been improved, but is still shifted with respect to the RF phase, leading to a moving proton package and a fast decay. Finally, the rightmost

<sup>26</sup>Debunching can also be useful. For example, controlled debunching and rebunching can be used to split and multiply bunches in the injection chain of an accelerator. This is, however, a delicate technique which is not used for bunch splitting in the LHC injector (PS).

<sup>27</sup>The radio-frequency electrical field together with the relativistic contraction provide a stronger longitudinal constraint on the bunch size than the bucket length. At  $450\text{ GeV}$  beam energy, the longitudinal RMS of the bunch is expected to be around  $8\text{ cm}$ , (the measured values were found to be significantly lower than that) decreasing to approximately  $6\text{ cm}$  at  $7\text{ TeV}$  design energy.

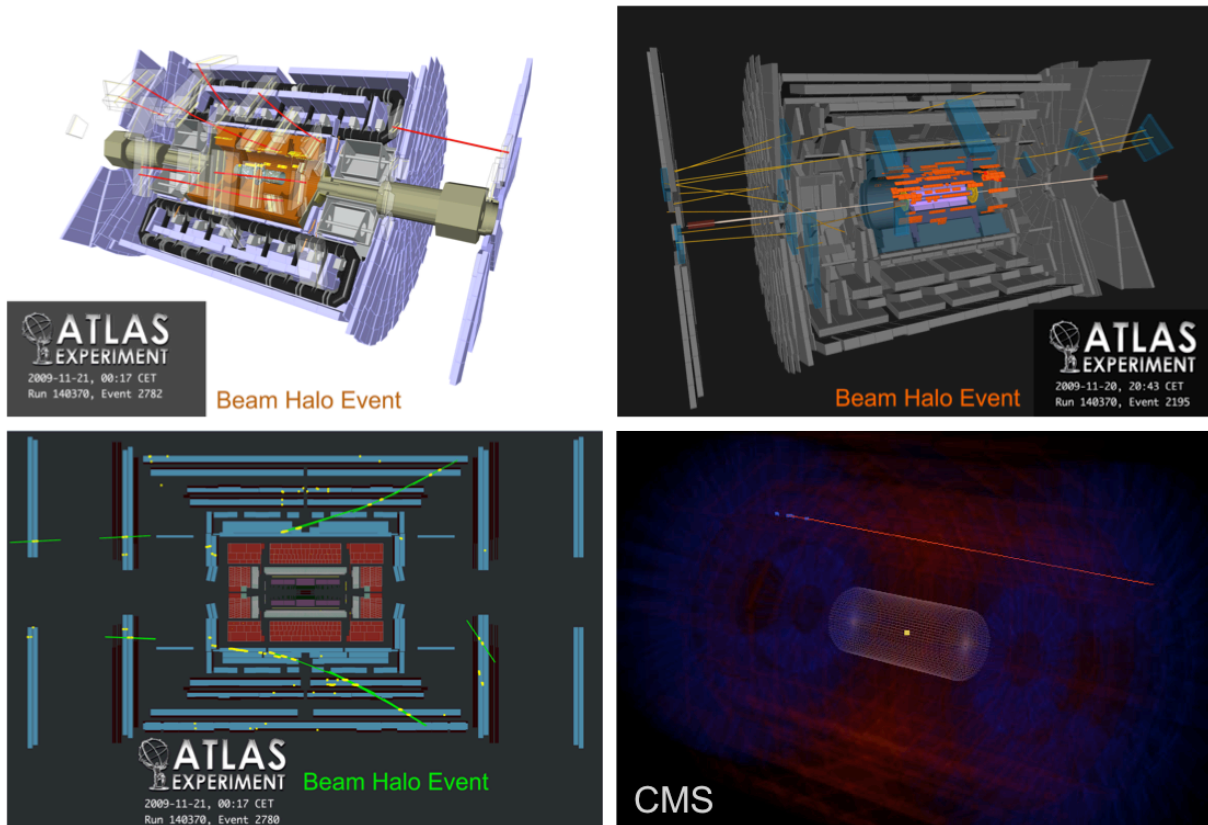


**Fig. 49:** Beam-related background events with halo muons taken by ATLAS and CMS (lower right) in November 2009.

plot shows an accurate injection phase and a properly captured bunch. No decay of the signal due to limited lifetime can be noticed.

Since the experiments record events triggered by the beam pickup signals and, by running synchronously with the LHC clock, also store the bunch crossing number that led to the trigger accept, it is possible to measure the beam debunching *and* its capture in an RF bucket. Such a measurement has been performed by CMS and the result is shown in Fig. 52. Before the RF capture the bunch crossing number of the triggered events is spread over many bunches. After successful RF capture all triggered events have the same bunch crossing number 831 as seen by the spike in the distribution at that point.

## 8 Early physics at the LHC — Overview

The major part of the LHC proton–proton physics programme can be grouped under the following grand themes.

1. **Mass** — search for the Higgs Boson.
2. **Electroweak unification** — precision measurements ( $W$  and top masses) and tests of the Standard Model.
3. **Hierarchy in the TeV domain** — search for supersymmetry, extra dimensions, new symmetries in the TeV domain, and other exotic phenomena.
4. **Flavour** —  $B$  meson mixing, rare decays and  $CP$  violation as tests of the Standard Model.

This programme is also reflected in the ATLAS and CMS physics organisation, separated into so-called ‘physics objects groups’ (CMS) or ‘combined performance groups’ (ATLAS), and ‘physics analysis



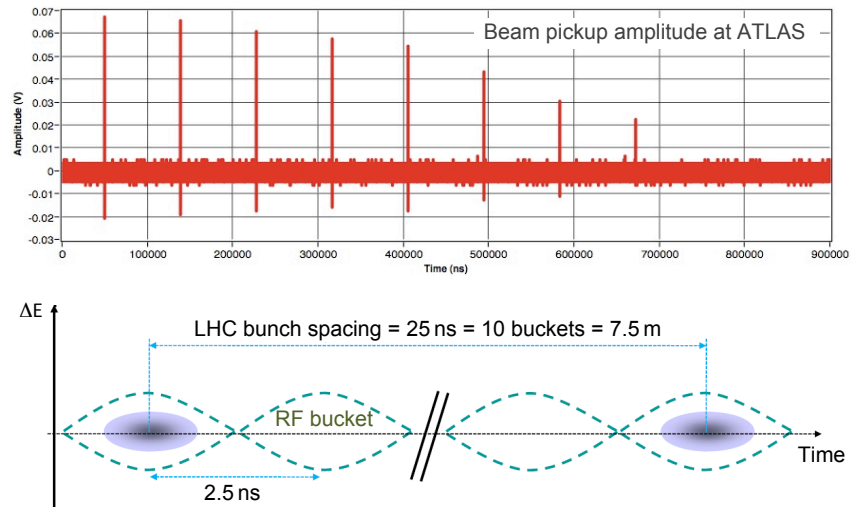


**Fig. 50:** Top: decaying circulating beam signal in an ATLAS beam pickup detector due to beam debunching. Bottom: bucket and bunch structure in the LHC.

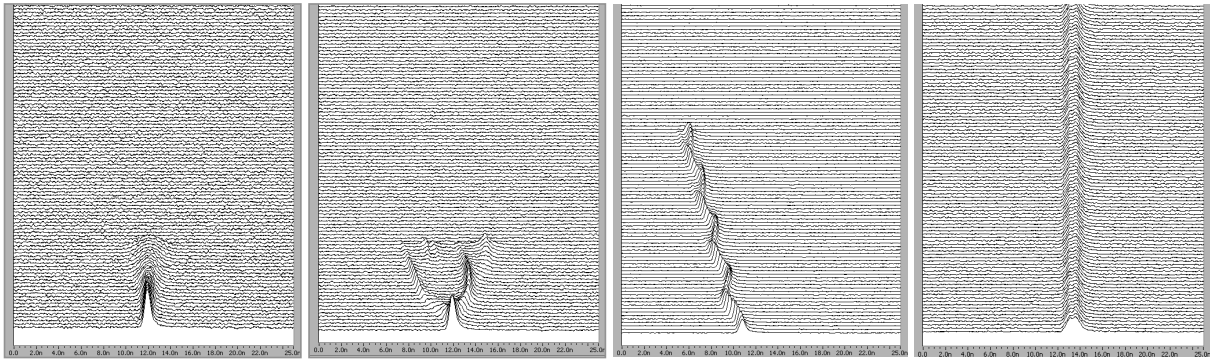


**Fig. 51:** Attempts and successful (rightmost plot) radio-frequency capture of a bunch in the LHC. Each horizontal line represents 10 LHC turns. See text for a discussion of the plots.

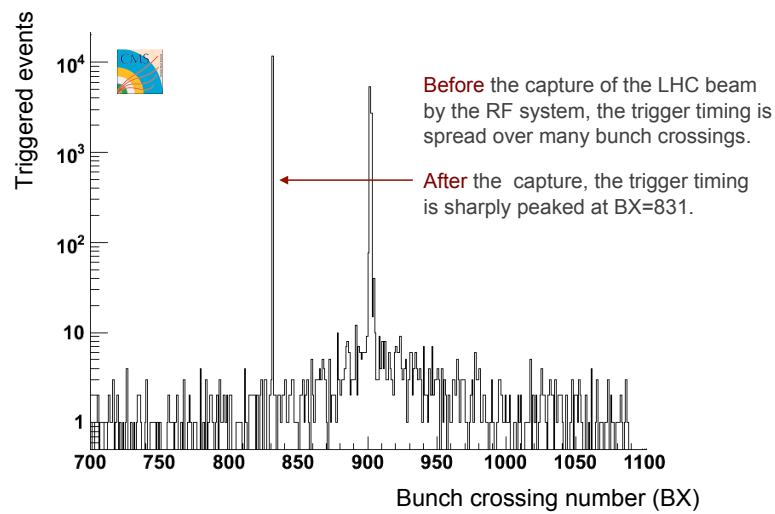
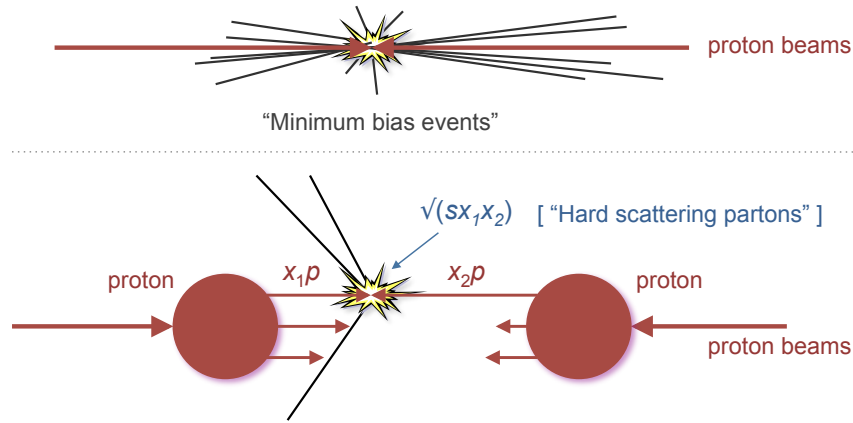


**Fig. 52:** LHC bunch decay and radio-frequency capture as measured by CMS.

groups'. The former groups provide the reconstruction of the objects that combine various detector systems and that are common input for physics analysis. They are subdivided into 'e/gamma', 'jets/missing transverse energy', 'hadronic tau', 'muons' and 'flavour tagging' groups. The physics groups are organised in 'Standard Model' containing QCD, electroweak and diffraction physics, 'B physics', 'Top', 'Higgs', 'SUSY', 'Exotics', 'Heavy ions', 'Luminosity', and 'Monte Carlo generators' subgroups.

Since protons are made out of quark and gluon constituents ('partons'), collisions of protons are complex scattering processes involving elastic, diffractive (single and double), inelastic non-diffractive and central diffractive interactions (pomeron–pomeron scattering). The large majority of the proton–proton events are due to interactions at large distances. The inclusive sum of single and double diffractive, and non-diffractive processes are called 'minimum bias' events, in allusion to lowest transverse momentum events that can be selected by a trigger, and in contrast to 'zero-bias events', which can only be obtained if all events or a random sample of events are selected. The total minimum bias cross section at 14 TeV centre-of-mass energy at the LHC is approximately 70 mb. It dominates by orders of magnitude the primary physics channels of interest. Minimum bias events are characterised by tracks with small transverse momenta of  $\langle p_T \rangle = 0.5$  GeV on average.



The constituents of the protons participating in the interaction carry only a fraction of the proton's momentum. The fraction is governed by parton distribution functions that cannot be predicted from first principles and are taken from experiment. The complexity of describing proton–proton interactions includes, besides the hard scattering as described by parton-level perturbative QCD, the parton distribution functions of the proton, the underlying event (describing the possibility of multiple parton interactions in the same proton–proton collision), initial- and final-state radiation, the definition of jets, and the minimum bias event properties.

Figure 53 (taken from Ref. [23]) illustrates the structure of a proton–proton collision event as it occurs in the LHC. Hard subprocesses between partons need to be convolved with parton densities, the decays of the hard subprocesses, initial- and final-state radiation, and multiple parton interactions (and their initial- and final-state radiation), as well as beam remnants and other outgoing partons (not shown) to arrive at a realistic description. All parton-level processes are connected through colour confinement, leading to a primary hadronisation, with many primary hadrons being unstable and further decaying.

To reconstruct such an event in ATLAS or CMS it first needs to be triggered, i.e., the event must pass several trigger levels with increasing rejection power. Once accepted, the event is written to disk and promptly reconstructed on large offline computer farms comprising several thousand central processing units. The reconstruction program reconstructs tracks of charged particles in the inner tracker and the muon systems, electromagnetic clusters in the electromagnetic calorimeter, hadronic clusters and jets in the combined electromagnetic and hadronic calorimeters, missing transverse energy in the calorimeters, and identifies particles and objects: muons, electrons, photons, taus, jets, and heavy quark flavour. All these steps in the reconstruction chain involve tremendous challenges regarding efficiency, purity, accu-

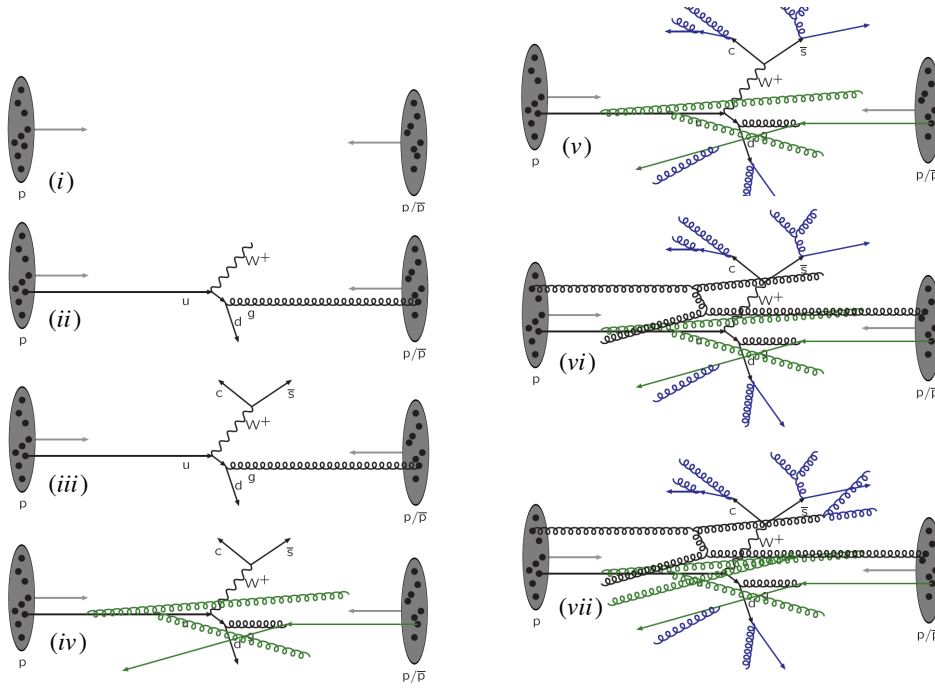


**Fig. 53:** Schematic Feynman graphs for proton–proton collisions corresponding to: (i) incoming proton beams: parton distributions; (ii) hard subprocess: described by matrix elements; (iii) resonance decays: correlated with hard subprocess; (iv) initial-state radiation: spacelike parton showers; (v) final-state radiation: timelike parton showers; (vi) multiple parton–parton interactions; (vii) multiple parton–parton interactions with its initial- and final-state radiation. Pictures and legend taken from Ref. [23].

racy and resolution (calibration). The extensive commissioning work performed by the experiments will surely pay off when analysing the first collision data and comparing them with Monte Carlo simulations.

With increasing statistics data-driven analysis and calibration methods will take over and the experiments will achieve the performance they have been designed for.

After the reconstruction of the primary physics objects, the events are selected according to topological criteria that characterise the physics channel of interest. *Inclusive analyses* count events with leptons, photons, jets or missing transverse energy. For example, a QCD analysis may select events with high-energetic (or many) jets. A combined QCD and electroweak analysis may select events with leptons or photons in the final state. A search for supersymmetry with  $R$ -parity conservation will select events with large missing transverse energy, and may also require leptons to reduce the contamination from Standard Model QCD events. *Exclusive analyses* kinematically combine reconstructed objects. For example, an analysis using  $W \rightarrow \mu\nu$  decays will identify a muon and compute the transverse  $W$  mass using the muon momentum and the transverse missing energy vector. To select top–antitop events, where, for example, one top decays to  $b\ell\nu$  and the other to  $bq\bar{q}$ , one must identify the electron and two  $b$ -jets, and compute the top mass from the invariant mass of one of the  $b$  jets and two hard light-quark jets, which originate from a  $W$  decay. To identify Higgs decays into two photons one must identify two photons in the event and compute their invariant mass, which needs to accumulate at the same value within the experimental errors to create a significant Higgs signal over backgrounds from random two-photon or misidentified photon-jet combinations. Similarly, to search for Higgs decays into two electrons and two muons, one must identify the corresponding leptons and compute their invariant mass. Intermediate on-shell resonances with known mass can be used as additional kinematic constraints. Finally, to search for new high-mass resonances such as Kaluza–Klein graviton states decaying into lepton pairs, as predicted in models with extra spatial dimensions, one must identify the leptons and compute their mass to obtain a signal over the dominant Drell–Yang di-lepton background. For many of these analyses it is beneficial to combine all the available object-level and event-level information using multivariate statistical pattern recognition techniques.

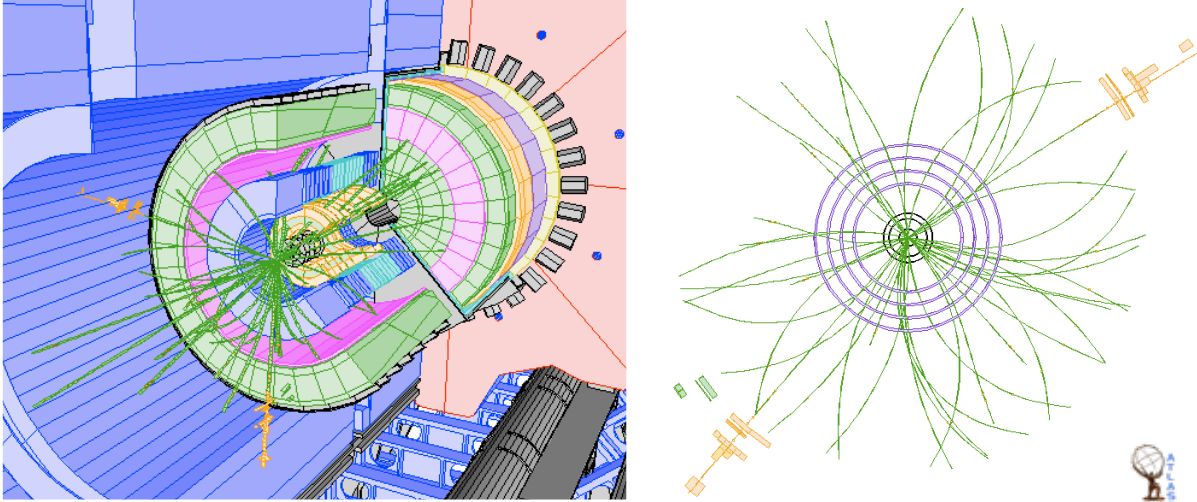


**Fig. 54:** Event display of a simulated  $Z \rightarrow ee$  event in ATLAS. The final-state electrons have tracks in the inner tracker and large energy depositions in the electromagnetic calorimeter. Their invariant mass is consistent with that of a  $Z$  boson.

## 9 Physics commissioning

With emphasis at the beginning of the collision data taking, but also throughout the whole lifetime of the experiments, physics commissioning such as the calibration and alignment of detector systems and physics objects, as well as the data-driven (*‘in-situ’*) measurement of efficiencies, purities, calibration biases and resolutions, will represent a large part of the experimental work. We discuss in the following the *in-situ* calibration of the electromagnetic calorimeter, the determination of material in the inner tracking detector, and jet and missing transverse energy calibration and reconstruction.

### 9.1 *In-situ* electromagnetic calorimeter calibration

Among the primary measurements driving the performance requirements for the ATLAS and CMS electromagnetic calorimeters is the search for  $H \rightarrow \gamma\gamma$ . Since this channel is important at low Higgs mass where the intrinsic width of the Higgs is negligible,<sup>28</sup> the measured width of the di-photon invariant mass, and hence the sensitivity for discovery, will be determined by the energy resolution of the electromagnetic calorimeter. We have already mentioned the importance of the constant term in the calorimeter energy resolution for Higgs searches in Footnote 17. We can extend this by a back-of-the-envelope exercise. Let us consider a data sample for an integrated luminosity of  $20 \text{ fb}^{-1}$  containing 690  $H \rightarrow \gamma\gamma$  and  $\sim 170\,000$  background events with di-photon invariant mass  $110 < m_{\gamma\gamma} < 150 \text{ GeV}$ . With the nominal (design) ATLAS electromagnetic calorimeter resolution, assuming a constant term of 0.7%, a fit to the di-photon mass would yield a signal significance of  $2.9\sigma$ . Worse constant terms of 1.0% or even 2.0% would reduce this significance to  $2.4\sigma$  and  $1.8\sigma$ , respectively.<sup>29</sup>

It is hence mandatory to keep the constant term, originating from non-uniformities in the calorimeter response due to inhomogeneities and non-linearities, as small as possible by *intercalibrating* the calorimeter with physics events. Calorimeter intercalibration (which is *not* absolute scale calibration) can be performed with any physics events that provide a predicted or smooth energy deposition.

The most favourable channel for *in-situ* intercalibration is  $Z \rightarrow ee$ . The  $Z$  mass being precisely

<sup>28</sup>A Higgs of mass 120 GeV has an intrinsic width of 4 MeV, while at 200 GeV the Higgs has a width of 1.4 GeV due mainly to the opening of the di-weak-boson channels.

<sup>29</sup>Note that this test assumes the simplest possible  $H \rightarrow \gamma\gamma$  analysis approach. A more sophisticated fit using more discriminating variables and detector-specific ‘categories’ boosts the fit performance significantly.

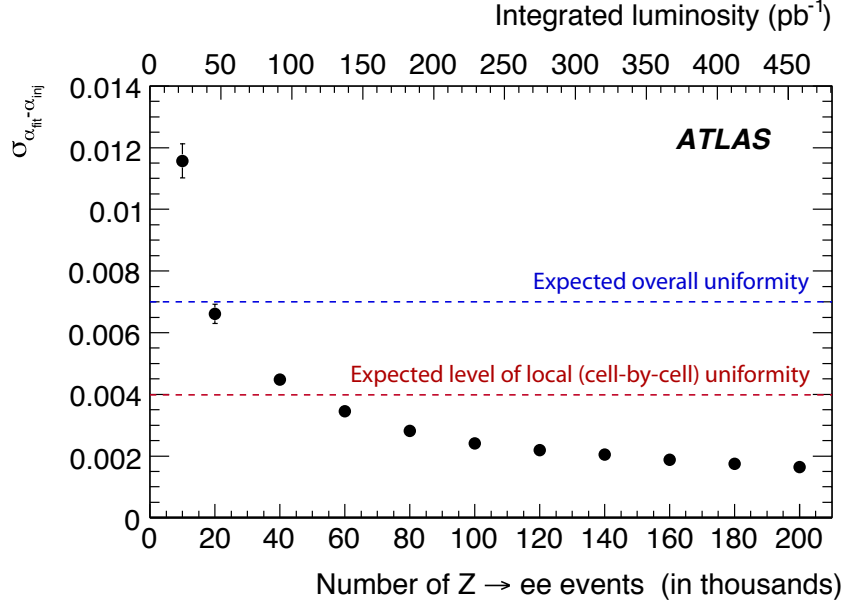


**Fig. 55:** Statistical yield of the  $Z \rightarrow ee$  electromagnetic calorimeter intercalibration in ATLAS. Shown is the expected accuracy achieved for the constant term versus the number of events used in the intercalibration fit. The corresponding integrated luminosity is given on the upper abscissa.

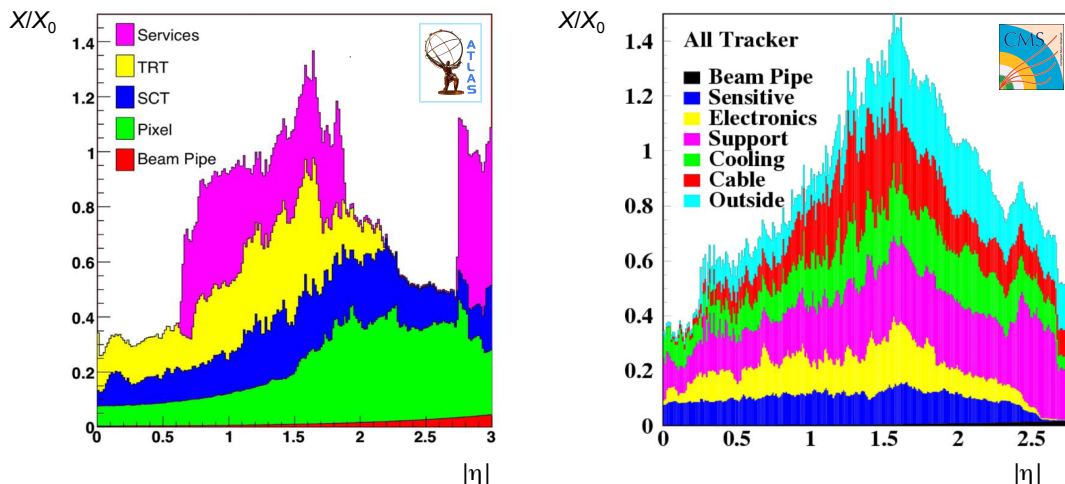
measured at LEP to  $(91.1875 \pm 0.0021)$  GeV, the average reconstructed di-electron mass in the detector after calibration must reproduce it (per event, the detector resolution and the natural width of 2.5 GeV will lead to a natural smearing). With sufficient statistics, the mass-constrained intercalibration can be done per geometrical detector units, which are suitably chosen regions in pseudorapidity and azimuth, typically  $\Delta\eta \times \Delta\phi = 0.2 \times 0.4$ . ( $Z \rightarrow ee$  decays also allow one to calibrate the absolute energy scale, which is required to be known at the per mil level or less for most analyses, and should be at the 0.02% level for the high-precision  $W$  mass measurement.) For a given intercalibration region  $i$ , it is assumed that long-range non-uniformities, encoded in a parameter  $\alpha_i$ , have modified the measured electron energy as  $E_i^{\text{reco}} = E_i^{\text{true}} \cdot (1 + \alpha_i)$ . Neglecting correlations between the electrons and postulating that the opening angle between the two electrons is correctly measured on average, the effect on the di-electron invariant mass is  $M_{ij}^{\text{reco}} = M_{ij}^{\text{true}} (1 + (\alpha_i + \alpha_j)/2)$ . The  $\alpha_i$  can be extracted from a maximum-likelihood fit to  $Z \rightarrow ee$  candidates, which must also incorporate a background component from events other than  $Z \rightarrow ee$ .

Figure 54 shows the event display of a simulated  $Z \rightarrow ee$  event in ATLAS. The electrons leave large energy deposits in the electromagnetic calorimeter and their invariant mass is consistent with that of a  $Z$  boson. Approximately 10 000 of these events (and approximately 10 times more  $W \rightarrow e\nu$ ) will be recorded in  $10 \text{ pb}^{-1}$  integrated luminosity (reconstruction efficiency not subtracted). Figure 55 depicts the expected statistical yield of the  $Z \rightarrow ee$  electromagnetic calorimeter intercalibration in ATLAS. Shown is the expected accuracy achieved for the constant term versus the number of events used in the intercalibration fit. Indicated by the dashed horizontal lines are the design value of 0.7% for the constant term and the level of the local non-uniformity from cell-by-cell variations, estimated to be 0.4%. Design calibration performance is expected to be reached with  $20 \text{ pb}^{-1}$  integrated luminosity.

## 9.2 Inner detector material mapping

The high-precision and redundant inner tracking systems of ATLAS and CMS come at the price of a significant amount of material the particles must traverse. Figure 57 shows the material in the inner tracking system of ATLAS (left) and CMS (right) in terms of radiation lengths. It is remarkable that only a small part of it stems from active detector material, whereas the main contributions are due to services.





**Fig. 57:** Material in the inner tracking system of ATLAS (left) and CMS (right) in terms of numbers of radiation lengths  $X/X_0$ . Solenoid and calorimeter cryostat add roughly  $2X_0$  before the electromagnetic calorimeter presampler in ATLAS.

The amount of radiation lengths in these services needed to be systematically reevaluated throughout the planning and construction phases of both detectors. While the technical proposals in 1994 estimated about (in units of  $X_0$ ) 0.2 (0.6) at  $\eta = 0$  ( $\eta = 1.7$  corresponding to about  $20^\circ$  polar angle) for both ATLAS and CMS, it became 0.2 (1.5 for ATLAS and 0.85 for CMS) at the time of the TDRs in 1997, to finally converge to 0.3 (1.3 for ATLAS and 1.5 for CMS) at the time of the construction in 2006. Note that in ATLAS objects need to traverse approximately an additional  $2X_0$  before reaching the presampler (available for  $|\eta| < 1.8$ ), and roughly another  $X_0$  before the electromagnetic calorimeter.

A good understanding and simulation of the inner detector material is crucial for precision measurements such as the  $W$  mass, where the accurate calibration at the  $Z$  mass needs to be transferred to the  $W$  mass using Monte Carlo simulation. Many other physics analyses benefit from a precise material mapping. The best method to perform a radiography of the inner tracking detector is to use photon-to-electron-positron-pair conversion, which occurs only in the vicinity of a nucleus that recoils against the  $e^+e^-$  system and thus ensures momentum conservation (*cf.* Fig. 56). The conversion needs to happen not too far from the interaction point so that sufficient tracking layers remain to reconstruct the electron and positron tracks and their common vertex position, which indicates matter. A photon-conversion-based radiography of the ATLAS inner tracking detector, obtained from Monte Carlo simulation, which implements a detailed modelling of the active and passive components, is shown in Fig. 58. The photons originate from  $\pi^0$  and  $\eta$  decays, and Monte Carlo truth information has been used for the conversion vertices (the measured conversion map will look quite different).

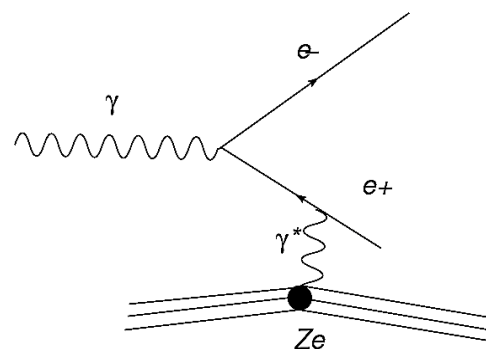


**Fig. 56:** Feynman diagram for the conversion of a photon to an electron-positron pair in presence of a nucleus.

### 9.3 Efficiency determination with the tag-and-probe method

Decays of  $Z$  bosons to leptons can also be exploited to measure trigger selection and offline reconstruction efficiencies from data. The primary method used for this is denoted ‘tag-and-probe method’, the



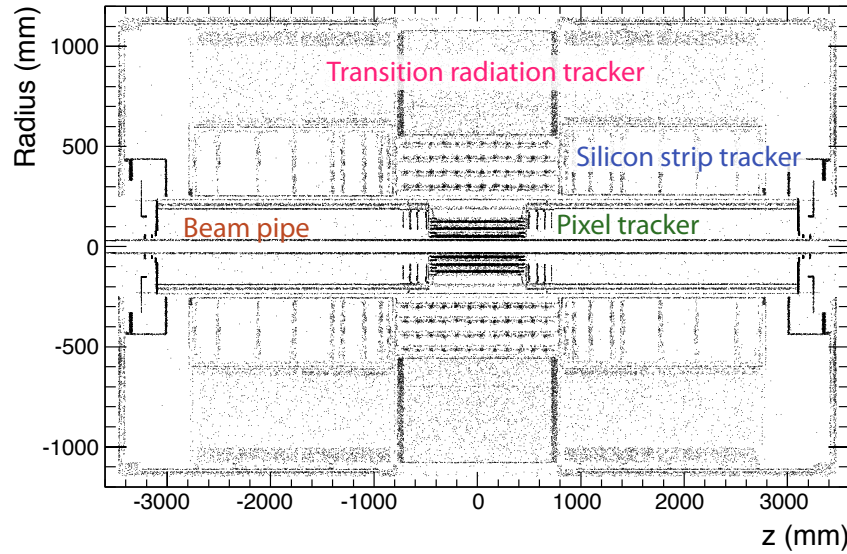


**Fig. 58:** Mapping of photon to electron–positron conversions as a function of  $z$  and radius, integrated over the azimuth angle, for the ATLAS inner tracking detector. The mapping has been made from 500 000 simulated minimum bias events ( $\sim 40$  minutes of data taking at 200 Hz output rate), using  $\sim 90\,000$  conversion electrons of transverse momentum larger than  $0.5\,\text{GeV}$ , originating from photons from  $\pi^0$  and  $\eta$  decays. Monte Carlo truth information is used for the conversion vertices. The plot shown does not represent the latest version of the ATLAS detector description. In particular the beam condition monitor stations located at  $z = \pm 1840\,\text{mm}$  are not yet included.

principle of which is straightforward (see sketch in Fig. 59). Let us consider the example of determining the reconstruction efficiency of muons in the muon system using  $Z \rightarrow \mu\mu$  candidate events.<sup>30</sup>

The candidate event has been triggered by the ‘tag muon’, which is a ‘golden’ muon candidate with an isolated track from combined inner tracker and muon system reconstruction, and transverse momentum larger than  $20\,\text{GeV}$ . The probe muon is another muon candidate, which is independent of the tag-muon selection. To find the candidate we require a track reconstructed in the inner tracker and an invariant mass of tag and probe muons consistent with that of a  $Z$  boson. We now count how often the probe muon has been reconstructed in the muon spectrometer. With sufficient statistics the efficiency of the probe muon reconstruction can be evaluated in bins of  $p_T$ ,  $\eta$  and  $\phi$ . Usually, the result has to be corrected for combinatorial background under the  $Z$  peak. The most powerful approach combines background and efficiency determination in all regions within a single unbinned maximum-likelihood fit. The tag-and-probe method is very flexible, and many versions of the same idea exist. Figure 60 shows an event display of a simulated  $Z \rightarrow \mu\mu$  event in ATLAS. The minimum ionising muon tracks traverse the calorimeters and leave measured hits in the muon spectrometer. Approximately 10 000 of these events (and approximately 10 times more  $W \rightarrow \mu\nu$ ) will be recorded in  $10\,\text{pb}^{-1}$  integrated luminosity (reconstruction efficiency not subtracted).

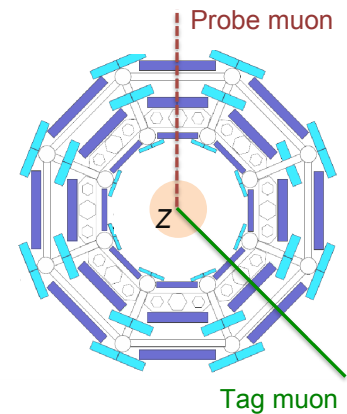


**Fig. 59:** Sketch illustrating the tag-and-probe method.

<sup>30</sup>The expression ‘candidate’ refers to the fact that for real data we do not know whether a reconstructed  $Z \rightarrow \mu\mu$  candidate is indeed the process we believe it to be, or whether it is background from random combinations of muons (‘combinatorial background’) or objects faking muons. Only a statistical analysis allows us to separate signal from irreducible background.

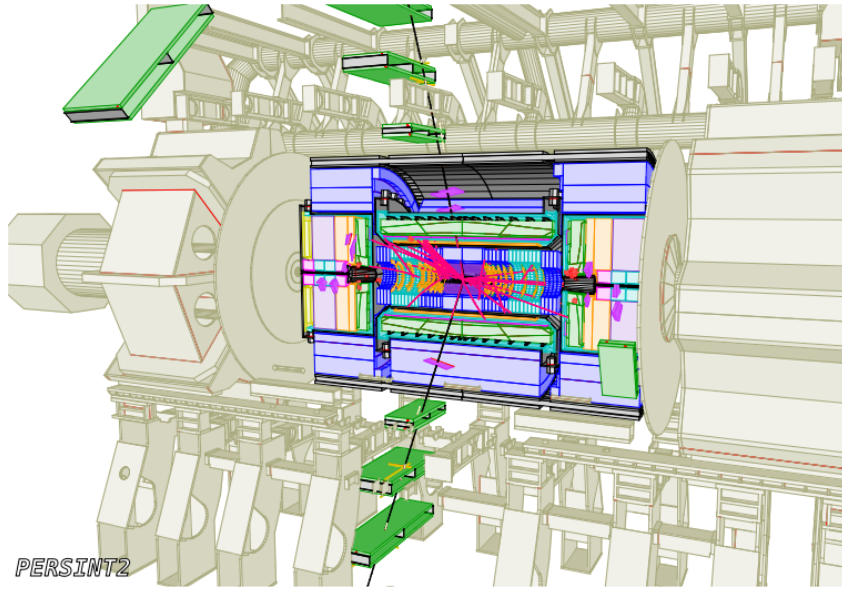


**Fig. 60:** Event display of a simulated  $Z \rightarrow \mu\mu$  event in ATLAS. The final-state muons are measured in the muons spectrometer.

#### 9.4 Jet calibration

A precise knowledge of the absolute jet energy scale (JES) is needed by many physics analyses. Typically a calibration of better than 1% is required for the measurement of the top-quark mass, but also for supersymmetry signatures. Jets are complex phenomenological objects, and their reconstruction involves a large number of corrections and calibrations. Only a brief overview is given here.

The jet energy reconstruction and calibration can be divided in four steps:

1. Calorimeter tower or cluster reconstruction.
2. Jet forming (cone,  $k_t$ , anti- $k_t$  or other ‘jet algorithms’).
3. Jet calibration from calorimeter to the particle scale.
4. Jet calibration from particle to the parton scale.

The discussion here concentrates on jet calibration, assuming jets have been formed by an algorithm with suitable experimental and theoretical properties for the physics measurement under study.

Several and conceptually quite different calibration approaches are considered by the experiments. Monte Carlo based jet calibrations, transforming the electromagnetic energy scale to the hadronic scale, can be distinguished according to the level of detail with which the jet constituents are treated and separately corrected. The ‘global jet calibration’ uses as input clusters that have been properly calibrated at the electromagnetic scale, and which are matched in energy to the Monte Carlo truth particle jet for bins of  $E_T$  and  $\eta$ . This calibration returns the jet energy at the hadronic scale (*cf.* sketch in Fig. 61). On the contrary, the ‘local hadron calibration’ calibrates clusters independently of the jet algorithm by making an assumption on their electromagnetic or non-electromagnetic nature. Jets are then formed out of calibrated clusters, and the jet energy is given at the hadronic scale. Finally, *in-*

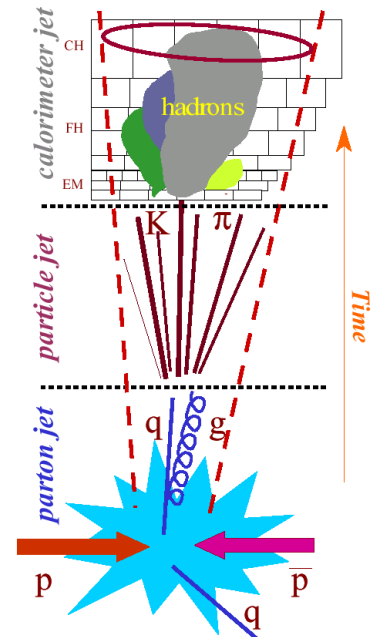


**Fig. 61:** Illustration of the various jet reconstruction levels from partons over hadrons to the calorimeter.

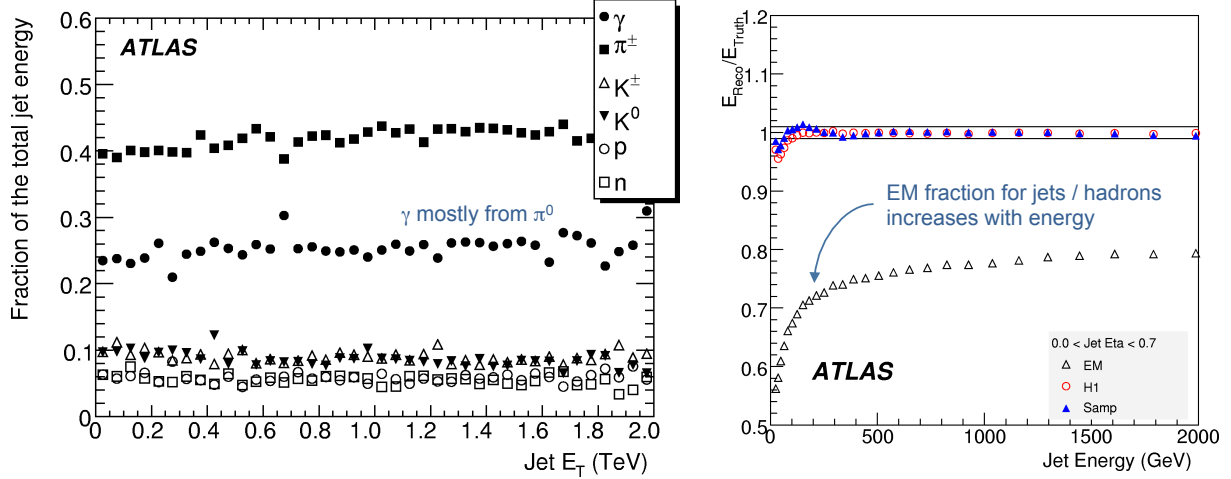


**Fig. 62:** Left: fractional energy carried by different particle types as a function of the jet energy (ATLAS simulation). Right: jet energy linearity as a function of jet energy (ATLAS simulation). Shown are jets reconstructed at the electromagnetic (EM) scale (open triangles), and using global jet calibration algorithms (open circles and full triangles). The jets have a large cone radius of 0.7.

*situ* calibration methods are used to match the hadron to the parton levels of the jet using known physics processes.

A large amount of contributions to the jet signal at the various jet levels must be considered in the calibration process. The parton level is governed by the physics process of interest. At the hadron level (particle jet), one must take into account the jet reconstruction algorithm efficiency, added tracks from in-time event pileup from minimum bias scattering interactions, added tracks from the underlying event, and lost soft tracks due to the magnetic field. At the calorimeter jet level one must account for longitudinal energy leakage, detector signal inefficiencies (e.g., dead channels, dead HV boards) background from pileup events, electronic noise, the definition of the calorimeter signal (cluster algorithm, noise suppression, etc.), dead material losses (front material, geometrical cracks in the active material, transition regions, etc.), the detector response characteristics ( $e/h \neq 1$ ), and the jet reconstruction algorithm efficiency. The left panel of Fig. 62 shows the fractional energy that is carried by different particle types in a jet as a function of the jet energy. The largest contributors are charged pions, followed by photons originating mostly from  $\pi^0$  decays, so that the total pion component amounts to roughly 70% of the jet energy, with no significant jet energy dependence. The right plot shows the jet energy linearity and the electromagnetic fraction versus the jet energy. The electromagnetic fraction for jets or hadrons increases with the jet energy, asymptotically reaching 80% for very hard jets. After calibration, the energy response is accurate above 300 GeV, whereas softer jets are more difficult to calibrate due to the stronger impact of calorimeter noise fluctuations and other effects.

The ultimate goal of the jet reconstruction is to match the calibrated hadronic scale to the initial parton momentum with the use of physics events, i.e., to perform *in-situ* calibration. Several approaches exist.

- Directly verify the hadronic energy scale with **isolated prompt hadrons** from minimum bias events, or hadrons from  $\tau$  decays, by comparing the reconstructed hadron energy with the momentum of the hadron track measured in the inner tracker. Another possibility is to use track balancing in  $\phi$  (energy and momentum conservation of proton–proton collisions requires the event to be transversely balanced, but not longitudinally) to intercalibrate the hadronic scale with respect to different hadron energies.
- Use **transversely balanced  $\gamma$ -jet or  $Z(\rightarrow \ell\ell)$ -jet events**. This method assumes that electromag-

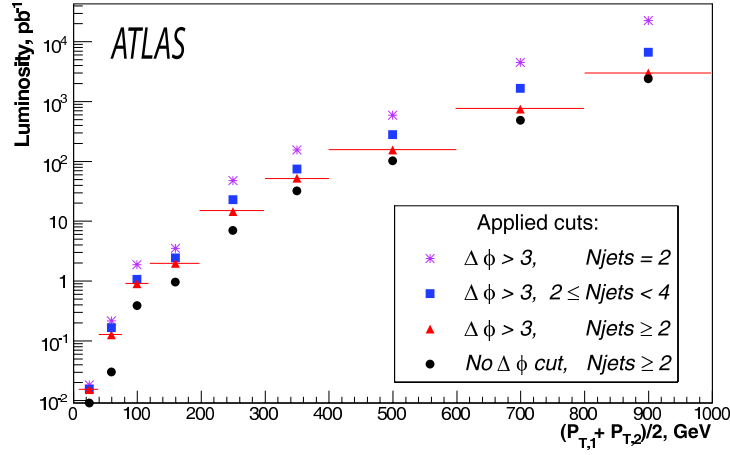


**Fig. 64:** Integrated luminosity required to reach 0.5% precision on the jet energy scale with the multi-jet calibration method for various  $p_T$  ranges in the region  $0.7 < \eta < 0.8$ , and with different sets of selection cuts (ATLAS simulation): all Pythia di-jet events (circles), requiring  $\Delta\phi > 3$  rad between the two leading jets (triangles), requiring in addition fewer than four reconstructed jets in an event (squares), and requiring exactly two reconstructed jets (stars).

netic objects have been properly calibrated beforehand. The jet energy calibration is performed with respect to the average transverse momentum of photon (or  $Z$ ) and jet. Owing to the large cross section of 180 nb for  $\gamma$ -jet processes<sup>31</sup> this method can be applied with initial data. The statistical yield corresponding to an integrated luminosity of  $10\text{ pb}^{-1}$  would allow a jet calibration of better than 1% statistical precision for  $p_T < 200$  GeV. However, the determination of systematic uncertainties is tricky, and requires careful studies. For example, initial- and final-state radiation, underlying events and in-time event pileup, but also out-of-jet particles have the potential to contribute to the  $\gamma$ -jet imbalance, and these effects must be disentangled from miscalibration. Monte Carlo studies by ATLAS have shown that systematic imbalances of non-calibration origin contribute at the 10% level for 20 GeV jets, whereas the effect is below 1% for jets above 100 GeV.

- Use **QCD di-jet and multi-jet events** for  $\Delta\eta \times \Delta\phi$  intercalibration. Di-jet events cannot constrain the absolute jet energy scale, but allow one to intercalibrate the calorimeter response. In case of more than two jets in the event, the leading jet dominates the energy resolution of the event, so that one may assume that the error in the vector sum of the ‘soft’ jets is negligible with respect to the hard jet, and hence ‘calibrate’  $E_T$  versus  $\eta$  and  $\phi$  (*cf.* sketch in Fig. 63). This method benefits from huge statistics (the di-jet cross section exceeds by a factor 100 to 5000 the  $\gamma$ -jet cross section), but sizable systematic effects arise from soft jets, in particular for the multi-jet approach, requiring detailed studies. Figure 64 shows the integrated luminosity required to reach a precision in the jet energy scale of 0.5% with the multi-jet calibration method for various  $p_T$  ranges in the region  $0.7 < \eta < 0.8$  and for different sets of selection cuts (see figure caption). Requiring the jets to be back-to-back (i.e., applying a tight  $\Delta\phi$  cut) reduces systematic effects from initial- and final-state radiation and the underlying event. The figure has been obtained by ATLAS with the use of simulated events.
- Absolute jet energy scale calibration is possible by means of  **$W$  decays into a pair of jets**, for clean  $W$  from top decays. However, this calibration applies to soft jets only (jet energies below

<sup>31</sup>The leading parton level processes contributing to the  $\gamma$ -jet cross section are  $t$ -channel quark–quark scattering via fermion exchange into  $g + \gamma$ , and quark–gluon scattering via fermion exchange into  $q + \gamma$ , gluon–gluon scattering via a box diagram into  $g + \gamma$ , and the  $s$ -channel quark–gluon-to-quark annihilation into  $q + \gamma$ .

200 GeV). In addition, the  $W$  boson does not carry colour charge, which makes it differ from QCD jets.

The LHC will explore energies that have never been reached before. Above 500 GeV, neither measurements nor test beam results are available for jet calibration. Multi-jet balancing should allow a few per cent jet energy scale accuracy in that range with  $1 \text{ fb}^{-1}$  integrated luminosity.

### 9.5 Missing transverse energy reconstruction

A precise reconstruction of missing transverse energy (MET) in terms of energy scale, linearity, and resolution is essential for the ATLAS and CMS physics programme. Large MET is predicted in many new physics scenarios, notably in supersymmetric extensions of the Standard Model respecting  $R$ -parity, where a stable weakly interacting neutral particle is produced that — just as neutrinos — escapes the detector without measurable interaction with the active material. Figure 65 shows a simulated SUSY candidate event in CMS that exhibits significant MET of 360 GeV. MET is also an ingredient of precision Standard Model measurements, such as semileptonic top reconstruction and the  $W$  mass, and also of the search for  $H \rightarrow \tau\tau$  decays, the cross section of which may or may not be enhanced by beyond Standard Model contributions. The MET measurement is particularly sensitive to systematic effects in the detector response and the reconstruction. Understanding MET in early data is therefore one of the primary physics commissioning challenges.

The conceptually simplest way to reconstruct MET is to compute the transverse vector sum of all the electromagnetic and hadronic calorimeter cells and to correct for unaccounted contributions. In the case of ATLAS, one has

$$\cancel{E}_T = \sqrt{\cancel{E}_x^2 + \cancel{E}_y^2}, \quad (5)$$

$$\cancel{E}_{x,y} = \cancel{E}_{x,y}^{\text{Calo}} + \cancel{E}_{x,y}^{\text{Cryo}} + \cancel{E}_{x,y}^{\text{Muon}}, \quad (6)$$

where the symbol  $\cancel{E}$  denotes missing energy. The calorimeter term

$$\cancel{E}_{x,y}^{\text{Calo}} = - \sum_{\text{EM \& Had cells}} E_{x,y}, \quad (7)$$

is calibrated at the hadronic energy scale. The electromagnetic scale would underestimate MET by roughly 30% because the largest contributions to it stem from hadrons and jets.

The ‘cryostat’ term in Eq. (6) corrects for energy loss (leakage) in the cryostats between the electromagnetic and hadronic calorimeters and becomes important for jets with large transverse momentum (representing a 5% contribution per jet with  $p_T > 500 \text{ GeV}$ ). It is given by

$$\cancel{E}_{x,y}^{\text{Cryo}} = - \sum_{\text{Jets}} w^{\text{Cryo}} \cdot E_{x,y}^{\text{Jet-at-cryo}}, \quad (8)$$

where  $w^{\text{Cryo}}$  is a calibration weight determined empirically from Monte Carlo simulation, and  $E_{x,y}^{\text{Jet-at-cryo}}$  is the average of the jet energies deposited in the third layer of the electromagnetic calorimeter and in the first layer of the hadronic calorimeter.

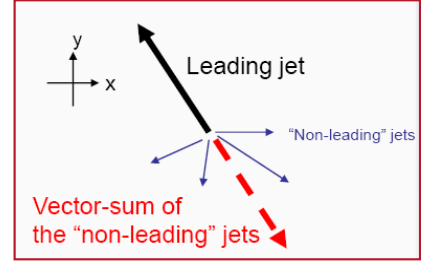


**Fig. 63:** Illustration of multi-jet energy calibration.

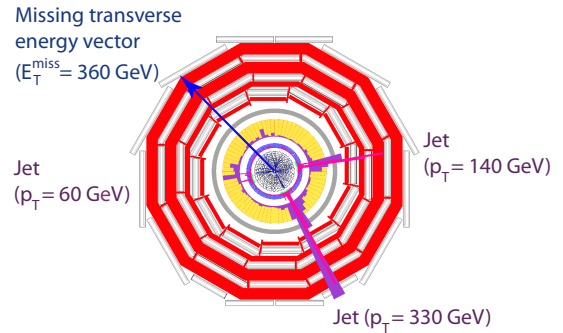


**Fig. 65:** Display of a simulated SUSY event in CMS. The arrow indicates the missing transverse energy vector.



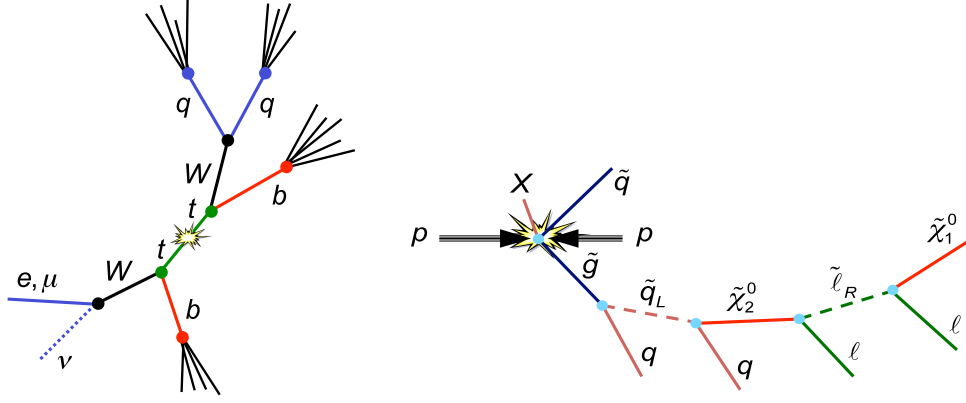


**Fig. 67:** Schematic graphs of processes generating true MET. The left graph corresponds to a  $pp \rightarrow t\bar{t}(+X)$  Standard Model event (only the top part of the event is shown), where one top-quark decays fully hadronically and the other semileptonically. The neutrino generates MET. The right graph depicts a typical decay cascade as obtained in  $R$ -parity conserving supersymmetry. An initial gluino decays into a left-handed squark and a quark (giving a jet), the squark decays into a heavy neutralino and a quark (giving another jet), the heavy neutralino further decays into a slepton and a lepton, and the slepton finally decays into the lightest neutralino, which escapes detection, and a second lepton of opposite charge with respect to the previous lepton. Note that the initial supersymmetric particles are created in pairs, but only one decay cascade is shown here.

Finally, the muon term sums over measured muon momenta within the muon spectrometer acceptance ( $|\eta| < 2.7$ )

$$\cancel{E}_{x,y}^{\text{Muon}} = - \sum_{\text{Muons}} E_{x,y}. \quad (9)$$

The MET reconstruction can be refined by associating reconstructed electrons, photons, muons, hadronically decaying  $\tau$  leptons,  $b$ -jets and light jets to calorimeter cells, and replacing for these cells the global calibration by one that takes into account the nature of the identified objects.

It is apparent from the above equations that all detector systems contribute to the MET measurement, which makes it vulnerable to hardware, reconstruction, and calibration problems. One distinguishes between ‘true’ and ‘fake’ MET. For example, weakly interacting neutral particles generate true MET (*cf.* Fig. 67). Even without systematic effects, MET is created by the detector response resolution, giving rise to fake MET. Fake MET can also be introduced by detector problems or misreconstruction, such as dead and noisy channels, particles falling out of the detector acceptance (e.g., muons for  $|\eta| > 2.7$ ), unaccounted pile-up contributions to resolution effects, backgrounds from beams or cosmic rays, ‘punch-through’ of hadron showers into the muon system faking a muon signal, and many more effects.

The suppression and — if not possible — proper simulation of fake MET is crucial to increase the sensitivity to the true MET. This requires the best possible jet energy resolution and absolute scale, and a thorough classification through data quality bookkeeping and the simulation of varying detector problems. Figure 66 shows an extreme case of MET distortions due to detector noise and bad channel effects,

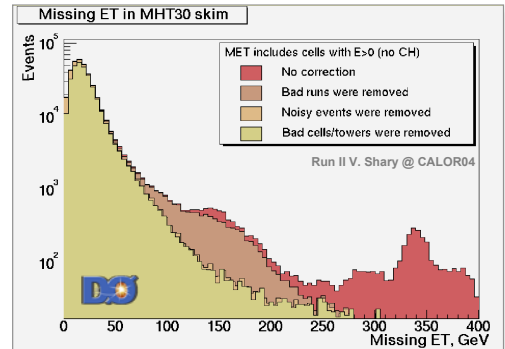


**Fig. 66:** Missing transverse energy distribution measured by the D0 experiment at the Tevatron  $p\bar{p}$  collider. Shown are the various correction stages leading to the removal of fake MET tails that could be misinterpreted as new physics.



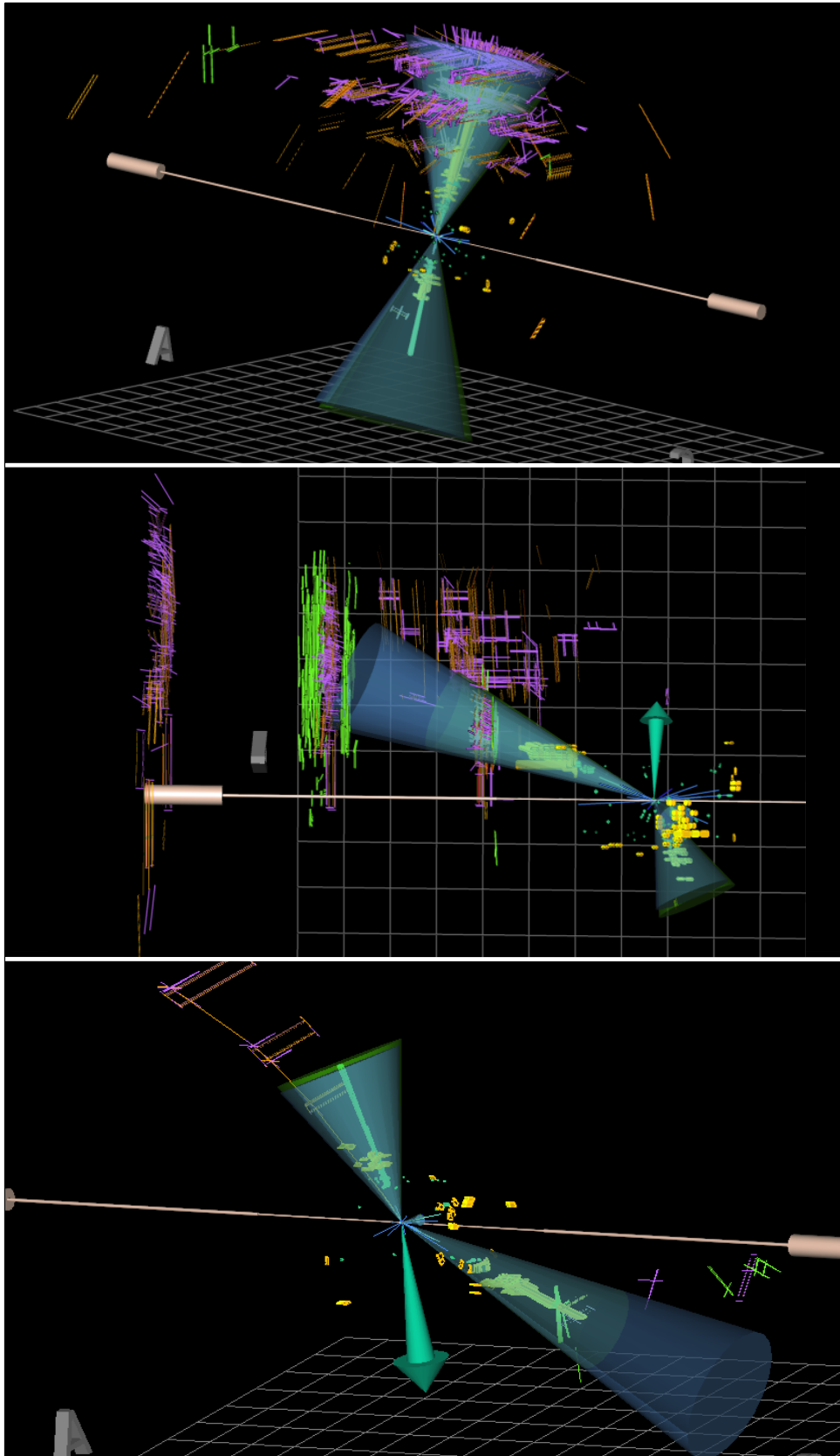


**Fig. 68:** ATLAS event displays of simulated rare di-jet events creating large amounts of fake MET (represented by the round arrow). The upper two displays show hadron punch-through from the calorimeter into the muon spectrometer. The lower display shows large MET found in an event populating the jet energy resolution tails.

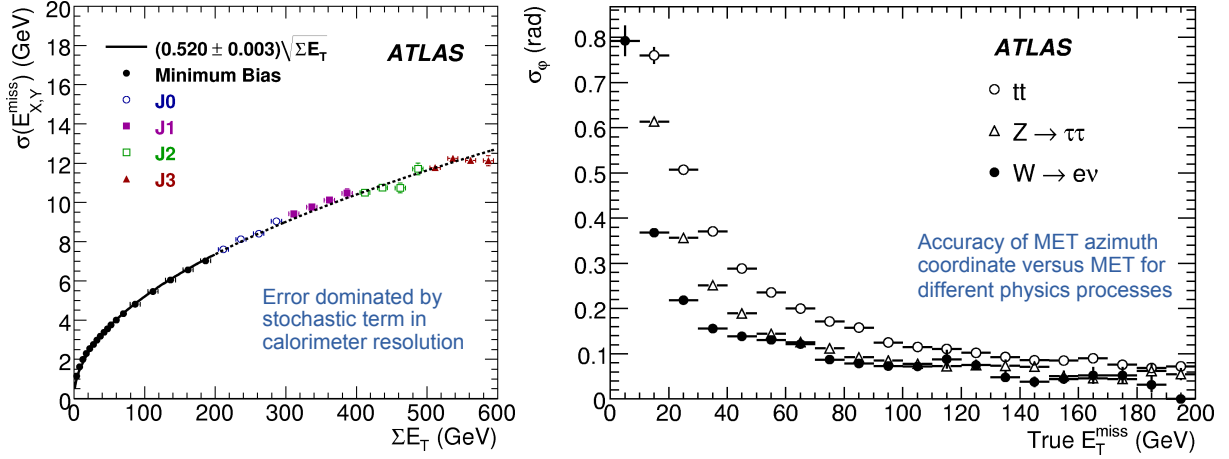


**Fig. 69:** *Left:* expected MET resolution for ATLAS versus the transverse energy sum for minimum bias events and various jet samples. *Right:* accuracy of the MET azimuth angle versus MET for  $t\bar{t}$ ,  $Z \rightarrow \tau\tau$  and  $W \rightarrow e\nu$  events, obtained from Monte Carlo simulation in ATLAS.

provided for illustration purposes by the D0 experiment. The effects lead to large tails that — if not properly corrected or simulated — could be misinterpreted as a new physics signal. Figure 67 depicts schematically two processes that generate true MET. The left one is a Standard Model  $t\bar{t}$  event where one of the tops decays semileptonically, and the right one is a supersymmetric event with its typical decay cascades ending with two invisible lightest stable supersymmetric particles (only one of two decay cascades is shown). Figure 68 shows event displays from simulated events in ATLAS that were selected for featuring pathologically large fake MET due to hadron punch-through (upper two displays) and jet mismeasurement (lower display). Both types of fake MET usually point towards a jet, which allows such backgrounds to be reduced by eliminating events where the MET vector lies on a jet axis.

Fake MET tails can be studied with early data using minimum bias events. Ample statistics will be available thanks to the large minimum bias cross section,<sup>32</sup> allowing the experiments to select clean data samples. Because the expected true MET is negligible ( $\sim 0.06$  GeV) the measured MET will be dominated by fake effects from single hadron and jet energy resolution (82%), and acceptance (18%). ATLAS expects an MET average value of 4.3 GeV. The left panel in Fig. 69 shows the expected MET resolution for ATLAS versus the measured transverse energy sum for minimum bias events and various jet samples providing increasing transverse energies. The resolution is dominated by the stochastic term in the jet energy resolution, giving a square-root dependence on the transverse energy sum with the expected coefficient of approximately 50% (see Section 5).

True MET in early data can be measured in leptonic  $W$  decays, which have good statistics, but also in  $Z \rightarrow \tau\tau$  events. In case of one  $\tau$  decaying semileptonically (hadron(s) plus neutrino) and the other leptonically (electron or muon plus two neutrinos), one can reconstruct the  $\tau$  mass by assuming that the  $\tau$  decay products were emitted collinear with the  $\tau$  flight direction in the lab frame. This is a useful conjecture since the  $\tau$  exhibits a strong boost. With this one finds

$$m_{\tau\tau}^2 \approx 2 \cdot (E_h + E_{\nu(h)}) (E_\ell + E_{\nu(\ell)}) (1 - \cos\theta_{h\ell}), \quad (10)$$

where the neutrino energies are approximated by MET. Simulated  $Z \rightarrow \tau\tau$  decays in ATLAS showed that this method allows the  $Z$  mass to be reconstructed with an average resolution of 12 GeV. The right panel of Fig. 69 gives the expected accuracy of the MET azimuth angle versus the true MET for  $t\bar{t}$ ,  $Z \rightarrow \tau\tau$

<sup>32</sup>At 14 TeV centre-of-mass energy, a minimum bias event rate of 70 kHz is expected to be produced at  $10^{30} \text{ cm}^{-2}\text{s}^{-1}$  peak luminosity, and owing to the logarithmic  $\sqrt{s}$  dependence similar orders of magnitude are expected at lower centre-of-mass energy. For example, at 900 GeV the minimum bias cross section is reduced by a factor of only 1.8 with respect to 14 TeV.

and  $W \rightarrow e\nu$  events simulated by ATLAS. With larger true MET the signal-to-calorimeter-noise ratio increases and hence the quality of the MET reconstruction. Moreover, the more hadronic activity in the detector, the worse the MET reconstruction.

## 10 Early physics with ATLAS and CMS

Early physics measurements will be performed while the detectors are still being commissioned. Some of the commissioning tasks will thus have to take priority to allow systematic uncertainties to be evaluated. An example is the determination of the absolute tracking efficiency, which is an important ingredient of first QCD measurements such as the average number of produced tracks per pseudorapidity region, and which depends on basic detector properties such as the hit efficiency, the alignment of the inner tracking systems, and low-transverse-momentum track finding. Likewise, any physics measurement requires the determination of at least the relative trigger efficiency, and in case of cross section measurements also the absolute trigger efficiency as well as the integrated luminosity. The latter quantity requires either an absolute luminosity detector or, more importantly at the beginning of data taking, an LHC beam scan ('Van der Meer scan'<sup>33</sup> [24]).

The following paragraphs present a very brief and incomplete overview of initial measurements that will be performed at ATLAS and CMS after the collection of approximately  $100\text{pb}^{-1}$  integrated luminosity. Most of the prospective studies shown here are taken from ATLAS [3]. The CMS studies, documented in Ref. [4], are very similar. All results shown are based on Monte Carlo simulation at 14 TeV centre-of-mass energy. This is, however, not the energy at which the LHC will start. Because of problems with the magnet quench protection, the startup centre-of-mass energy in 2010 will be 7 TeV, after a pilot run at LHC injection energy of 0.9 TeV in 2009. The decision whether or not to raise the energy to 10 TeV in the course of the year 2010 will depend on the running experience. The design energy of 14 TeV can only be reached after a shutdown of approximately one year, which may be scheduled in 2011 or 2012, when vulnerable parts of the quench protection system are exchanged.

### 10.1 Minimum bias studies

Minimum bias events will dominate the first triggered data samples of all LHC experiments. The total minimum bias cross section receives contributions from inelastic non-diffractive and diffractive collisions,<sup>34</sup> where whether or not single diffractive events are included is subject to the experiment's definition. Experimentally, it is not possible to distinguish these classes of events on an event-by-event basis. Minimum bias triggers have usually large (medium, small) efficiencies for non-diffractive (double diffractive, single diffractive) events. If coincident hits in both forward regions of the detector are required, the efficiency of single diffractive events becomes small. In-time coincidence is a useful requirement to eliminate beam related backgrounds (beam gas and beam halo events, *cf.* Section 7.2). These backgrounds are, however, also eliminated when requiring the reconstructed tracks in the event to form a primary vertex. The minimum bias analysis will most likely be the first paper published by ALICE, ATLAS and CMS. Apart from the physics measurement, it will represent a first proof that the detectors (mainly the inner tracking systems) work and the data including the trigger and tracking efficiencies are understood.

Multiparticle production is successfully described by phenomenological models with pomeron

<sup>33</sup>The beam scan is used to measure the beam sizes and positions in a collider, which, together with the known currents, can be used to compute the absolute luminosity. The beams are scanned across each other at the collision point and, using beam position measurements, the amount of motion is correlated with detectors monitoring the relative luminosity of the collisions at each scan point. This method has been successfully applied at the heavy-ion collider RHIC [25].

<sup>34</sup>Diffractive denotes the excitation of the proton(s) participating in the inelastic scattering. One distinguishes single, double and central diffraction. While single and double diffractive events produce activity in only one and both forward regions of the detector, respectively, central diffractive events, (which are described by double pomeron exchange, and have small cross sections), give activity at small pseudorapidities.

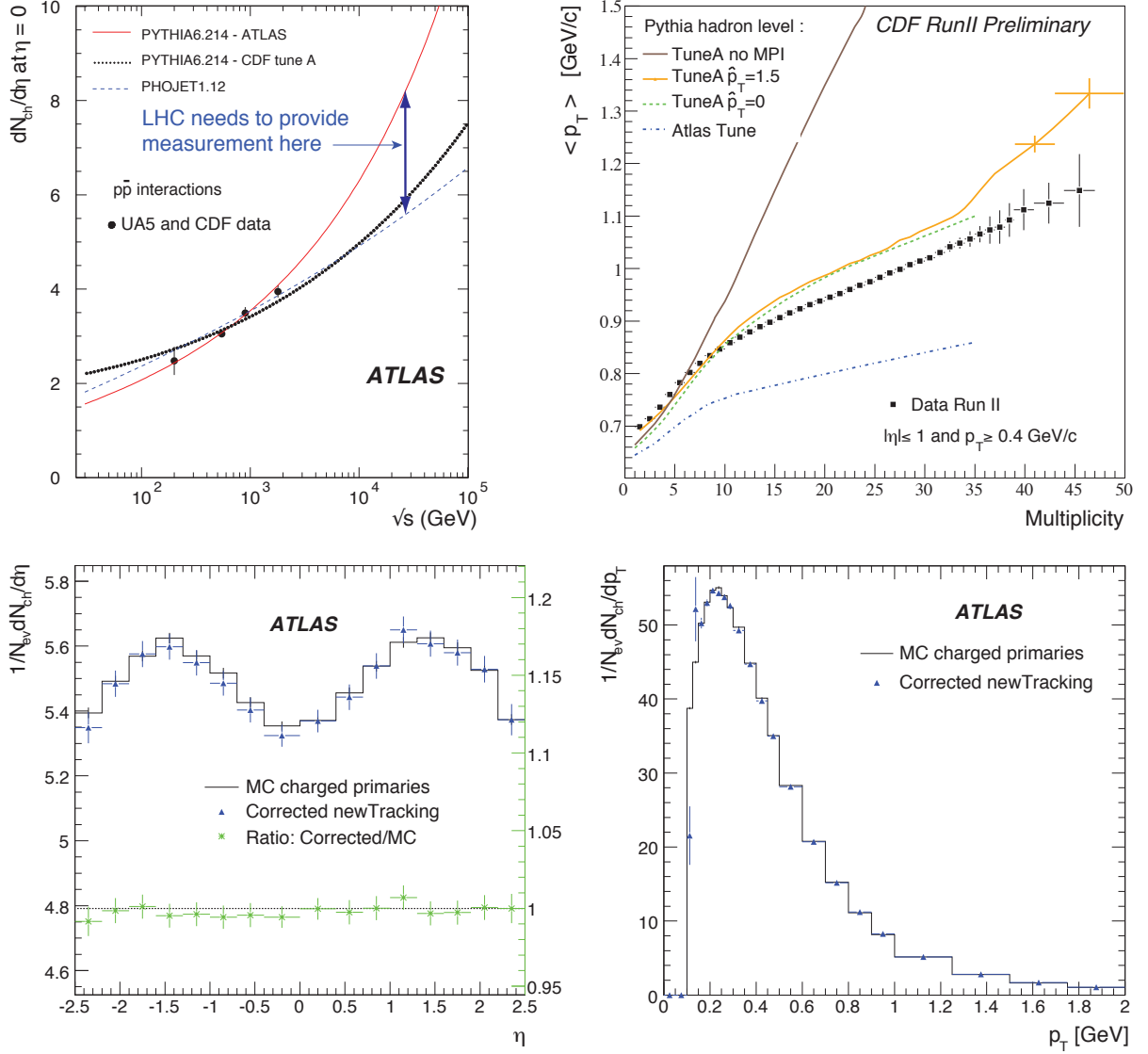


**Fig. 70:** Top left: central charged particle density for non-single diffractive inelastic events in  $p\bar{p}$  collisions as a function of energy, extrapolated to large centre-of-mass energies. Shown are available measurements and Monte Carlo generator predictions. Top right: correlation between average track transverse momentum and the charged particle multiplicity for  $\eta < 1$  as measured by CDF [26], and compared with various Pythia generator tunings. ‘No MPI’ means that multiple parton interactions have been switched off in the generator. Bottom plots: particle density in non-diffractive minimum bias events versus the pseudorapidity (left) and  $p_T$  (right) in ATLAS with special low-momentum track reconstruction enabled. Systematic errors on track reconstruction are not included in the right plot.

exchange, which dominates at high energies. These models relate the energy dependence of the total cross section to that of the multiplicity production using a small number of parameters, and are the basis for several Monte Carlo event generators describing soft hadron collisions. Minimum bias multiplicity measurements between 200 GeV and 2 TeV centre-of-mass energies at the CERN ISR, CERN Sp $\bar{p}$ S, Fermilab’s Tevatron, and BNL’s RHIC colliders have been used to tune these generators for predictions of multiplicities at LHC energies.

The top left panel in Fig. 70 shows a comparison of model predictions for the central charged particle density in non-single-diffractive  $p\bar{p}$  events for a wide range of centre-of-mass energies compared

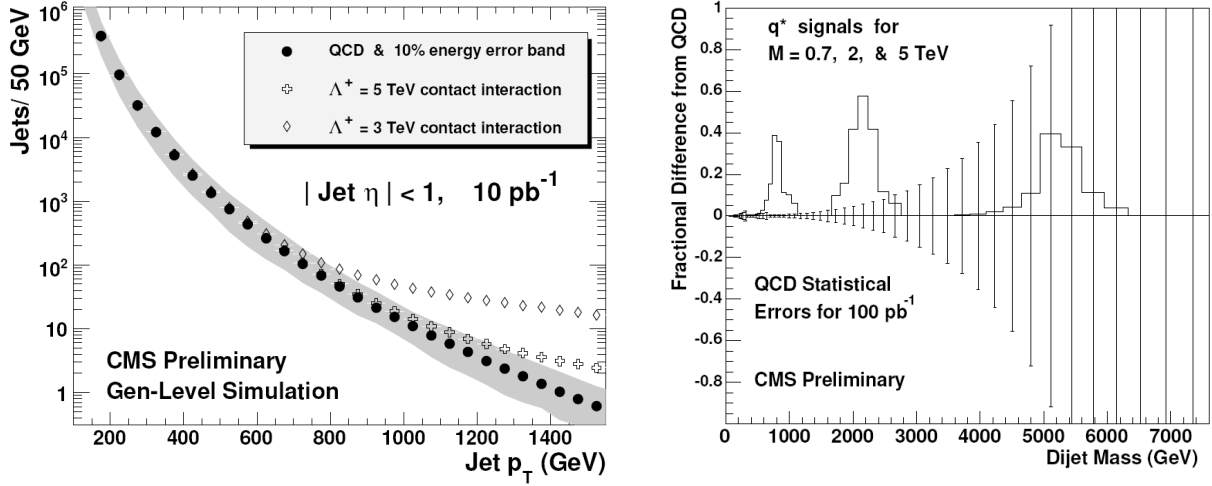


**Fig. 71:** Left: distribution of the transverse momentum of the hardest central jet in simulated di-jet events for  $10\text{pb}^{-1}$  integrated luminosity (CMS study). The shaded band indicates the systematic uncertainties. The cross and diamond curves indicate the distortions in the high- $p_T$  spectrum expected from contact interactions at the scales  $\Lambda^+ = 3\text{ TeV}$  and  $5\text{ TeV}$ , respectively. Right: fractional difference from the QCD expectation of the di-jet invariant mass (CMS). Also shown are the contributions to the difference from heavy excited quarks decaying into jet pairs.

with measurements that have been corrected for detector acceptance. Large extrapolation uncertainties exist that must be overcome by LHC measurements. Improved generator tunings at LHC energies will directly feed into Monte Carlo predictions of many primary physics channels. A good minimum bias multiplicity description is also important because event pileup from minimum bias interactions is background to hard scattering processes at high luminosity. The top right panel in Fig. 70 is taken from CDF [26]. It shows the measured dependence of the average track transverse momentum on the charged particle multiplicity per event for  $|\eta| < 1$ , compared with various Pythia generator tunings. Without multiple parton interactions the average predicted  $p_T$  multiplicities above 6 is grossly overestimated. The bottom plots in Fig. 70 show the particle density versus pseudorapidity (left) and transverse momentum (right) in ATLAS for simulated minimum bias events. Special low- $p_T$  tracking reconstruction has been enabled for these plots, which allows one to lower the track measurement down to  $p_T = 150\text{ MeV}$  (standard cut is  $500\text{ MeV}$ ), at the price of larger systematic uncertainties (not included in the error bars). The statistics shown corresponds to 1 minute of data taking with  $10^{31}\text{ cm}^{-2}\text{s}^{-1}$  at  $14\text{ TeV}$ .

## 10.2 Di-jet studies

Jet production has a roughly 1000 times lower cross section than non-diffractive minimum bias scattering, but is still an abundant process for early physics measurements and performance studies. Apart from its importance for QCD studies and Monte Carlo generator tuning at yet unexplored centre-of-mass energies, jet production can be used to probe the Standard Model. Inclusive di-jet production ( $pp \rightarrow 2\text{ jets} + X$ ) is the dominant LHC hard scattering process. It is straightforward to observe and has a rich potential of new physics signatures. Restricting the leading jet (the jet with the largest  $p_T$ ) to the central detector region  $|\eta| < 1$  reduces the background from QCD  $t$ -channel processes, thus enhancing the sensitivity to new physics contributions to the  $s$ -channel at small pseudorapidities. The main variables used for new physics searches are the transverse momentum of the leading jet and the di-jet invariant mass. Prospective studies from CMS show that the highest di-jet masses reached with integrated luminosities of  $100\text{pb}^{-1}$ ,  $1\text{fb}^{-1}$ , and  $10\text{fb}^{-1}$  are respectively 5, 6 and 7 TeV. The current limits from measurements by the Tevatron experiments will be almost immediately extended by ATLAS and CMS.

The left panel in Fig. 71 shows the distribution of the leading central-rapidity jet  $p_T$  in simulated

di-jet events as expected by CMS for an integrated luminosity of  $10\text{pb}^{-1}$ . The shaded band indicates the estimated systematic uncertainties. Also shown are the distortions in the spectrum expected from contact interactions<sup>35</sup> at the characteristic scales  $\Lambda^+ = 3\text{ TeV}$  and  $5\text{ TeV}$ , respectively. A quantitative sensitivity study shows that contact interactions up to  $\Lambda = 3\text{ TeV}$  can be discovered with the first  $10\text{pb}^{-1}$ . However, the analysis requires excellent understanding of the jet resolution in the tails and the jet energy scale. Systematic errors dominate over the statistical ones and over uncertainties from the parton density functions.

The right plot in Fig. 71 shows a Monte Carlo study by CMS of a search for strongly produced heavy excited quarks decaying into a quark pair. The most sensitive observable here is the di-jet invariant mass. Shown in the plot is the fractional difference between measurement (here: simulation) and Standard Model expectation for  $100\text{pb}^{-1}$  integrated luminosity. Shown by the resonances are the contributions from excited quarks to that difference, which can be clearly separated below  $3\text{ TeV}$ . Other variables can also be looked at. For example, the ratio of di-jet abundances between different regions of pseudorapidity versus the di-jet invariant mass benefits from reduced systematic uncertainties compared with absolute cross section measurements. Also angular distributions exhibit sensitivity to new physics.

### 10.3 Quarkonia production

Quarkonia ( $q\bar{q}$  resonances such as  $J/\psi$ ,  $\psi'$ ,  $\Upsilon$ ,  $\Upsilon'$ , etc.) are abundantly produced at the LHC (see the Feynman graphs in Fig. 72) and excellent sources for early physics commissioning, but also for early physics measurements, e.g., prompt versus non-prompt production distinguished via different lifetimes, ratios of cross sections, polarisation, etc. Examples of Feynman diagrams for the singlet and octet production of a  $J/\psi$  resonance are drawn in Fig. 72. The upper diagram describes the leading colour-singlet process, which has a small cross section. The middle diagram, which dominates at low  $p_T$ , can be produced through both singlet and octet  $c\bar{c}$  states with various quantum numbers. At high  $p_T$ , the gluon fragmentation subprocess shown in the lower plot becomes increasingly important.

Quarkonia in ATLAS and CMS are mainly studied through their decays into muon and also electron pairs. Since they are narrow resonances they can be used as commissioning tools for the alignment and calibration of the trigger, tracking, and muon systems. Efficiency studies can employ the ‘tag-and-probe method’ (see Section 9.3). Owing to the low mass of the resonances, trigger considerations are crucial to estimate the available cross section for analysis. Using a di-muon trigger with  $4\text{ GeV}$  thresholds for each muon, the overall rate of events from all quarkonium states is likely to remain below the rate of  $1\text{ Hz}$  at a luminosity of  $10^{31}\text{ cm}^{-2}\text{s}^{-1}$ . (The trigger rates may be dominated by background processes.)

The left-hand plot in Fig. 73 shows the cumulative differential cross section of the invariant di-muon invariant mass for  $J/\psi$  and  $\Upsilon(1S)$  signal events and various combinatorial backgrounds from an ATLAS Monte Carlo study. The plot includes trigger requirements of at least one muon with  $6\text{ GeV}$  and

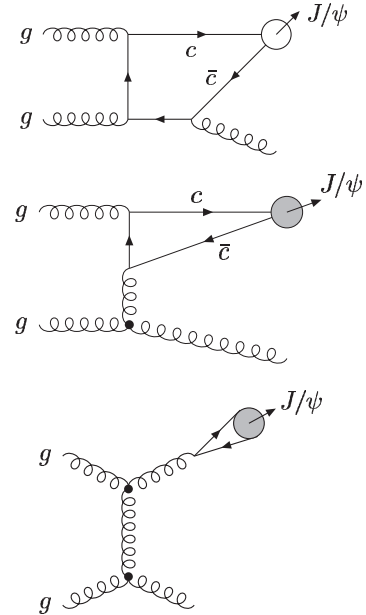


**Fig. 72:** Examples of Feynman diagrams for the singlet and octet production of a  $J/\psi$  resonance (see text).

<sup>35</sup>New physics models with fermion substructure (‘compositeness’) at high scale lead to excitations of these fermions which modify scattering cross sections. The interaction can be parametrised by an effective four-fermion contact term

$$\mathcal{L}_{\text{eff}} = \frac{4\pi^2}{\Lambda^2} \sum_{i,k=L,R} \alpha^{ik} (\bar{q}_i \gamma^\mu q'_i) (\bar{f}_k \gamma^\mu f'_k), \quad (11)$$

where  $\Lambda$  is the mass scale of the new interaction. Experimental limits exclude excited fermions up to a few  $\text{TeV}$ .



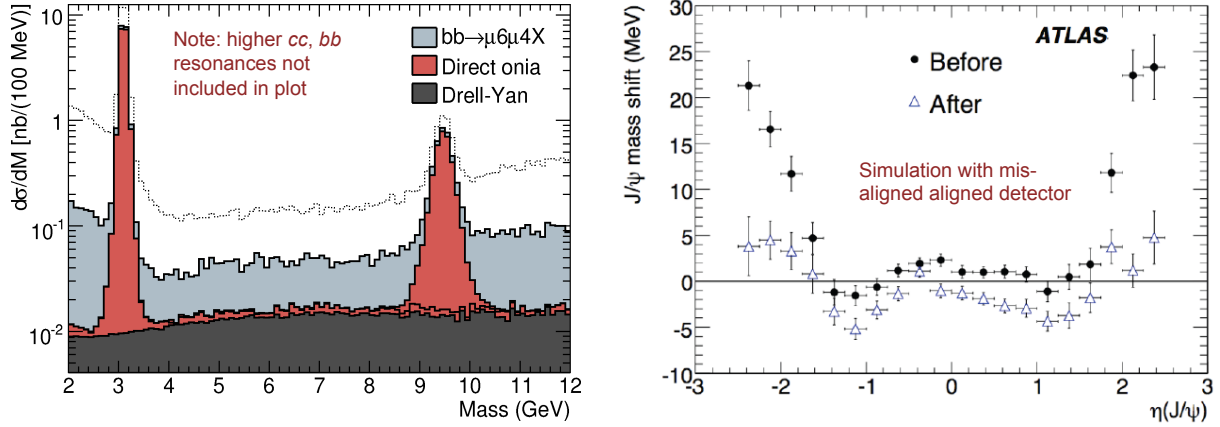


**Fig. 73:** Left: cumulative differential cross section versus the invariant mass of muon pairs from various quarkonia signal and combinatorial background sources (ATLAS study). A primary vertex and pseudo-proper time requirement of 0.2 ps has been applied. The dotted line shows the cumulative distribution without these cuts. The quarkonia simulation used for the plot does not include higher radial excitations. Right: invariant mass of di-muons from  $J/\psi$  decays versus the  $J/\psi$  pseudorapidity for simulated ATLAS data where a severe misalignment of the inner tracking system has been introduced. Shown are results before and after alignment.

another one with 4 GeV transverse momentum, and that these muons must originate from a common primary vertex. In addition a lifetime requirement has been applied. (The dotted line shows the cumulative distributions without these latter two requirements). Backgrounds from Drell–Yan processes and leptonic heavy-quark decays are of similar size.

The right panel of Fig. 73 shows a simulated commissioning result from ATLAS. Events of the type  $pp \rightarrow J/\psi(\rightarrow \mu\mu) + X$  with (somewhat unrealistically) severe misalignment in the inner tracker have been simulated and run through the alignment procedure based on hits-on-track residual minimisation. As discussed in Section 6.2, this method suffers from so-called weak modes, which denote misalignments that leave the global  $\chi^2$  function, used to minimise the hit residuals, invariant. As seen in the plot, the reconstructed invariant di-muon mass versus the pseudorapidity of the di-muon system exhibits a strong non-uniformity before the alignment, but remaining effects caused by weak modes after the alignment.

#### 10.4 W and Z boson production

Inclusive production of W and Z bosons ( $pp \rightarrow W(Z) + X$ ) has large cross sections so that interesting data-driven cross section measurements can be performed with early data ( $10\text{--}50\text{pb}^{-1}$ ). The weak bosons are also important ingredients for commissioning studies: Z bosons are most important for various *in-situ* calibrations (*cf.* Section 9), and Z+jets and W+jets are sensitive probes of higher order QCD calculations. Inclusive weak boson production is also precisely predicted by theory so that a cross section measurement in particular of the more abundant W production can be used to infer the absolute integrated luminosity recorded.

Figure 74 shows the distribution of the W transverse mass for  $W \rightarrow e\nu$  (left) and  $W \rightarrow \mu\nu$  (right) decays together with their dominant backgrounds for simulated data corresponding to  $50\text{pb}^{-1}$  integrated luminosity (ATLAS study). The transverse mass is defined by

$$m_T = \sqrt{E_T^\ell \cancel{E}_T (1 - \cos\Delta\phi)}, \quad (12)$$

where  $\Delta\phi$  is the angle between the transverse lepton and missing energy vectors, and  $E_T^\ell$  is the transverse energy of the lepton. The transverse W mass is also used as an ingredient for the precision measurement

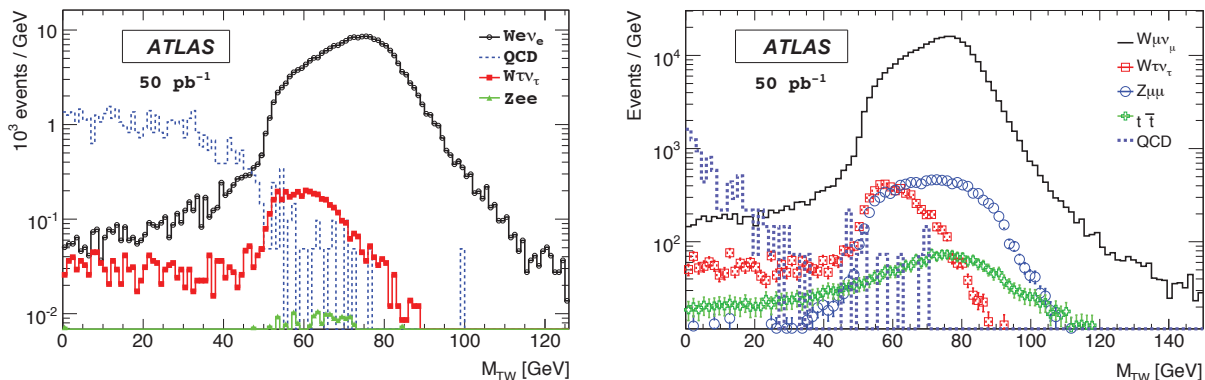


**Fig. 74:**  $W$ -boson transverse mass distribution for  $W \rightarrow e\nu$  (left) and  $W \rightarrow \mu\nu$  (right) and backgrounds after full selection except for the  $M_T$  cut, for simulated data corresponding to an integrated luminosity of  $50\text{ pb}^{-1}$ .

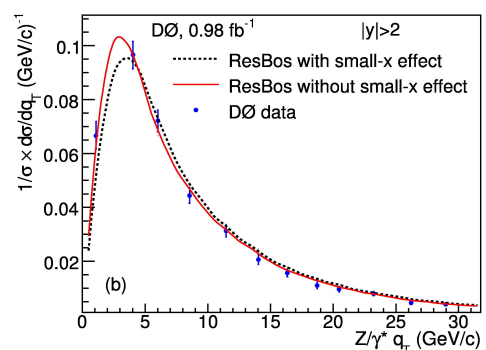
of the  $W$  mass, which, however, requires much larger data samples for a competitive measurement, because of the required mass calibration with respect to the accurately known  $Z$  boson, which has a ten times smaller leptonic cross section.

Figure 75 shows the  $Z$ -boson transverse momentum distribution as measured by D0 at the Tevatron for a centre-of-mass energy of 1.96 TeV. It is compared with Monte Carlo generator models including next-to-leading order QCD calculations. Good control of the transverse momentum of weak bosons is important for many physics studies. Specifically in multivariate Higgs searches, the Higgs transverse momentum can be used as a discriminating variable since Higgs production is expected to have a harder spectrum than QCD backgrounds.

### 10.5 Top-quark production

The roughly 100 times larger  $t\bar{t}$  production cross section of  $\sim 830\text{ pb}$  at the LHC (at 14 TeV centre-of-mass energy) compared with  $\sim 7.5\text{ pb}$  at the Tevatron, makes it possible to observe top quarks in early data. Also the electroweak single-top production cross section of  $\sim 300\text{ pb}$  is similarly enlarged. Apart from having important physics potential, top quarks represent excellent objects for data-driven commissioning and calibration analyses, notably  $b$ -tagging and jet energy scale fits. The leading processes contributing to  $t\bar{t}$  production are gluon–gluon scattering ( $s$  and  $t$ -channels) and quark–antiquark annihilation ( $s$ -channel). Single-top production is dominated by  $W$ –gluon fusion ( $t$ -channel),  $W$  exchange between  $b$  quarks ( $t$ -channel), associated production of top and  $W$ , and quark–antiquark annihilation ( $s$ -channel, smaller cross section).

Data corresponding to an integrated luminosity of  $100\text{ pb}^{-1}$  should allow the experiments to measure the  $t\bar{t}$  production cross section, with events where both  $W$  bosons decay leptonically, to an accuracy of 3% statistical and 5% systematic error (dominated by the uncertainty in the integrated luminosity value). The measurement provides an important probe of the validity of the Standard Model at unexplored centre-of-mass energy. Figure 76 shows on the right panel the reconstructed hadronic top mass from a combination of three jets as found in a simulated signal and background sample corresponding to  $100\text{ pb}^{-1}$  integrated luminosity after full event selection. The left panel shows the corresponding di-jet mass formed by light-flavour jets, representing the  $W$  signal and combinatorial background. This plot



**Fig. 75:**  $Z$ -boson transverse momentum distribution, measured by the D0 experiment at the Tevatron, compared with Monte Carlo generator models.

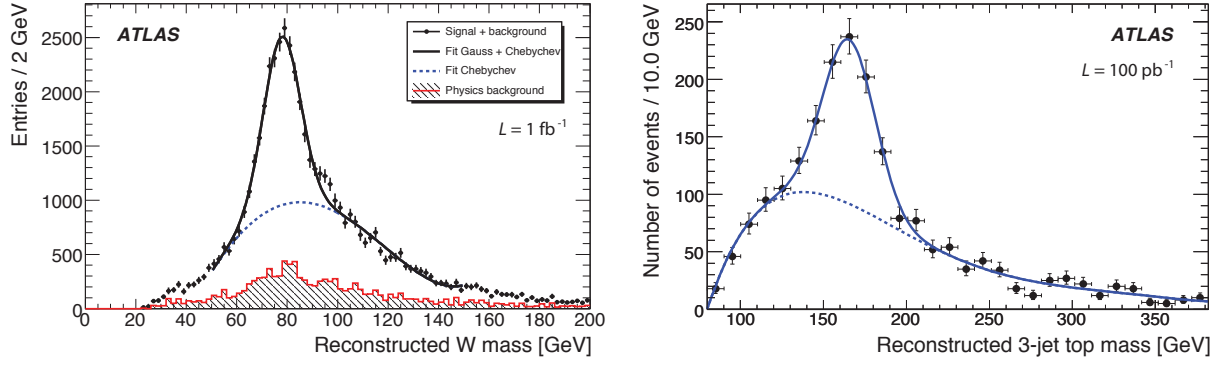


**Fig. 76:** Left: distribution of the invariant di-jet mass of light-flavoured jets as an estimate of the hadronically decaying  $W$ -boson mass in a simulated data sample corresponding to  $1 \text{ fb}^{-1}$  integrated luminosity for signal  $t\bar{t}$  and background processes (ATLAS study). Right: reconstructed hadronic top mass from the combination of three jets in simulated data corresponding to  $100 \text{ pb}^{-1}$  integrated luminosity signal  $t\bar{t}$  and background events after full selection.

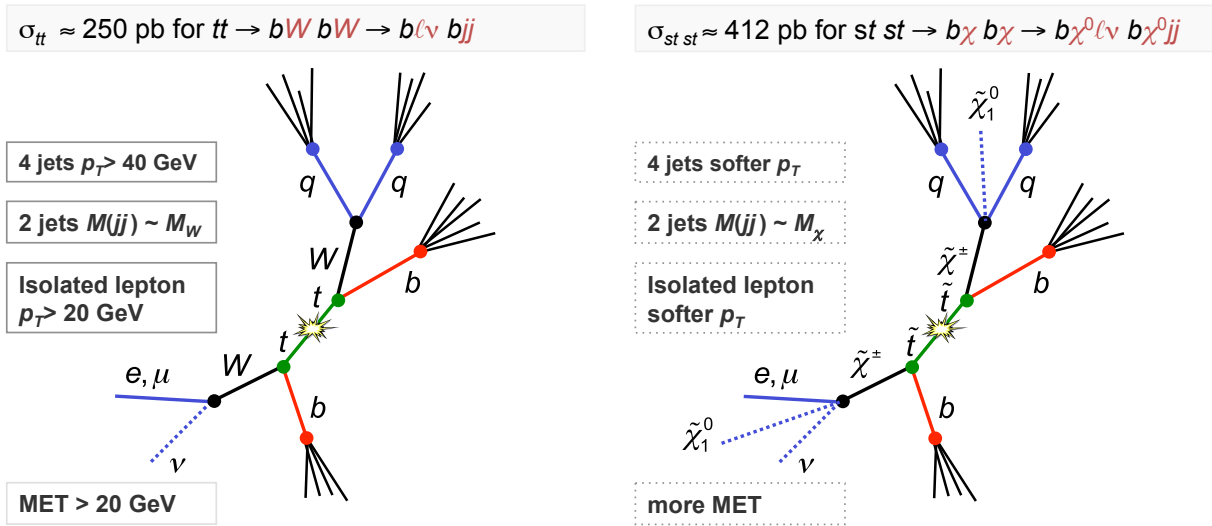


**Fig. 77:** Left: schematic graph of a  $pp \rightarrow t\bar{t}(+X)$  process where one top decays fully hadronically and the other semileptonically. The neutrino generates missing transverse energy. Right: schematic graph of a supersymmetric stop–antistop production. The  $W^\pm$  propagators in top–antitop production are replaced by charginos that decay into three bodies of which one (the neutralino) is a stable weak interacting neutral particle.

can be used to determine and adjust the jet energy scale. A kinematic fit to the true  $W$  mass can be used to improve the accuracy of the three-jet top-mass reconstruction.

Single-top production is of particular interest due to its sensitivity to charged new physics fields, such as a charged Higgs replacing the  $W$  in the weak propagator as occurs in two-Higgs-doublet models. Single-top production has been observed by the Tevatron in 2009 with the use of advanced multivariate analysis techniques [27]. The measured cross section of  $(2.3^{+0.6}_{-0.5}) \text{ pb}$  (CDF),  $(3.94 \pm 0.88) \text{ pb}$  (D0), is in agreement with the Standard Model expectation.

Figure 77 shows on the left diagram a schematic drawing of a Standard Model top–antitop event, where one top decays fully hadronically and the other semileptonically. The right diagram shows the production and decay of a light supersymmetric ( $R$ -parity conserving) stop–antistop pair, which follows a similar decay cascade with, however, an additional weak interacting neutral particle in the final state

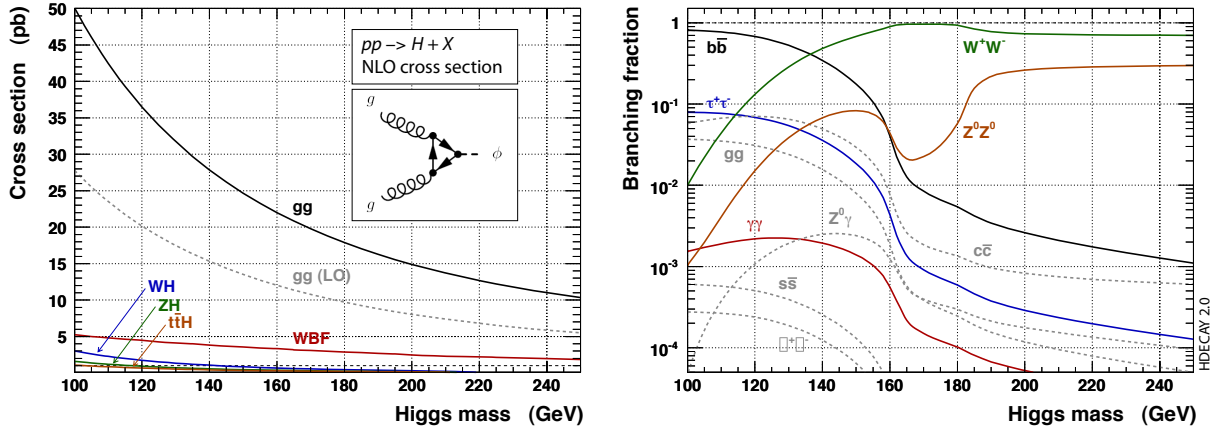


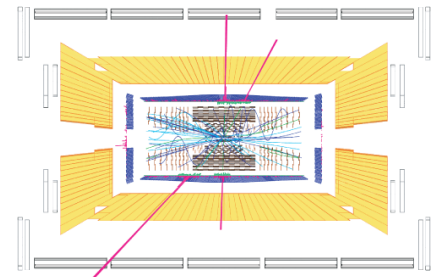
**Fig. 79:** Expected inclusive Standard Model Higgs boson production cross section for the various production modes (left) and Higgs branching fractions (right) versus the Higgs mass at 14 TeV centre-of-mass proton–proton collisions.

that escapes the detector. As a consequence, the four particle jets and the isolated lepton are softer than in the  $t\bar{t}$  case, the two light jets originating from the heavy neutralino decay form the invariant mass of a neutralino, instead of that of a  $W$ , and significantly more missing transverse energy is produced in the supersymmetric event. The experimental separation of the  $t\bar{t}$  and  $t\bar{t}\tilde{t}$  processes is difficult and requires more statistics than available in early data taking. The analysis requires  $b$ -flavour tagging to be commissioned and proceeds by plotting the minimum three-particles invariant mass that can be formed of a  $b$ -jet and the two light-flavoured jets. Subtracting from it the expected  $t\bar{t}$  Standard Model contribution a  $t\bar{t}\tilde{t}$  contamination would show up by a peak below the top (and below the stop mass, due to the escaped neutralino). A study performed by ATLAS shows that with  $1.8\text{fb}^{-1}$  and a stop mass of 137 GeV, for which the  $t\bar{t}\tilde{t}b\chi b\chi \rightarrow (b\chi^0\ell\nu)(b\chi^0qq)$  cross section amounts to 412 pb (depending also on other model parameters), exceeding by a factor 1.6 the corresponding  $t\bar{t} \rightarrow bWbW \rightarrow (b\ell\nu)(bqq)$  cross section, a clear signal can be derived.

## 10.6 Standard Model Higgs boson search

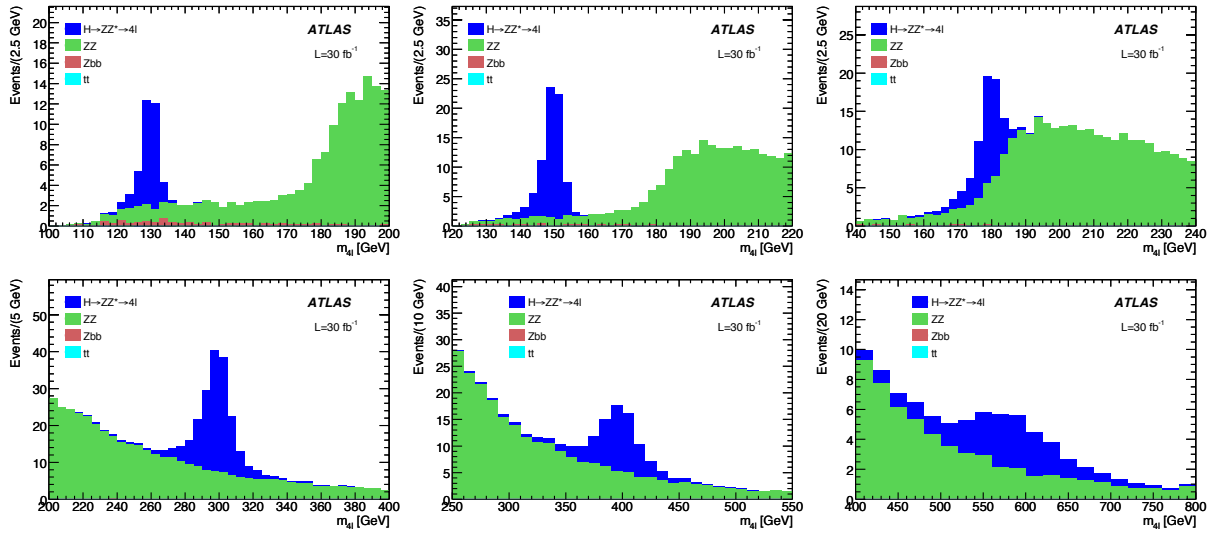
The observation of a Standard Model Higgs boson is inverse femtobarn rather than picobarn physics, and hence not of primary importance for early physics. However, new physics may enhance Higgs-like signals and the experiments must be prepared for surprises. It is also important to begin early with the understanding and improvement of electron muon, tau and photon selection efficiencies and purities, and the study of  $b$ -jet and forward-jets tagging, and a thorough categorisation of the relevant Higgs backgrounds to tune the multivariate analyses that will be used to extract a signal.

Figure 79 shows the dependence of the inclusive Standard Model Higgs boson production cross section and branching fractions on the Higgs mass. The dominant production mode is the fusion of two gluons into a scalar Higgs via triangular top loop. Next-to-leading order (NLO) corrections give a sizable  $K$ -factor (the factor with which the leading order result needs to be multiplied to include higher orders) in this process. The second most important process is weak boson fusion that is accompanied by two forward jets. Since it is a weak process, next-to-leading order corrections are less important. Following are the associated Higgs production with a  $W$  or a  $Z$  boson, or with a  $t\bar{t}$  pair. The strong rise in the branching fractions to the heavy weak boson pairs is



**Fig. 78:** A simulated  $H \rightarrow ZZ^* \rightarrow 4e$  event with  $m_H = 150\text{ GeV}$  in CMS.

due to the kinematic opening of these channels, which are favoured because the Higgs couples to the masses of the particles (if the Higgs boson were heavy enough to be able to decay into a top–antitop pair (not shown in the plot), it would reach a branching fraction of up to 20% at around  $m_H \sim 500$  GeV).



**Fig. 80:** Reconstruction of the four-lepton invariant mass for simulated  $H \rightarrow ZZ^{(*)} \rightarrow 4\ell$  ( $\ell = e, \mu$ ) signal and background events corresponding to an integrated luminosity of  $30\text{fb}^{-1}$  (ATLAS study). From upper left to lower right are shown analyses for the true Higgs masses 130, 150, 180, 300, 400, and 600 GeV, respectively.

Figure 80 illustrates the results of a simulated search for  $H \rightarrow ZZ^{(*)} \rightarrow 4\ell$  in ATLAS with  $30\text{fb}^{-1}$  for different true Higgs masses. Because the Higgs partial width into two vector bosons increases with  $m_H^3$ , but only linearly for a Higgs decaying into two fermions,<sup>36</sup> the total Higgs width grows fast beyond the  $H \rightarrow WW$  and  $H \rightarrow ZZ$  openings. For example, while the Standard Model Higgs width is only 3.6 MeV at  $m_H = 120$  GeV and 76 MeV at 160 GeV, it grows to 1.4 GeV at 200 GeV and 8.5 GeV at 300 GeV. In the region favoured by the electroweak fit (see below) the Higgs intrinsic width is much smaller than the experimental resolution and hence negligible.

Electroweak precision observables, measured by experiments at the LEP (CERN), SLC (SLAC) and Tevatron (FNAL) accelerators, can be used in a global Standard Model fit to derive a constraint on the Higgs mass. The resulting  $\Delta\chi^2$  curves versus the Higgs boson mass, without and with results from direct Higgs boson searches at LEP and the Tevatron included in the fit, are given in Fig. 81. The result including all the available information yields the allowed range  $114 < m_H < 157$  GeV at 95% confidence level. Although this represents an important indication, experimentalists cannot afford to disregard the high-mass region. The analyses must cover all Higgs masses that are not yet excluded by direct searches.

<sup>36</sup>The leading order width of the Higgs boson decay into a fermion–antifermion pair is given by

$$\Gamma^{(\text{LO})}(H \rightarrow f\bar{f}) = \frac{G_F N_C}{4\sqrt{2}\pi} m_H m_f^2 \beta_f^3, \quad (13)$$

where  $G_F = 1.16637 \cdot 10^{-5} \text{ GeV}^{-2}$  is the Fermi constant,  $\beta_f = \sqrt{1 - 4m_f^2/m_H^2}$  is the fermion velocity in the Higgs rest system, and  $N_C = 3(1)$  is the number of colours for quarks (leptons). Large next-to-leading order corrections can occur in the case of quarks. The leading order width of the decay into two on-shell weakly interacting vector bosons reads

$$\Gamma(H \rightarrow VV) = \frac{G_F m_H^3}{16\sqrt{2}\pi} \cdot \delta_V \cdot A(x), \quad (14)$$

where  $\delta_V = 2(1)$  for  $V = W(Z)$ , and  $A(x) = \sqrt{1 - 4x} \cdot (1 - 4x + 12x^2)$  with  $x = m_V^2/m_H^2$ . For masses much larger than  $2m_Z$  the width  $\Gamma(H \rightarrow WW)$  is twice as large as  $\Gamma(H \rightarrow ZZ)$ . Very roughly one finds  $\Gamma(H \rightarrow WW + ZZ) \approx 0.5 \text{ TeV} \cdot (m_H/1 \text{ TeV})^3$ , so that for a Higgs mass of 1 TeV the Higgs width becomes of the same order of magnitude.

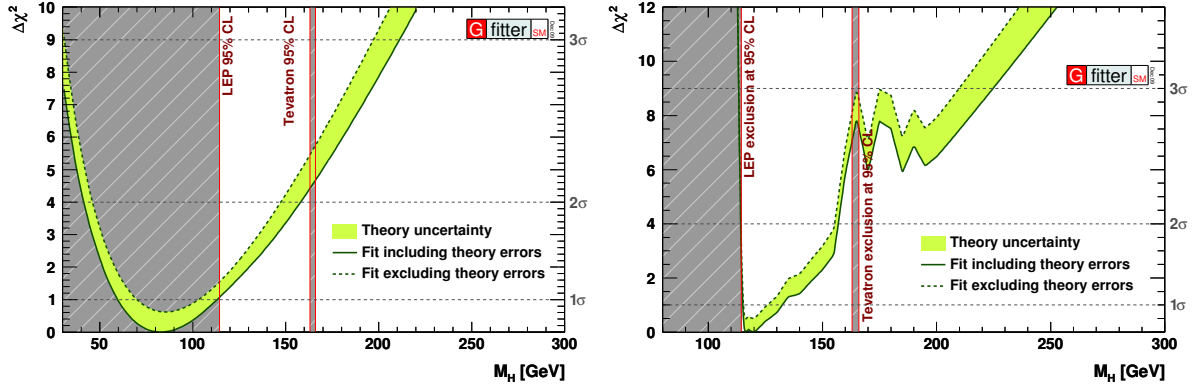


**Fig. 81:** Curves of  $\Delta\chi^2$  obtained from the global fit to electroweak precision data. The right plot includes in addition the results from the direct Higgs boson searches at LEP and Tevatron. The plots are taken from Ref. [6].

From Fig. 81 it becomes clear that very different experimental search strategies need to be pursued depending on the Higgs mass hypothesis. The golden discovery modes are  $H \rightarrow \gamma\gamma$  for masses below  $\sim 150$  GeV (grand maximum), which is a very rare channel (branching fraction of about 0.2%) with a clean signature,  $H \rightarrow WW^{(*)} \rightarrow \ell\nu\ell\nu$  for high masses, which is an abundant but not a clean mode, and  $H \rightarrow ZZ^{(*)} \rightarrow 2\ell 2\ell'$  which has a sizable branching fraction above  $m_H \simeq 130$  GeV, and which is clean at relatively low mass. We have no space here to discuss all these measurements. Early searches will concentrate on the high-cross-section modes leading to a successive exclusion (or discovery) of smaller and smaller Higgs masses. ATLAS and CMS have performed studies to evaluate the discovery reach of the various Higgs search analyses as a function of the Higgs mass. Figure 82 shows an ATLAS study for the Higgs boson discovery (left panel) and exclusion potential (right panel) for given integrated luminosity versus the Higgs mass. At  $1\text{ fb}^{-1}$  a Higgs of mass between 150 GeV and 170 GeV could be observed with five standard deviations significance, and Higgs masses above  $\sim 127$  GeV can be excluded to at least 95% confidence level.

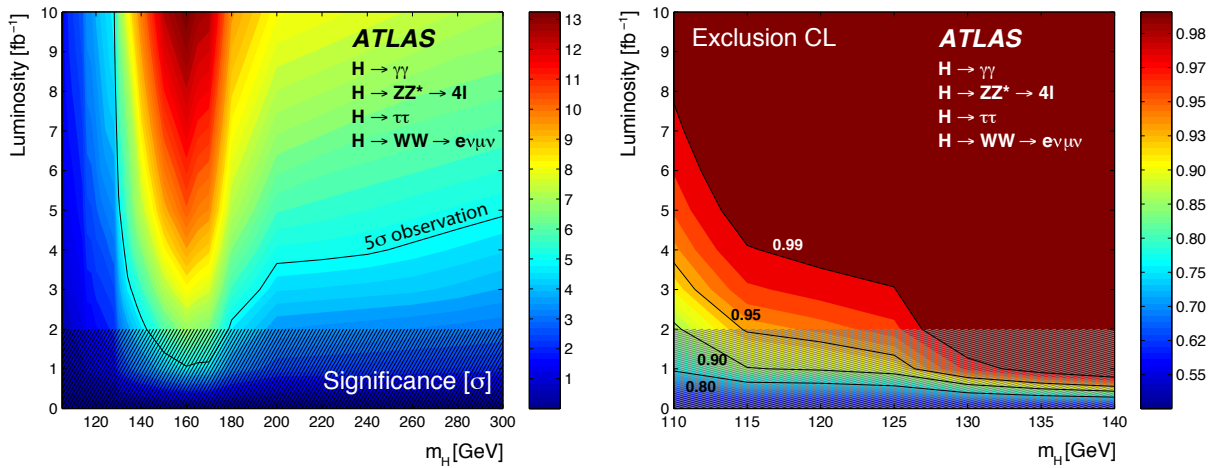


**Fig. 82:** Standard Model Higgs boson discovery (left) and exclusion potential (right) for given integrated luminosity versus the Higgs mass (ATLAS study). The shaded bands at low integrated luminosity indicate that the results are less accurate (but are expected to be pessimistic).



### 10.7 Search for phenomena beyond the Standard Model

The primary motivation for the LHC construction is — beyond the discovery of the Higgs boson — the search for signatures from unknown physics at the high-energy frontier, which it is hoped will provide answers to at least part of the current unknowns and problems outlined in Section 1. There is a wealth of models introducing new physics, which is also driven by the relatively few constraints that the high-energy sector must comply with. At any order of magnitude beyond the TeV scale may lurk new symmetries, the breaking of which creates partners of the known Standard Model fields, but which also may lead to a profusion of new particles at ever higher mass scales. Alternatively, in case we live in an apparently severely fine-tuned world, no new physics exists at least in the quark sector up to the reduced Planck scale, leaving a desert of 16 orders of magnitude all described by the Standard Model interactions. This latter picture must probably be regarded as disfavoured, not only by the fine-tuning argument, but since it also contradicts our experience: up to now, each ascent of an order of magnitude in energy has afforded new phenomena in particle physics.

#### Di-lepton resonances at high mass

Popular early searches for new physics involve di-lepton invariant mass spectra, which may exhibit peaks originating from generic  $Z'$  resonances present in many beyond the Standard Model scenarios, such as grand unified theories, little Higgs models, Technicolour, and models featuring extra spatial dimensions. The widths of the new resonances may be narrow (such as for Randall–Sundrum gravitons), or broad enough so that they may be resolved in the detector (for example heavy resonances in grand unified theories and little Higgs models, as well as in models with small extra dimensions where the gauge fields are allowed to propagate into the extra-dimensional bulk). The most rigorous direct limits on the existence of heavy neutral particles decaying into di-leptons come from direct searches at the Tevatron, excluding mass scales until approximately 1 TeV (model dependent).

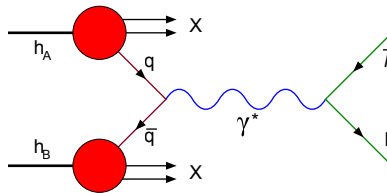


**Fig. 84:** Feynman graph of a Drell–Yan process (quark–antiquark annihilation to a virtual photon or  $Z$  boson) producing a final-state lepton pair.

Contrary to searches with missing transverse energy, which usually do not exhibit clear-cut kinematic signatures, the observation of a di-electron mass peak over (mostly) irreducible Drell–Yan background (Fig. 84) does not require the design calorimeter performance (this is somewhat different for heavy di-muon resonances, where the alignment of the muon system must be well understood to reach good resolution and charge measurement). In case of the search for very high-mass resonances (not

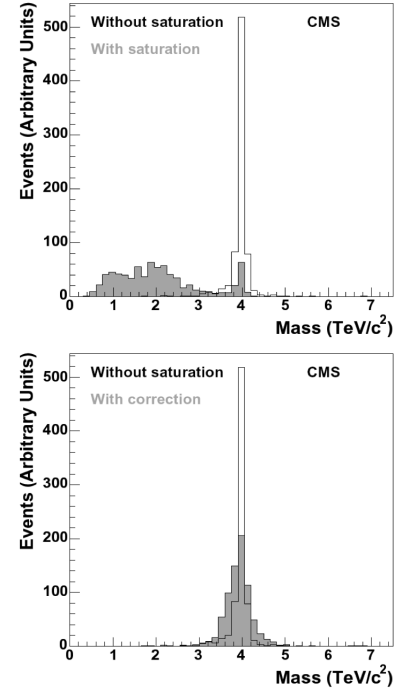


**Fig. 83:** High energy saturation effect (upper plot) and its correction (lower) in the CMS electromagnetic calorimeter for 4 TeV Randall–Sundrum gravitons decaying to  $e^+e^-$ .

early physics), electromagnetic calorimeter saturation must be corrected (Fig. 83 for CMS). It is also not required to predict the background shapes with Monte Carlo simulation. It can be determined from data by means of a parametrised maximum-likelihood fit with parameters determined simultaneously with the signal abundance by the fit.

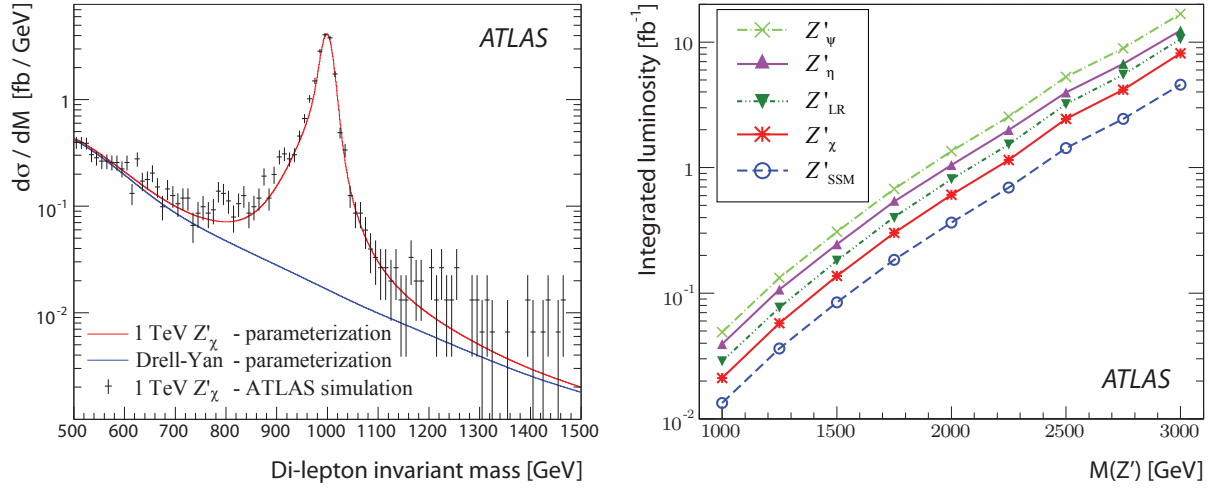


**Fig. 85:** Left: distribution of the di-electron mass for fully simulated ATLAS data (dots) in presence of a 1 TeV  $Z'_\chi$  (solid line) and Drell–Yan background (dashed line). The statistics used correspond to  $21 \text{ fb}^{-1}$ . Right: Required luminosity versus the  $Z'$  mass for a  $5\sigma$  observation according to various  $Z'$  models (ATLAS study).

The left panel in Fig. 85 shows a  $Z'_\chi \rightarrow ee$  peak in ATLAS for a simulated  $Z'$  with mass 1 TeV, over Drell–Yan background. The right panel gives the luminosity that is required for a  $5\sigma$  observation according to various  $Z'$  models, as a function of the  $Z'$  mass. With  $100 \text{ pb}^{-1}$  of data, and 14 TeV centre-of-mass energy,  $Z'$  (and also  $W'$ ) resonances until a mass of roughly 1 TeV could be discovered. The ultimate goal for ATLAS and CMS reaches about 7 TeV (SLHC prospective).

### Statistical considerations

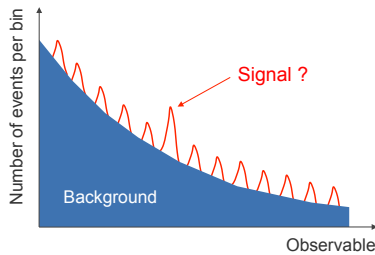


**Fig. 86:** The p-value quantifying the statistical significance of an observation must be corrected for the statistical trials factor.

mass peak with a single p-value<sup>37</sup> of  $3.0\sigma$  ( $5.0\sigma$ ) somewhere in the allowed mass range, and assuming 13 independent trials fit into the mass range, the p-value must be corrected by the corresponding *trials factor*. In this case, we find a corrected p-value of  $2.1\sigma$  ( $4.5\sigma$ ). Because of the non-linearity in the rela-

The search for di-lepton resonances in a mass range that is large compared with the experimental resolution, and without using prior knowledge about which mass the resonance should have, introduces a statistical ‘look-elsewhere effect’. The probability of finding a 6 when playing a dice is  $1/6$ . The probability of finding at least one 6 when playing 2 dice is  $2/6 \cdot (1 - 5/6)$ . In case of a small single-occurrence probability  $p$  and at least one occurrence required, the binomial probability for an occurrence with  $n$  trials can be approximated by  $n \cdot p$ . What counts in the case of the di-lepton invariant mass is the size of the search range in terms of the mass resolution (assuming a negligible intrinsic width of the resonance that is searched for). The number of trials is thus roughly the number of times the resonance ‘fits’ in the given mass range. Assuming the ‘discovery’ of a

<sup>37</sup>Terminology: the *significance level* of a statistical hypothesis test is the fixed probability of wrongly rejecting the null hypothesis, if it is true. It is the probability for a *Type-I error* to occur. The *p-value* is compared with the significance level and, if it is smaller, the result is significant. It is hence the significance of a single trial.

tion between probability and number of standard deviations, the effect of the correction appears larger at smaller significance of the observation.

The above exercise is a very rough approximation. In practice the evaluation of the trials factor is complex, and the conceptually simplest way to take it into account is via toy Monte Carlo simulation. A natural way to proceed is to perform an unbinned maximum-likelihood fit by describing the background by a simple parametrised function, with parameters determined by the fit, and the signal by a Gaussian or crystal-ball shaped function with predetermined width (obtained from Monte Carlo simulation, but taking into account the mass dependence of the calorimeter or tracking resolution) of which only the mean mass parameter is free to vary in the fit. Also determined by the fit are the signal and background abundances. The fit will converge towards ‘some’ signal yield at ‘some’ mass value. To obtain a relative likelihood estimator, the fit is repeated by fixing the signal yield to zero, and the difference between the log-likelihood estimators of the two fits is computed (the fit with free signal yield and mean mass always has a larger log-likelihood value, so that the difference is positive). The p-value of the observed log-likelihood difference is obtained by repeating the same exercise many times with a background-only Monte Carlo model faithfully describing the data. This Monte Carlo model is obtained by using the results from the background parametrisation obtained by the fit to data. The p-value is given by the ratio of the number of cases in which the log-likelihood difference in the Monte Carlo is found to be larger than the one in the data, divided by the total number of trials.

### Supersymmetry

In spite of the many creative and interesting new physics models that have appeared in recent years, supersymmetry remains the most popular Standard Model extension. It features an elegant solution of the hierarchy problem by cancelling the diverging weak boson radiative corrections to all orders (where, however, a logarithmic divergence remains due to supersymmetry breaking), a dark matter candidate, natural elementary scalar particles, the democratisation of the fermionic and bosonic degrees of freedom, and grand unification of the electroweak and strong forces. The minimal supersymmetric Standard Model introduces a conserved supersymmetry-parity, denoted *R-parity*, which is even for all Standard Model particles (including a Higgs doublet), and odd for all supersymmetric partners of these.<sup>38</sup> A consequence of *R-parity* conservation is that the lightest supersymmetric particle (LSP) is stable. Since we have not observed any strongly or electromagnetically interacting particles in the universe that are not included in the Standard Model, and because we need a cold dark matter candidate, it is assumed that the LSP is weakly interacting only (as are neutrinos). The primary LSP candidate is the lightest neutralino, a linear combination of gauginos. In much of the supersymmetry parameter space the neutralino is a mixture of photino and zino, but could also be a gravitino. *R-parity* conservation also implies that supersymmetric particles can only be produced in pairs. Hence, to produce supersymmetry in a hadronic interaction the centre-of-mass energy of the colliding partons must be twice the characteristic supersymmetric mass scale.

A typical decay cascade of a supersymmetric squark or gluino is depicted in the right-hand plot of Fig. 77. From the diagram one notices that supersymmetric events produce many high- $p_T$  jets, sometimes leptons, and always missing transverse energy due to the escaping LSP (unless it escapes along the beam pipe). Since squarks and gluinos are produced by strong interactions with  $\mathcal{O}(\text{picobarn})$  cross sections if their masses are well below a TeV, and because supersymmetric events have a clear experimental signature, supersymmetry could be detected quite early. An integrated luminosity of  $100 \text{ pb}^{-1}$  is expected to be sufficient for a discovery of relatively low-mass supersymmetry, provided that the Standard Model backgrounds can be well controlled.

Figure 87 shows distributions of missing transverse energy in ATLAS for simulated supersymmetry signal and Standard Model background events, and for analyses with (right panel) and without (left

<sup>38</sup>*R-parity*, defined by  $R = (-1)^{2S+3B+L}$ , was originally introduced to avoid the proton decay  $p \rightarrow e^+ \pi^0$ , which is possible in supersymmetry.

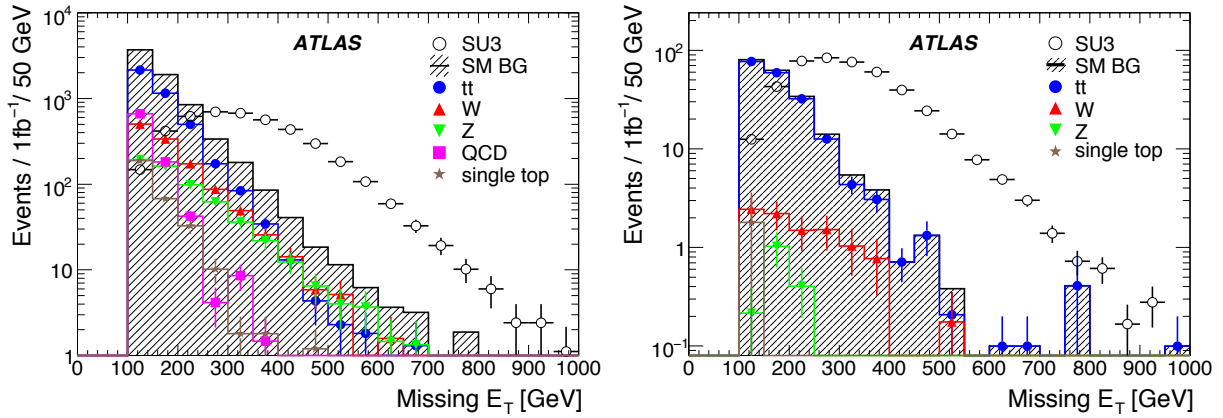


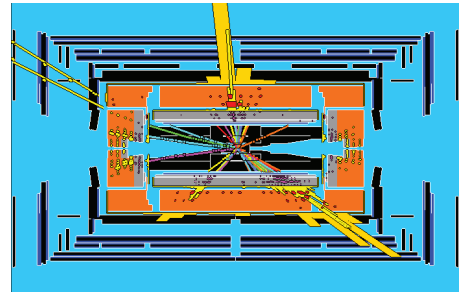
**Fig. 87:** Simulated distributions of missing transverse energy in ATLAS for analyses without (left) and with (right) requiring a reconstructed lepton (electron or muon) in the detector. Shown are the contributions from Standard Model processes and for  $R$ -parity-conserving supersymmetry using a minimal supergravity model (open circles) with the parameters  $m_0 = 100$  GeV and  $m_{1/2} = 300$  GeV. The number of events corresponds to  $10\text{fb}^{-1}$  integrated luminosity.

panel) requiring a reconstructed electron or muon. A clear signal excess is perceptible in both analyses, but the main Standard Model backgrounds differ significantly between the two. Whereas without lepton requirement,  $t\bar{t}$ , and  $W$  and  $Z$  plus jets backgrounds are of similar size in the large- $\cancel{E}_T$  tails, and background from jets (QCD) is also present, the background in the one-lepton analysis is entirely dominated by  $t\bar{t}$ , with some small contributions from  $W$  and jets, but no QCD jets background. This makes the one-lepton analysis particularly interesting for the initial running period, when the understanding of the inclusive QCD background is still immature.

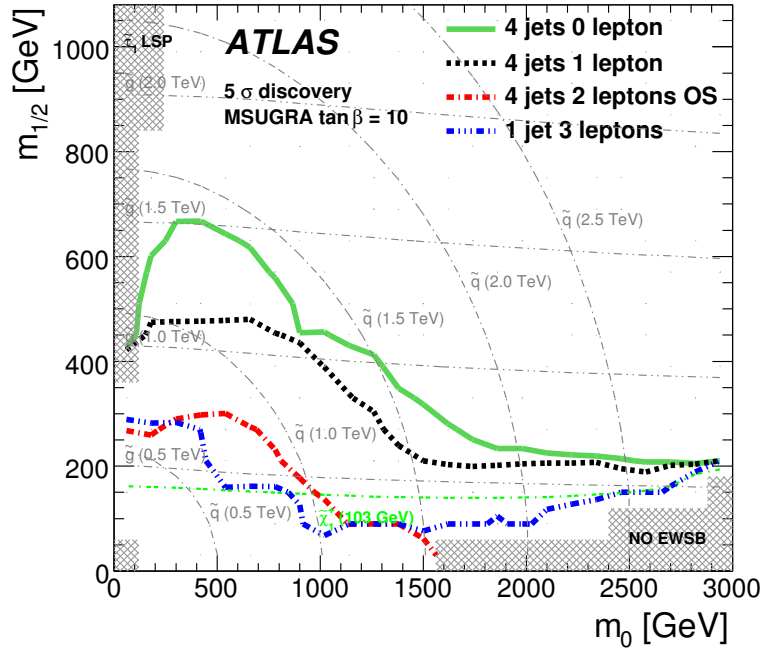
Other discriminating variables used in supersymmetry searches are the ‘effective mass’, which is the scalar sum of the transverse momenta of all jets and leptons (other variations of this variable also include  $\cancel{E}_T$ , or do not include the lepton momentum), and the transverse mass [see Eq. (12)] which is particularly useful to reduce background from events with a  $W$ . Figure 88 shows an event display of a typical supersymmetric event with jets, muons and large  $\cancel{E}_T$  in ATLAS.

Figure 89 shows the expected discovery potential for the minimal supergravity model as a function of the GUT mass parameters  $m_0$  and  $m_{1/2}$  (ATLAS study). The zero-lepton analysis has the best discovery reach. However, taking into account the experimental difficulties of this mode, the one-lepton mode may become competitive. Squarks and gluinos with masses up to 0.75, 1.35, 1.8 TeV can be discovered with integrated luminosities of 0.1, 1 and  $1\text{fb}^{-1}$ , respectively, using the four-jet, zero-lepton analysis.

We should note that supersymmetry could also break  $R$ -parity. The signature could be taus originating from  $\chi_1^0 \rightarrow \tilde{\tau}\tau$  decays. Moreover, signals due to other phenomena could be seen like supersymmetry so that a (challenging) neutralino spin analysis needs to be performed to reveal their fermionic nature. Experimentalists should proceed with the search for supersymmetry as model-independently as possible, and watch out for anomalies, e.g., the occurrence of photons, taus, or strange tops



**Fig. 88:** Simulated supersymmetric event in ATLAS with six particle jets and two muons with opposite charge in the final state, and with large missing transverse energy.



**Fig. 89:** Expected contours for  $5\sigma$  minimal supergravity discovery versus the GUT mass parameters  $m_{1/2}$  and  $m_0$ , for analyses with various lepton requirements and for an integrated luminosity of  $1\text{ fb}^{-1}$ . The grey dashed contour lines indicate the corresponding squark and gluino masses. The zero-lepton analysis has the best discovery reach.

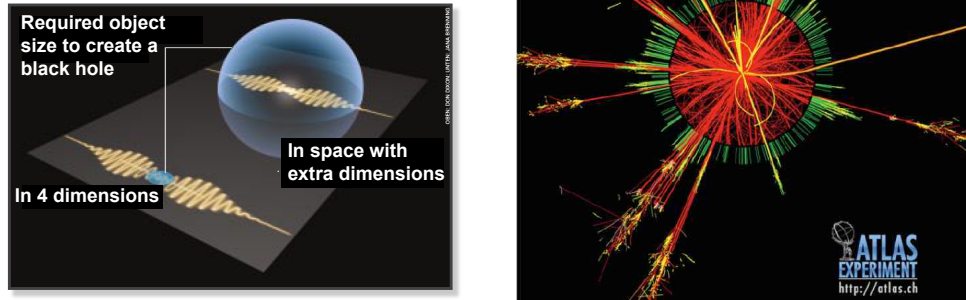


**Fig. 90:** Left: Schwarzschild radius in 4 and  $4+d$  dimensions. Right: Simulation of a black hole decay in ATLAS.

### Strong gravity

Finally, if we are allowed to enter trans-Planck scales, that is, gravity in compact extra spatial dimensions is strong enough to reduce the Planck scale to energies reached by the LHC, hard-scattering proton–proton collisions may produce microscopic black holes. An object becomes a black hole if it is smaller than the Schwarzschild radius  $r = 2GM/c^2$ . In  $4+d$  spatial dimensions the Schwarzschild radius<sup>39</sup> becomes  $r = 2G^{(4+d)}M_D/c^2$ , where  $G^{(4+d)}$  is a gravitational constant in the full-dimensional space. The four-dimensional constant  $G$  is thus only a reflection of the real gravitational constant  $G^{(4+d)}$ , reduced

<sup>39</sup>The Schwarzschild radius is the radius below which the gravitational attraction between the particles of a body is so strong that the body undergoes gravitational collapse. For a typical star such as the Sun, the Schwarzschild radius is about 3 km.



(‘diluted’) by the extra dimensions (see Fig. 90, Left). The Planck scale is no longer fundamental. If  $M_D \approx M_{\text{Planck}}^{(4+d)} \approx 1 \text{ TeV}$ , a black hole can be produced by the LHC if the momentum transfer of the hard scattering reaction exceeds  $M_D$ . The cross section of the black hole production is  $\sigma_{\text{BH}} \approx \pi r^2$ . With  $M_D \sim 2\text{--}3 \text{ TeV}$  one finds  $\sigma_{\text{BH}} \sim \mathcal{O}(\text{pb})$  allowing a fast discovery for  $M_{\text{BH}} < 4 \text{ TeV}$ , and  $d = 2\text{--}6$ .

The black hole undergoes a fast ( $\tau_{\text{BH}} \sim 10^{-27} \text{ s}$ ) thermal decay via Hawking radiation of temperature  $T_H \sim M_D \cdot (M_D/M_{\text{BH}})^{1/(d+1)}$  (a microscopic black hole is not black at all!). The life cycle of a 10 TeV black hole could be sketched as follows: (i)  $\Delta t = 0$ ,  $M_{\text{BH}}(\Delta t) = 10 \text{ TeV}$ : *creation* — the micro black hole is created in a proton–proton collision: it is asymmetric, may vibrate and rotate, and may be electrically charged; (ii)  $\Delta t = 0\text{--}1 \cdot 10^{-27} \text{ s}$ ,  $M_{\text{BH}}(\Delta t) 10\text{--}8 \text{ TeV}$ : *‘baldness phase’* — emission of gravitational and electromagnetic waves, and charged particles, the black hole is solely characterised by mass and angular momentum; (iii)  $\Delta t = 1\text{--}3 \cdot 10^{-27} \text{ s}$ ,  $M_{\text{BH}}(\Delta t) = 8\text{--}6 \text{ TeV}$ : *slowing down* — the black hole radiates by reducing its angular momentum, its form becomes spherical; (iv)  $\Delta t = 3\text{--}20 \cdot 10^{-27} \text{ s}$ ,  $M_{\text{BH}}(\Delta t) = 6\text{--}2 \text{ TeV}$ : *Schwarzschild phase* — after losing its angular momentum, the micro black hole evaporates its mass via Hawking radiation; (v)  $\Delta t = 20\text{--}22 \cdot 10^{-27} \text{ s}$ ,  $M_{\text{BH}}(\Delta t) = 2\text{--}0 \text{ TeV}$ : *Planck phase* — the black hole shrinks down to the Planck mass ( $M_D$ ) and fully decays into all particles with probabilities according to their degrees of freedom (Fig. 90, Right). The spectacular decay signature cannot be missed by the experiments.

## 11 Conclusions and outlook

Commissioning such tremendously complex apparatus as the LHC high- $p_T$  experiments ATLAS and CMS is a continuous challenge. It starts far earlier than with the installation of the experiments in their underground caverns. To some extent it already begins with the design phase, when prototypes are drawn, simulated, and eventually built for the purpose of testing and optimisation. Commissioning continues in dedicated test beams where parts or even complete slices of the detectors, modelling as accurately as possible the final geometry, are assembled. While installing the detectors at their final locations, commissioning campaigns with cosmic ray events are undertaken. Hundreds of millions of cosmic rays have been recorded by both experiments in roughly three years of data taking with more and more complete detectors. Finally, with the start of the LHC commissioning, single beams with 900 GeV injection energy are sent through both LHC beam pipes, circulating or as beam-on-collimator ‘splash’ dumps, radio-frequency captured or not. Later two beams are injected, again at injection energy, radio-frequency captured, and brought to collision. These collisions produce for the first time so-called minimum bias events, producing roughly 20 tracks in the inner tracking systems, some photons from  $\pi^0$  and  $\eta$  decays, and electrons from photon conversion, as well as rare jet events and muons from pion and kaon decays. The beams will not be squeezed at this initial stage so that owing to the large beam spot, the small number of bunches in the machine, and the low bunch intensity, the peak luminosity will not exceed  $10^{27} \text{ cm}^{-2} \text{ s}^{-1}$ . However, once the LHC energy is ramped up, the relativistic contraction of the beam will lead to an increase in the luminosity, and the experiments will see an increase in jet rates, as well as electrons and muons mainly from heavy quark decays and quarkonia. Moreover, beam squeezing (i.e., the reduction of the beam envelope by the magnet optics) and a crossing angle between the colliding beams will further allow an increase in the luminosity of the LHC at higher energy.

With the data taken during these commissioning phases, the experiments have gained experience and obtained a good initial understanding of the detector response, and improved the quality of the data by calibrating and aligning the detector subsystems, which will pay off when analysing the first collision data for physics and detector performance. With the arrival of physics data it is very important to continue improving the detector understanding, and the faithfulness of its description by the detector



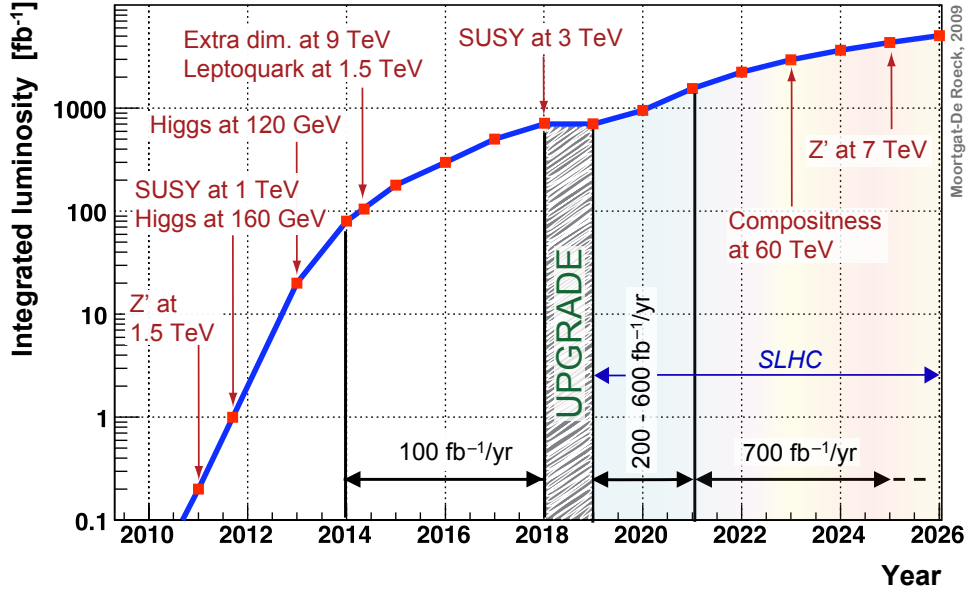


Fig. 91: The LHC programme in a nutshell [28] (see text for discussion).

response simulation. It is the key to a longterm success of the experiments, and to physics results with the smallest possible bias and systematic errors. It is also important that the experiments optimise the fraction of useful data taken, by steadily improving the data-taking efficiency of all detector systems, and aiming at the best achievable data quality.

Figure 91 gives an exploratory view of the expected LHC performance versus year of (design) operation at 14 TeV centre-of-mass energy [28], and the corresponding sensitivity for discovery of various phenomena by the ATLAS and CMS experiments. After accumulating  $1 \text{ fb}^{-1}$  integrated luminosity, minimal supersymmetry with up to 1 TeV characteristic mass scale could be discovered. The Standard Model Higgs boson is expected to be observed at any mass with  $30 \text{ fb}^{-1}$ . With the ultimate integrated luminosity of possibly  $500 \text{ fb}^{-1}$  around the year 2018, the discovery reach for many new physics models can be pushed deep into the TeV scale, and properties of earlier discoveries may be studied. Among these are the coupling strengths of the Higgs boson in various production and decay channels. If the Higgs is observed to decay into either  $\gamma\gamma$  or  $ZZ^{(*)}$ , one will know that it cannot have spin 1. Observations of angular distributions and correlations in  $ZZ^{(*)}$  decays will enable the spin and  $CP$  properties of the Higgs to be determined. It should also be possible to constrain masses of supersymmetric particles, possibly even the spin of a heavy neutralino. A spin analysis of heavy resonances decaying to di-leptons could be performed in case of a discovery. After four years at the highest peak luminosity with approximately  $100 \text{ fb}^{-1}$  of data recorded each year, the increase in sensitivity becomes asymptotic (recall the  $1/\sqrt{\mathcal{L}}$  scaling of statistical errors), which is the opportunity to undertake an upgrade of machine and detectors to the Super-LHC (SLHC). The SLHC programme proposes to increase the LHC peak luminosity to  $1.5 \cdot 10^{35} \text{ cm}^{-2} \text{ s}^{-1}$ , i.e., 10 times the nominal LHC peak luminosity [29]. At nominal bunch pattern, it will compel the experiments to cope with 250 pile-up minimum bias interactions occurring in time with the hard-scattering event. This requires many changes to the detectors: (i) reduce background rates by changing the beam pipe and improving the shielding, (ii) improve the radiation and occupancy tolerance of the detectors and electronics, in many cases by replacing entire subsystems, and (iii) increase the bandwidth of front-end and readout electronics to minimise pile-up and handle a 10 times increase in the event rate. A successful SLHC upgrade would allow the experiments to extend their discovery reach for supersymmetry and  $Z'$  bosons to 4 TeV and 7 TeV, respectively.

The current situation, however, is that, owing to limitations in the quench protection system, the LHC will begin in 2010 with 7 TeV centre-of-mass energy, which later in the year may or may not be

increased to a maximum of 10 TeV. ATLAS and CMS have performed indicative studies to evaluate the impact of the reduced energy on their physics programme. It is expected that up to half an inverse femtobarn of data will be delivered in 2010. (If the run is continued through 2011 a total of one inverse femtobarn of data could be delivered.) Between 14 TeV and 10 TeV the number of selected  $Z \rightarrow ee$  events will decrease from roughly 5000 per  $10\text{pb}^{-1}$  integrated luminosity to 3600 (linear relationship). The number of produced  $t\bar{t}$  events will drop by roughly a factor of 2, so that the sample size will attain that of the Tevatron after approximately  $100\text{pb}^{-1}$  at 10 TeV. The exclusion of a Higgs boson requires about twice more integrated luminosity at 10 TeV than at 14 TeV. A  $5\sigma$  discovery of a Higgs with mass of 160 GeV (which is unlikely) would require roughly  $1\text{fb}^{-1}$  of recorded physics data. To challenge the Tevatron Higgs searches, a sample of about  $200\text{pb}^{-1}$  at 10 TeV is needed. The sensitivity of the search for a heavy  $Z'$  is reduced by a factor of roughly 3 at 10 TeV. A  $5\sigma$  observation of a 1 TeV (Tevatron limit) weighing  $Z'$  would require roughly  $100\text{pb}^{-1}$  of 10 TeV collision data. To achieve an equivalent discovery reach for supersymmetry, a factor of 2 more integrated luminosity is required at 10 TeV centre-of-mass energy. Nevertheless, the current Tevatron limits can be improved with as little as  $20\text{pb}^{-1}$  of 10 TeV data. What would be the impact of a 7 TeV centre-of-mass energy compared to 10 TeV? The number of  $Z \rightarrow ee$  will drop by another factor of 1.4. The  $t\bar{t}$  rate will further drop by approximately a factor of 2. The required luminosity for equal search sensitivity for a  $Z'$  will increase by a factor of 3, similarly for supersymmetry searches, and a factor of 2–3 for Higgs searches.

## References

- [1] ATLAS Collaboration, JINST **3**, S08003 (2008).
- [2] CMS Collaboration, JINST **3**, S08004 (2008).
- [3] ATLAS Collaboration, *Expected Performance of the ATLAS Experiment: Detector, Trigger and Physics*, CERN-OPEN-2008-020, arXiv:0901.0512 (2008).
- [4] CMS Collaboration, *CMS Physics: Technical Design Report*, Volume I: CMS-TDR-008-1, CERN-LHCC-2006-001; Volume II: CMS-TDR-008-2, CERN-LHCC-2006-021 (2006).
- [5] CDF Collaboration (T. Aaltonen *et al.*), Phys. Rev. Lett. **102**, 031801 (2009); D0 Collaboration, Conference Note 5923-CONF (2009).
- [6] H. Flücher *et al.*, Eur. Phys. J. C **60**, 543 (2009) [arXiv:0811.0009], <http://cern.ch/gfitter>.
- [7] ALEPH Collaboration (S. Schael *et al.*), Phys. Rep. **421**, 191 (2005) [arXiv:hep-ex/0506072].
- [8] M. Davier, S. Descotes-Genon, A. Höcker, B. Malaescu and Z. Zhang, Eur. Phys. J. C **56**, 305 (2008) [arXiv:0803.0979].
- [9] CKMfitter Group (J. Charles *et al.*), Eur. Phys. J. C **41**, 1 (2005) [arXiv:hep-ph/0406184], <http://ckmfitter.in2p3.fr>.
- [10] A. Hoecker and W. Marciano, The muon anomalous magnetic moment (in: Review of Particle Physics 2008), Phys. Lett. B **667**, 1 (2008), updated 2009 on <http://pdglive.lbl.gov>.
- [11] J. Ellis, *Beyond the Standard Model for Montañeros*, lectures at this School.
- [12] A.D. Martin, R.G. Roberts, W.J. Stirling, and R.S. Thorne, Eur. Phys. J. C **14**, 133 (2000) [arXiv:hep-ph/9907231].
- [13] The Tevatron Electroweak Working Group, FERMILAB-TM-2439-E, arXiv:0908.1374 (Aug 2009).
- [14] J. Nash, *Instrumentation for the LHC experiments*, lectures at this School.
- [15] D. Froidevaux and P. Sphicas, Annu. Rev. Nucl. Part. Sci. **56**, 375 (2006).
- [16] N. Ellis, *Trigger and data acquisition*, lectures at this School.
- [17] T. Gaisser, *Cosmic Rays and Particle Physics* (Cambridge University Press, 1990).
- [18] S. Aefsky *et al.*, J. Instrum. **3**, P11005 (2008).
- [19] T. Hebbeker and C. Timmermans, Astropart. Phys. **18**, 107 (2002) [arXiv:hep-ph/0102042].

- [20] MINOS Collaboration (P. Adamson *et al.*), Phys. Rev. D **76**, 052003 (2007) [arXiv:0705.3815].
- [21] CMS Collaboration [M. Aldaya, P. Garcia-Abia], CMS NOTE-2008/016 (2008).
- [22] ATLAS Collaboration, arXiv:0912.2642 (2009).
- [23] T. Sjöstrand, *QCD at LHC in pp*, Talk given at 3rd Nordic *LHC and Beyond* Workshop, Lund, Sweden, 2009.
- [24] S. Van der Meer, CERN internal report, ISR-PO/68-31, 1968.
- [25] K.A. Brown, M. Blaskiewicz, C. Degen, and A. Della Penna, Phys. Rev. Spec. Topics — Accelerators and beams **12**, 012801 (2009).
- [26] CDF Collaboration, Phys. Rev. D **79**, 112005 (2009) [arXiv:0904.1098].
- [27] CDF Collaboration, Phys. Rev. Lett. **103**, 092002 (2009) [arXiv:0903.0885]; D0 Collaboration, Phys. Rev. Lett. **103**, 092001 (2009) [arXiv:0903.0850].
- [28] A. de Roeck and F. Moortgat, *Private communication* (2010).
- [29] SLHC web site with references to project papers: <http://project-slhc.web.cern.ch/project-slhc>.